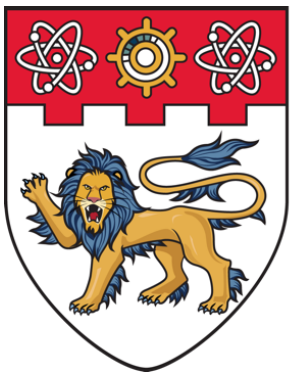

NANYANG TECHNOLOGICAL UNIVERSITY
SINGAPORE

SYNTHESIS OF Nd-Fe-B BASED MAGNETIC MATERIALS THROUGH THE MECHANOCHEMICAL PROCESS

ZHONG YAOYING

SCHOOL OF MATERIALS SCIENCE AND ENGINEERING

2018

SYNTHESIS OF Nd-Fe-B BASED MAGNETIC MATERIALS THROUGH THE MECHANOCHEMICAL PROCESS

ZHONG YAOYING

SCHOOL OF MATERIALS SCIENCE AND ENGINEERING

A thesis submitted to the Nanyang Technological University
in partial fulfilment of the requirement for the degree of
Doctor of Philosophy

2018

Statement of Originality

I hereby certify that the work embodied in this thesis is the result of original research and has not been submitted for a higher degree to any other University or Institution.

Input Date Here

30/12/18

Date

Dec 30, 2018

Input Signature Here

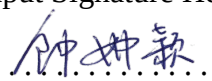

Input Name Here

Zhong Yaoying

Supervisor Declaration Statement

I have reviewed the content and presentation style of this thesis and declare it is free of plagiarism and of sufficient grammatical clarity to be examined. To the best of my knowledge, the research and writing are those of the candidate except as acknowledged in the Author Attribution Statement. I confirm that the investigations were conducted in accord with the ethics policies and integrity standards of Nanyang Technological University and that the research data are presented honestly and without prejudice.

Input Date Here

30/12/18

Date

Dec 30, 2018

Input Supervisor Signature Here

Raju V. Ramanujan

Input Supervisor Name Here

Raju V. Ramanujan

Authorship Attribution Statement

This thesis contains material from papers published/submitted in the following peer-reviewed journals where I was the first author.

Chapter 4 is published as Y. Zhong, V. Chaudhary, X. Tan, H. Parmar and R. V. Ramanujan, Mechanochemical synthesis of high coercivity $Nd_2(Fe, Co)_{14}B$ magnetic particles. *Nanoscale* **9**, 18651-18660 (2017). DOI: 10.1039/C7NR04703G.

The co-authors' contributions are listed as below:

- A/Prof R. V. Ramanujan furnished with the project direction in the beginning and reviewed and edited the drafted manuscript.
- I co-designed the study with A/Prof R. V. Ramanujan and performed all the laboratory work at the School of Materials Science and Engineering and the School of Physical and Mathematical Sciences. I also analyzed the data.
- I prepared the manuscript drafts. The manuscript was revised by Dr Chaudhary and Dr. Parmar.
- All microscopy, including sample preparation, was conducted by me in the Facility for Analysis, Characterization, Testing and Simulation and in the School of Physical and Mathematical Sciences.
- Ms Tan Xiao discussed the results and data with me.
- Dr Chaudhary assisted in the collection and provided guidance in the interpretation of the magnetic measurement data.

Chapter 5 is published as Y. Zhong, V. Chaudhary, X. Tan, H. Parmar and R. V. Ramanujan, Kinetic study of the mechanochemical synthesis of $Nd_2(Fe, Co)_{14}B$ hard magnetic nanoparticles. *Journal of Alloys and Compounds* **747**, 755-763 (2018). DOI: 10.1016/j.jallcom.2018.03.077.

The co-authors' contributions are listed as below:

- A/Prof R. V. Ramanujan furnished with the project direction in the beginning and reviewed and edited the drafted manuscript.
- I co-designed the study with A/Prof R. V. Ramanujan and performed all the laboratory work at the School of Materials Science. I also analyzed the data and prepared the modeling methodology.
- I prepared the manuscript drafts. The manuscript was revised by Dr Chaudhary and Dr. Parmar.
- All microscopy, including sample preparation, was conducted by me in the Facility for Analysis, Characterization, Testing and Simulation.
- Ms Tan Xiao discussed the results and data with me.

Chapter 6 is submitted as Y. Zhong, V. Chaudhary, X. Tan, H. Parmar and R. V. Ramanujan, High coercivity Dy substituted Nd-Fe-Co-B magnetic nanoparticles produced by mechanochemical processing. Submitted, *Journal of Alloys and Compounds* (2018).

The co-authors' contributions are listed as below:

- A/Prof R. V. Ramanujan furnished with the project direction in the beginning and reviewed and edited the drafted manuscript.
- I co-designed the study with A/Prof R. V. Ramanujan and performed all the laboratory work at the School of Materials Science. I also analyzed the data and prepared the modeling methodology.
- I prepared the manuscript drafts and conducted the manuscript revision with Dr Chaudhary and Dr. Parmar.
- All microscopy, including sample preparation, was conducted by me in the Facility for Analysis, Characterization, Testing and Simulation.
- Ms Tan Xiao discussed the results and data with me.
- Dr Chaudhary assisted in the collection and provided guidance in the interpretation of the magnetic measurement data.

Input Date Here

30/12/18

Date

Dec 30, 2018

Input Signature Here

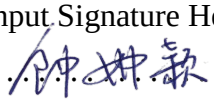

Input Name Here

Zhong Yaoying

Abstract

The limited geographical availability of rare earth elements has resulted in fluctuations in the price of rare earth permanent magnets. The high cost of Nd-Fe-B permanent magnets has limited the range of applications of these magnets. Therefore, a reduction in the use of rare earth elements or a reduction in the processing cost of Nd-Fe-B based magnets is urgently needed. However, most conventional processing methods of rare earth magnets are physical methods which require elemental rare earths as precursors, these elements are much more expensive than rare earth oxides. Developing chemical methods using low cost precursors is necessary to reduce the cost of Nd-Fe-B magnets. The large energy product of nanostructured Nd-Fe-B particles is also of interest. In mechanochemical processing, low cost metal oxides (e.g., Nd_2O_3, Dy_2O_3, Fe_2O_3, CoO and B_2O_3) are reduced by Ca granules during milling, in the presence of a CaO diluent. The desired tetragonal crystal structure of Nd-Fe-B nanoparticles is observed after annealing. It is a low cost and scalable process to produce high coercivity Nd-Fe-B magnetic nanoparticles. However, only a few studies of the mechanochemical synthesis of Nd-Fe-B magnets have been conducted. Detailed studies of the process have not been carried out. Hence in this work, the role of process parameters, reaction mechanisms and reaction kinetics of mechanochemical processing of Nd-Fe-B based magnets were investigated.

The effect of process parameters in the mechanochemical process, e.g., milling time and diluent (CaO) content, were investigated during the synthesis of $Nd_2(Fe,Co)_{14}B$ magnetic nanoparticles. The diluent content influenced the formation of $Nd_2(Fe,Co)_{14}B$, with the reduction process delayed for larger CaO content. For smaller CaO content, reduction of precursor oxides occurred during milling. For larger CaO content, the reduction reaction could only be triggered by subsequent annealing. With increasing CaO content, the crystallite size of the synthesized $Nd_2(Fe,Co)_{14}B$ magnetic nanoparticles increased from 11 nm to 38 nm, accompanied by an enhancement in coercivity. The highest coercivity value of 8.8 kOe was obtained with 50 wt% of diluent. This is the highest coercivity observed for $Nd_2(Fe,Co)_{14}B$ magnetic nanoparticles synthesized by chemical methods.

To investigate the reaction mechanism during mechanochemical milling, a study of the phase transformations as a function of milling time for a range of milling speeds was performed. It was found that continuous input of mechanical energy was required for the reaction to reach equilibrium. Three stages were observed during mechanochemical milling: (1) fast amorphization of precursor metal oxides, (2) continuous reduction of metal oxides, (3) steady state. A model was proposed to predict the milling kinetics, there is good agreement between experimental data and the predictions. The milling efficiencies at different milling speeds were calculated by the model; the highest milling efficiency was observed at a milling speed of 550 rpm.

Dy alloyed $(Nd_{1-x}Dy_x)_2(Fe,Co)_{14}B$ (x = 0 to 0.6) magnetic nanoparticles were also synthesized to further increase coercivity and thermal stability. The effects of Dy on the structure and magnetic properties of $(Nd_{1-x}Dy_x)_2(Fe,Co)_{14}B$ nanoparticles were investigated. Homogeneous Dy distribution was observed and high room temperature coercivity of 17.5 kOe was obtained at x = 0.5. Improved thermal stability was observed with increasing Dy substitution. The reduced spin reorientation temperature of these particles suggests that they are attractive for cryogenic applications. The coercivity mechanism of these particles was determined and it was shown that the nucleation of reversed domains was the controlling mechanism.

These results suggest that mechanochemical synthesis of hard magnets is feasible and cost-effective. Process parameter optimization and modeling can be employed to maximize the properties of Nd-Fe-B based permanent magnets.

Lay Summary

Nd-Fe-B type magnets possess the highest magnetic strength among all magnets; they are essentially needed in every aspect in daily life, ranging from small devices like headphones, to large devices such as electric motors. However, the price of Nd-Fe-B magnets is high and volatile. It is mainly due to the high price and low geographic availability of the rare earth element Nd, as well as the high processing cost of commercially available Nd-Fe-B magnets. Therefore, it is important to develop rare earth lean magnets or to reduce the cost of Nd-Fe-B magnets through novel processing methods. Scientists have also found that nanostructured magnets can exhibit excellent properties. Hence, using a cost-effective method to produce Nd-Fe-B nanoparticles has emerged as an area of great interest. The mechanochemical method, which involves chemical reactions during mechanical milling, stands out as it is green, scalable, and most importantly, can produce hard magnetic nanoparticles with low cost metal oxides as precursors. In this process, low cost metal oxides (e.g. Nd_2O_3, Dy_2O_3, Fe_2O_3, CoO and B_2O_3) are reduced by Ca granules in the presence of a diluent (CaO) during milling, and the desired Nd-Fe-B nanoparticles are formed by a subsequent heat treatment process. Though $Nd_2Fe_{14}B$ nanoparticles were synthesized through this method by previous researchers, detailed examination of the effects of processing parameters was not performed, and the reaction mechanism was unclear. Hence, this work focused on an investigation of the influence of processing parameters and reaction mechanisms on the mechanochemical synthesis of Nd-Fe-B based magnetic nanoparticles.

As CaO was added into this process as a diluent, the influence of CaO content on the mechanochemical process was studied. With increasing diluent content, an increasing magnetic field was needed to demagnetize the fully magnetized synthesized $Nd_2(Fe,Co)_{14}B$ magnetic nanoparticles, in another word, the coercivity of the synthesized particles increased. It was found that an optimum diluent content of 50 wt% yielded the highest coercivity. The milling process can be monitored by measuring the phase transformation process during milling. A three-stage milling process was observed: (1). the large mechanical energy induced by ball milling quickly amorphized all the precursor oxides,

(2). the precursor oxides were reduced by Ca granules, (3). achieving of a steady-state. The same milling process was observed over a range of milling speeds. A model was proposed to monitor the reaction kinetics during milling. Good agreement between the model and experimental data was observed. The highest milling efficiency was observed at 550 rpm. In order to further enhance the magnetic properties and improve the thermal stability of the magnets, Dy substitution of Nd was performed to synthesize $(Dy_xNd_{1-x})_2(Fe,Co)_{14}B$ magnetic nanoparticles. The coercivity of the synthesized nanoparticles increased with increasing Dy content until $x = 0.5$. The thermal stability was also improved with increasing Dy alloy content. All these results prove that the mechanochemical method is a cost-effective method to synthesize hard magnetic nanoparticles. The process parameters were optimized to achieve better magnetic properties.

Acknowledgements

I would first like to take this opportunity to convey my sincere gratitude to my supervisor *Prof. Raju V. Ramanujan* for offering me the opportunity to carry out research under his guidance. I am very grateful for his patience, professional guidance, continuous encouragement and generous support throughout this research project. His excellent guidance and encouragement have always been of immense value. I really gained a lot of knowledge from the discussions I had with him. I would also like to thank my co-supervisor *Prof. Huang Yizhong* for his trust, motivation and selfless help that incent me in many ways. My special thanks to Prof Alex Yan and Prof Rajdeep Singh Rawat for serving on thesis advisory committee for their critique and constructive comments on this research time to time.

I would also like to thank Prof. Christen Kloc and Dr Apoorva Chaturvedi, for their kind advice and help in the heat treatment process of this work.

My sincere thanks also go to past and present members in Prof Raju's group: Prof Zhong Xichun, Harshida, Varun, Chen Xi, Maheswar, Vijay, Anansa, Ayan, Suresh, Tan Xiao, Vinay, Xing Hua, Deepak, Subhasis for providing valuable support in their own expertise and for creating a lively and cooperative environment in the lab.

I would like to thank all technical staffs in MSE department for their patient trainings and providing of a friendly environment.

This work would not have been possible without the support of Rolls Royce @ NTU Corporate Lab and National Research Foundation.

I would like to thank the School of Materials Science and Engineering (MSE) who provided me scholarship and support to attend the scientific meetings locally and abroad. I thank the IEEE magnetic society for providing me the summer school scholarship in the Universidad International Menendez Pelayo, Spain, where I benefited greatly.

The list of acknowledgements will not be completed if I do not mention the support of my family members that were always a source of inspiration for me. It was their unconditional love, support and encouragement that supports me on going through 4 years of PhD study.

Table of Contents

Table Captions

Figure Captions

Abbreviations

BEI	Backscatter Electron Images
BSE	Backscattered Electron
EDS	Energy Dispersive X-ray Spectroscopy
XRD	X-ray Diffraction
XPS	X-ray photoelectron spectroscopy
SAED	Selected Area Electron Diffraction
SEM	Scanning Electron Microscopy
PM	Permanent Magnets
TEM	Transmission Electron Microscopy
Z	Atomic Number

Chapter 1

Introduction

One of the greatest challenges being confronted by today's scientists is to develop renewable energy resources and improve energy efficiency in the energy life cycle. Permanent magnets play a vital role in enhancing the performance and efficiency of various energy-related devices, including motors, wind turbines, power generators, etc. Nd-Fe-B based magnets, due to their superior hard magnetic properties, are being used in many of these devices. However, due to strategic issues surrounding the use of rare earth elements, such as Nd, and the high processing cost of Nd magnets, Nd-Fe-B based magnets are limited to high end systems. A novel cost-effective synthesis method is urgently needed to increase the use of Nd-Fe-B based magnets and improve energy efficiency. Hence, a "green" and cost-effective mechanochemical processing method, which uses metal oxides, instead of elemental metals, as precursors, was studied for the synthesis of Nd-Fe-B based magnets. This synthesis process was optimized by determining the influence of various processing parameters and by a study of the processing kinetics. (Dy, Nd)-(Fe-Co)-B alloys were also synthesized by this mechanochemical processing technique in order to further improve the properties.

1.1 Hypothesis/Problem Statement

Politicians, scientists and other interested parties have urged a reduction in the use of traditional hydrocarbon energy sources. Instead, green and renewable energy supplies should be developed. The reasons behind this thrust include global warming, oil price volatility, air pollution due to the use of fossil fuels and the need for diversification in energy portfolios. Electrical machines that utilize renewable energy include electric motors, hybrid cars, wind turbines etc. However, utilization of renewable energy requires efforts from several parties; one major obstacle is the performance of permanent magnets [1]. High performance permanent magnets are mostly rare earth based, e.g., Nd-Fe-B type permanent magnets and Sm-Co type permanent magnets. These magnets produce significantly stronger magnetic field than other hard magnets. They support energy conversion systems by their use in high-efficiency motors and generators. Hence, higher performance permanent magnets are beneficial for energy efficiency and a green earth.

One figure of merit in characterizing permanent magnets is the energy product, i.e. $(BH)_{max}$, which measures the maximum magnetostatic energy that can be stored in free space between the pole pieces of the magnet. Nd-Fe-B type permanent magnets possess the highest $(BH)_{max}$ among all known permanent magnets [2, 3]. They are the most attractive magnets in high-end energy conversion systems. However, the usage of Nd-Fe-B permanent magnets is limited due to their high cost. Reducing the cost of Nd-Fe-B type permanent magnet while maintaining or enhancing its high performance would be of great benefit to the energy conversion industry.

Nanostructured magnets or magnetic nanoparticles are of high interest since Coehoorn et.al developed a novel exchange-coupled nanocomposite magnet with high energy product $(BH)_{max}$ [4]. Later in 1991, the behavior and magnetic properties of these exchanged-coupled nanocomposite magnets was explained by the one-dimensional model proposed by Kneller and Hawig. They have proposed that the soft regions should have dimensions of the domain wall width of the hard phase for optimum coercivity [5]. And later analytical calculations by Skomski and Coey [6] and micromagnetic simulations by Schrefl et al. [7]

agree with the result of Kneller and Hawig on the critical particle dimensions. Figure 1.1a illustrates the energy product enhancement induced by exchange coupling. Figure 1.1b is a schematic of the exchange coupling. If the magnetic soft phase and hard phase can be fully exchange coupled, the composite magnet will possess both high coercivity from the hard phase and high magnetization from the soft phase. However, if the two phases cannot be fully exchange coupled, the hysteresis loop will behave as the decoupled composite loop (Figure 1.1a), with limited performance. Hence, developing nano-sized Nd-Fe-B can be the key to producing high-performance magnets. Coey's prediction of giant energy product for anisotropic $Sm_2Fe_{17}N_3/Fe_{67}Co_{33}$ nanocomposite magnets [6] and the high value of coercivity and $(BH)_{max}$ reported in nano-composite thin films [8] further enhanced interest in nanostructured Nd-Fe-B magnets.

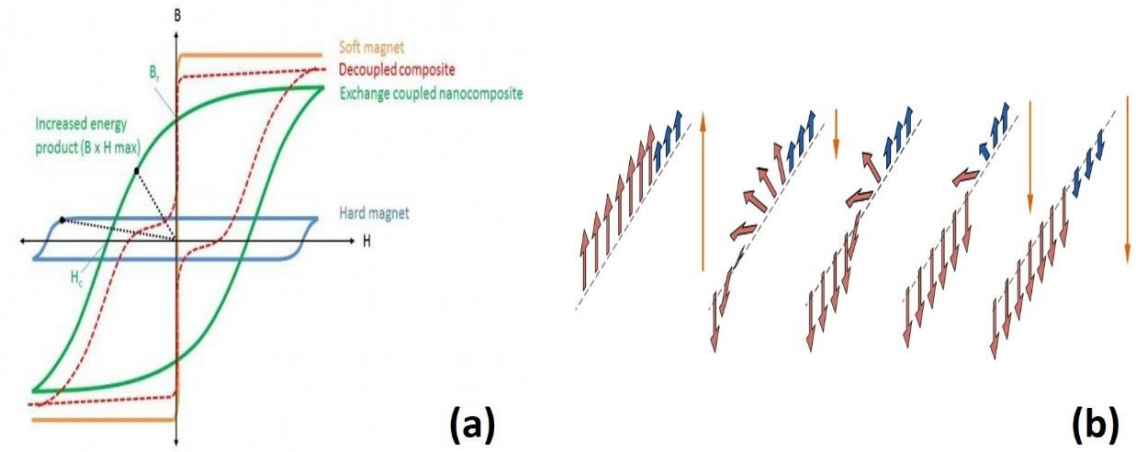

Figure 1.1. (a) Schematic of M-H hysteresis loops of soft magnets, hard magnets, exchange coupled nanocomposite magnets and decoupled composite magnets, respectively. (b). Schematic of exchange coupling for magnetic property enhancement.

The current conventional processing method of Nd-Fe-B type permanent magnet includes melt spinning, powder metallurgical sintering, hydrogenation-disproportionation-desorption-recombination (HDDR) etc. [9-13]. Such sintered Nd-Fe-B magnets represent ~ 90% of the Nd-Fe-B type permanent magnet market [13]. However, all these methods requires elemental powders as precursors, the high cost of elemental neodymium increases the price of Nd-Fe-B magnets produced by these methods. It is difficult to perform controlled synthesis of nanostructured Nd-Fe-B or Nd-Fe-B nanoparticles via physical

methods. On the other hand, uniform Nd-Fe-B based nanoparticles can be achieved by chemical synthesis routes, such as the sol-gel process, auto-combustion process, reduction-diffusion process, solution based synthesis etc. [14-19]. However, these techniques are mostly lab-based, hard to scale up and associated with limited magnetic properties. Hence, there is an urgent need to develop and study a low-cost, scalable processing technique for nanostructured Nd-Fe-B magnets.

The mechanochemical method is a well-established method and has been used in inorganic synthesis of metals and alloys [20-22]. It has also gained more interest in the last decade to achieve selective and "greener" syntheses of organic systems [23]. In the field of magnetic materials, it was first used in the synthesis of Sm-Co particles with relatively good properties. Hard magnetic nanoparticles for anisotropic exchange-coupled nanocomposites applications have also been prepared [24]. In this method, permanent magnetic powders were synthesized through mechanically and thermally activated reduction of metal oxides (e.g. Nd_2O_3, Fe_2O_3, B_2O_3) by calcium. The use of metal oxides instead of elemental metal powders greatly reduces precursor cost, while the large magnitude of mechanical energy associated with ball milling reduces processing time and makes the process scalable. Table 1.1 compares the raw material cost for the synthesis of 1 kg of $Nd_2Fe_{12}Co_2B$ by the conventional physical process and the mechanochemical process. The cost can be reduced by more than 50 % if the mechanochemical process is employed. In addition, the enclosed reaction environment in a ball miller provides well-defined parameters for process optimization. Overall, the mechanochemical method shows potential for cost-effective processing of high performance Nd-Fe-B based nanoparticles.

Table 1.1. Cost comparison for raw materials to produce 1 kg of $Nd_2Fe_{12}Co_2B$, by the conventional process and the mechanochemical process, respectively.

	Mechanical Milling				Mechanochemical Milling				
Precursors	Nd	Fe	Co	B	Nd_2O_3	Fe_2O_3	CoO	B_2O_3	Ca
Cost (SGD/gram)	21	0.33	1	22	3.22	0.11	0.8	1.64	1.62
Amount (g) /1 kg $Nd_2Fe_{12}Co_2B$	266	616	108	10	310	880	138	32	900
Cost (SGD/1 kg $Nd_2Fe_{12}Co_2B$)	6117				2716				

Apart from cost, another driving force for research and development in Nd-Fe-B type permanent magnets is to improve its low Curie temperature (T_C) and limited operating temperature range to satisfy the needs of modern energy conversion devices. The T_C of $Nd_2Fe_{14}B$ is ~ 310 °C and its operating temperature is usually ~ 100 °C which is below the temperatures observed in high power devices. Hence, there is a need to increase the Curie temperature and operating temperature of Nd-Fe-B type magnets.

The strength of ferromagnetic exchange interactions can be used via a mean field theory to estimate the magnitude of the Curie temperature of ferromagnetic alloys. The Bethe-Slater curve provides a description of the relationship between exchange energy and atomic spacing (Figure 1.2). This curve is informative in describing the effect of alloying on the Curie temperature [25, 26]. One can estimate that the Curie temperature of Co (T_C = 1130 °C) should be higher than that of Fe (T_C=770 °C) due to higher exchange interactions, and that Co substitution of Fe in $Nd_2Fe_{14}B$ could increase Curie temperature. Co substitution of Fe in $Nd_2Fe_{14}B$ indeed increase T_C while having minimum deleterious effects on coercivity and magnetization [27, 28].

Although the Curie temperature of $Nd_2Fe_{14}B$ can be improved by Co substitution of Fe, the temperature stability of this magnet will not be enhanced, and the operating temperature of Co alloyed Nd-Fe-B magnets is still limited. Dy substitution of Nd can improve the thermal stability of Nd-Fe-B, and expands the operating temperature of Nd-Fe-B. This strategy is widely used in some challenging automotive applications [28]. Due to the large magnetocrystalline anisotropy field of $Dy_2Fe_{14}B$ (H_A = 15.8 T), Dy substitution of Nd in Nd-Fe-B structure can also enhance its coercivity [29, 30]. Various studies have shown improved temperature stability and magnetic properties in Nd-Fe-B magnetic materials via Co and Dy substitution [31, 32].

Hence, the synthesis of (Nd, Dy)-(Fe, Co)-B permanent magnetic particles by the cost-effective mechanochemical method is promising to produce suitable material for modern electric conversion systems.

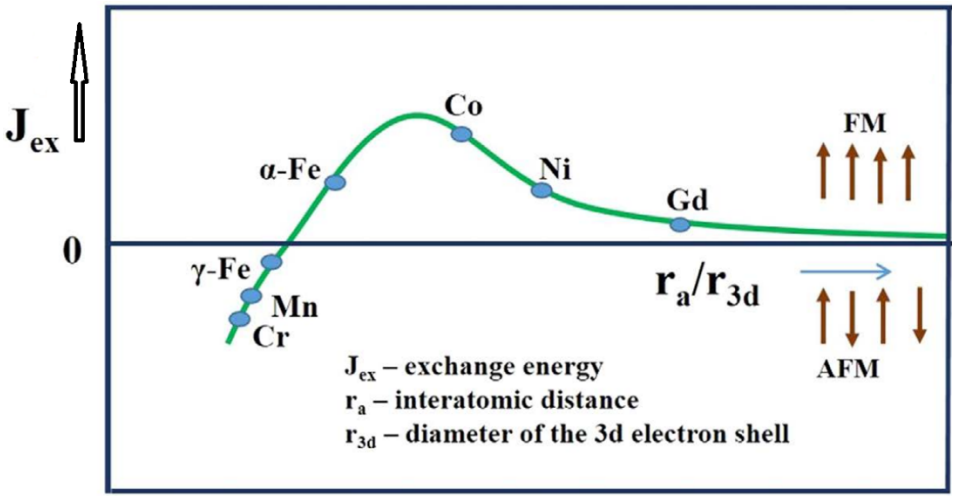

Figure 1.2. Bethe-Slater curve showing the relationship between interatomic spacing (r_a/r_{3d}) and exchange interactions (J_{ex}). r_a represents the interatomic distance for a certain element, r_{3d} is the diameter of the 3d electron shell of that element, J_{ex} is a measure of the exchange interaction.

1.2 Objectives and Scope

Based on the proposed problem statement, the main aim of this project is to study a cost-effective mechanochemical method to synthesize nanostructured Nd-Fe-B based hard magnets with good magnetic performance. Fe is partially replaced by Co to improve the limited Curie temperature. To expand the operating temperature range, Nd is partially replaced by Dy. The following objectives and scope were selected, there are no previous studies of the mechanochemical processing of Nd-(Fe, Co)-B or (Nd, Dy)-(Fe, Co)-B based magnetic materials.

The processing parameters during the mechanochemical milling process were varied to optimize the production of high performance Nd-Fe-Co-B particles. The structural and magnetic properties of these particles were characterized by X-ray diffraction (XRD), transmission electron microscopy (TEM) and the vibrating sample magnetometer (VSM). The formation mechanism of $Nd_2(Fe,Co)_{14}B$ was also studied.The kinetics of the mechanochemical milling process were monitored by measuring the mass percentage of each phase. Based on these experimental data and our theoretical results, a kinetic model was constructed for better understanding of the process.

An advantage of the mechanochemical method compared to other physical methods is the ease of controlling composition by tuning the precursor content. Hence, the effect of alloying of Dy in $Nd_2(Fe,Co)_{14}B$ alloys was studied. The magnetic properties were measured and the optimized alloy concentration was determined. The coercivity reversal mechanism of these Dy-alloyed samples was also analyzed.

1.3 Dissertation Overview

This thesis demostrated the synthesis of Nd-Fe-Co-B and Nd-Dy-Fe-Co-B based magnetic nanoparticles by the mechanochemical method. High coercivity $Nd_2(Fe,Co)_{14}B$ and $(Nd_{1-x}Dy_x)_2(Fe,Co)_{14}B$ hard magnetic nanoparticles were successfully synthesized. The effects of process parameters (i.e. the content of the dispersant CaO, milling time) have been studied and optimized. A kinetic model of the milling process was built based on both the experimental data and thermodynamic models. The influence of Dy alloying in $Nd_2(Fe,Co)_{14}B$ on the crystal structure and magnetic properties were studied and optimized. An analysis of the temperature dependent magnetic properties was employed to reveal the coercivity reversal mechanism of these magnetic particles.

Chapter 1 provides the rationale for this research. The problem statement, objective and scope, dissertation overview and findings and outcomes are introduced.

Chapter 2 reviewed the literature concerning the fundamentals of magnetism and discussed the state of art for the development of permanent magnetic materials. The effects of elemental substitution in Nd-Fe-B based alloys were discussed. The processing methods of Nd-Fe-B magnets were reviewed, with special attention paid to mechanical and mechanochemical processing. The questions yet to be addressed in the literature were discussed and the thesis work placed in the context of prior literature.

Chapter 3 discussed the rationale for the selection of the mechanochemical method. The experimental methodology, description of the synthesis and the characterization techniques

used in this project were described. The working principle and parameters used during characterization were also elucidated.

Chapter 4 elaborated the influence of the dispersant (CaO) content on the structure and magnetic properties of synthesized $Nd_2(Fe,Co)_{14}B$ magnetic nanoparticles. The observed effects of CaO content on the formation mechanism of $Nd_2(Fe,Co)_{14}B$ particles were also explained. With increasing CaO content (from 0 wt% till 50 wt%), the crystal size of $Nd_2(Fe,Co)_{14}B$ nanoparticles increased from 11 nm to 38 nm and enhanced coercivity value was observed. Increasing CaO content also delayed reduction, hence most of the reduction occurred during heat treatment rather than during milling.

Chapter 5 explained the mechanochemical milling process; three stages, i.e., amorphization, reduction, and steady-state, were observed. The milling kinetics can be predicted by a proposed thermodynamic model. The experimental data fits well with the model; milling efficiencies at a range of milling speeds were calculated from this model.

Chapter 6 discussed the effects of Dy-substitution on $(Nd_{1-x}Dy_x)_2(Fe,Co)_{14}B$ hard magnetic nanoparticles synthesized by the mechanochemical process. It was found that Dy homogeneously substituted for Nd in the $(Nd_{1-x}Dy_x)_2(Fe,Co)_{14}B$ particles. The coercivity and thermal stability improved with increasing Dy content. The coercivity reversal mechanism of these nanoparticles were analyzed through numerical models and it was found that nucleation of reversed domains was the controlling reversal mechanism.

Chapter 7 concludes the thesis and discusses future work.

1.4 Findings and Outcomes/Originality

This research led to several novel outcomes:

1. High coercivity $Nd_2(Fe,Co)_{14}B$ magnetic nanoparticles were synthesized for the first time by the "green" and low-cost mechanochemical process. The effect of the dispersant (CaO) content on the structure and magnetic properties were systematically

investigated for the first time. It was found that with increasing CaO content, from 0 wt% to 50 wt%, the crystal size of the synthesized $Nd_2(Fe,Co)_{14}B$ nanoparticles increased from 11 nm to 38 nm. An enhancement in coercivity from 4.5 kOe to 8.8 kOe was also observed. This result could be used to locate the optimum $Nd_2(Fe,Co)_{14}B$ nanoparticle size for enhanced hard magnetic properties. Increasing CaO content was also found to delay the reduction of the precursor oxides. With 50 wt% CaO content, the reduction was delayed until the heat treatment process. The optimum CaO content that should be used during the mechanochemical process was determined to be 50 wt%.

2. The reaction mechanisms and milling kinetics during the mechanochemical synthesis of $Nd_2(Fe,Co)_{14}B$ were identified and modeled. Three stages were observed during mechanochemical milling: 1. Amorphization of precursor oxides, 2. Reduction of precursor oxides, 3. Steady-state. A thermodynamic model was proposed to predict the reaction kinetics during milling. Good agreement was observed between this model and the experimental data. The milling efficiencies at different milling speeds were calculated from this model, the highest efficiency was found to be obtained at a milling speed of 550 rpm. These findings revealed for the first time the reaction mechanism and milling kinetics for the mechanochemical milling process for the synthesis of $Nd_2(Fe,Co)_{14}B$ nanoparticles, yielding understanding and control of this process.

3. The investigation of Dy-substitution of Nd in $(Nd_{1-x}Dy_x)_2(Fe,Co)_{14}B$ nanoparticles processed via the mechanochemical approach was carried out for the first time. It was found that Dy replaced Nd homogeneously in the nanoparticles. With increasing Dy content, the coercivity increased to a maximum of 17.8 kOe at $x = 0.5$. Improved thermal stability was also observed with Dy substitution. In addition, the coercivity reversal mechanism of the nanoparticles were analyzed. It was found that nucleation of reversed domains was the controlling reversal mechanism. This investigation provided an understanding of the influence of Dy-substitution in $Nd_2(Fe, Co)_{14}B$ nanoparticles through the mechanochemical process, and revealed the reversal mechanism of such nanoparticles for the first time.

References

[1] S. Hirosawa, M. Nishino, and S. Miyashita. *Advances in Natural Sciences: Nanoscience and Nanotechnology*. **2017**, 8, 013002.

[2] M. Sagawa, S. Fujimura, H. Yamamoto, Y. Matsuura, and K. Hiraga. *IEEE Transactions on Magnetics*. **1984**, 20, 1584-1589.

[3] J. J. Croat, J. F. Herbst, R. W. Lee, and F. E. Pinkerton. *Journal of Applied Physics*. **1984**, 55, 2078-2082.

[4] R. Coehoorn, D. De Mooij, and C. d. de Waard. *Journal of Magnetism and Magnetic Materials*. **1989**, 80, 101-104.

[5] E. F. Kneller and R. Hawig. *IEEE Transactions on Magnetics*. **1991**, 27, 3588-3560.

[6] R. Skomski and J. Coey. *Physical Review B*. **1993**, 48, 15812.

[7] T. Schrefl, J. Fidler, and H. Kronmüller. *Physical Review B*. **1994**, 49, 6100.

[8] W. B. Cui, Y. K. Takahashi, and K. Hono. *Advanced Materials*. **2012**, 24, 6530-6535.

[9] S. Shukla, A. Banas, and R. V. Ramanujan. *Intermetallics*. **2011**, 19, 1265-1273.

[10] T. Kolb *et al. 6th International Electric Drives Production Conference* **2016**, 34-40.

[11] X. Jilin, H. Zhengxian, L. Junming, and Z. Zhenchen. *Rare Metal Materials and Engineering*. **2015**, 44, 786-790.

[12] T.-H. Kim, J.-S. Oh, H.-R. Cha, J.-G. Lee, H.-W. Kwon, and C.-W. Yang. *Scripta Materialia*. **2016**, 115, 6-9.

[13] D. Brown, Z. Wu, F. He, D. Miller, and J. Herchenroeder. *Journal of Physics: Condensed Matter*. **2014**, 26, 064202.

[14] G. Sun, J. Chen, W. Dahl, H. J. Klaar, and W. G. Burchard. *Journal of Applied Physics*. **1988**, 64, 5519-5521.

[15] P. K. Deheri, V. Swaminathan, S. D. Bhame, Z. Liu, and R. V. Ramanujan. *Chemistry of Materials*. **2010**, 22, 6509-6517.

[16] H. Rahimi, A. Ghasemi, and R. Mozaffarinia. *Journal of Superconductivity and Novel Magnetism*. **2017**, 30, 475-481.

[17] H. X. Ma, C. W. Kim, D. S. Kim, J. H. Jeong, I. H. Kim, and Y. S. Kang. *Nanoscale*. **2015**, 7, 8016-8022.

[18] L. Yu, C. Yang, and Y. Hou. *Nanoscale*. **2014**, 6, 10638-10642.

[19] C. Yang and Y.-L. Hou. *Rare Metals*. **2013**, 32, 105-112.

[20] T. Tsuzuki and P. G. McCormick. *Journal of Materials Science*. **2004**, 39, 5143-5146.

[21] F. G. Tatiana, P. B. Antonina, and Z. L. Nikolai. *Russian Chemical Reviews*. **2001**, 70, 52-71.

[22] K. D. M. Harris. *Nature Chemistry*. **2013**, 5, 12-14.

[23] E. Boldyreva. *Chemical Society Reviews*. **2013**, 42, 7719-7738.

[24] A. Gabay and G. Hadjipanayis. *The Journal of the Minerals, Metals & Materials Society*. **2015**, 67, 1329-1335.

[25] M. E. McHenry, M. A. Willard, and D. E. Laughlin. *Progress in Materials Science*. **1999**, 44, 291-433.

[26] R. Cardias *et al. Scientific Reports*. **2017**, 7, 14878.

[27] C. B. Rong *et al. Journal of Physics D: Applied Physics*. **2013**, 46, 045001.

[28] E. Burzo. *Reports on Progress in Physics*. **1998**, 61, 1099.

[29] H. Rahimi, A. Ghasemi, R. Mozaffarinia, and M. Tavoosi. *Journal of Magnetism and Magnetic Materials*. **2017**, 424, 199-206.

[30] M. Sagawa *et al. Journal of Applied Physics*. **1987**, 61, 3559-3561.

[31] S. Zhou, C. Guo, and Q. Hu. *Journal of Applied Physics*. **1988**, 63, 3327-3329.

[32] O. Gutfleisch, M. A. Willard, E. Brück, C. H. Chen, S. Sankar, and J. P. Liu. *Advanced Materials*. **2011**, 23, 821-842.

Chapter 2

Literature Review

Due to its superior magnetic properties, various studies have been conducted on Nd-Fe-B hard magnets. This chapter first reviews the general concepts and fundamental aspects of hard magnets. After that, the influence of alloying on Nd-Fe-B type magnets is described. Progress in the processing of Nd-Fe-B type magnets via physical and novel chemical methods is discussed and analyzed. The inadequacy of the conventional methods in synthesizing nano-size or nanostructured magnetic particles is emphasized. The state-of-the-art for novel, cost-effective synthesis methods, especially the mechanochemical method, will be introduced. Its application to the synthesis of magnetic materials and importance as an industrially viable method is highlighted. Finally, the motivation of this study is presented.

2.1 Fundamentals of magnetism

In this section, an overview of the fundamentals of magnetism will be presented. The behavior and origin of different types of magnetisms in materials, including paramagnetism, ferrimagnetism, antiferromagnetism and ferromagnetism will be presented. The terminology and concepts in ferromagnetism will be introduced.

2.1.1 Magnetism

Magnetism refers to the phenomena arising from a force created by the presence of magnets, usually resulting in the attraction or repulsion of other materials. It originates from magnetic moments, which arise from the electronic configuration of each atom. The revolution of an electron around the atomic nucleus leads to a magnetic moment which is perpendicular to the orbit. The electron self-spinning phenomenon also generates a magnetic moment. From the Bohr model, the magnetic moment *μ(orbit)* induced by the electron revolution around the nucleus can be expressed as:

$$\mu(orbit) = \frac{neh}{4\pi m} \text{ (SI units)} \qquad (2.1)$$

where *h* is Planck's constant， *e* is the charge of an electron and *m* is the electron rest mass. For electrons in the first (*n*=1) Bohr orbit, $\mu(orbit) = 9.27 \times 10^{-24} A\,m^2$ (SI units).

The magnetic moment induced by electron spinning termed as *μ(spin).* Spin is an universal behavior of electrons at all temperatures. Electron spin is associated with a definite amount of magnetic moment, which was estimated theoretically and was found experimentally to be equal to:

$$\mu(spin) = \frac{eh}{4\pi m} \text{ (SI units)} = 9.27 \times 10^{-24} A\,m^2 \text{ (SI unit)} \qquad (2.2)$$

For each electron in an atom, the spin magnetic moment is $\pm\mu_B$ (+ for spin up, - for spin down).

The magnetic moment due to spin *μ(spin)* is thus equal to the magnetic moment due to orbital motion *μ(orbit)* in the first Bohr orbit. This is termed as the Bohr magneton μ_B. The total magnetic moment of an electron is the vector sum of *μ(orbit)* and *μ(spin)*. There are

numerous electrons within one atom, each spinning around its own axis and orbiting around the nucleus. Hence, the magnetic moment of an atom is equal to the vector sum of all the magnetic moments arising from each electron's motion. Two possibilities can occur for this summation:
All orbitals of the atom are filled by electrons and the magnetic moments of all the electrons cancel each other out. Hence, there's no net magnetic moment for the atom, which results in a diamagnetic material.

The magnetic moments of the electrons partially cancel each other, leaving a net magnetic moment for the atom. Substances made up of this kind of atoms are termed as para-, ferro-, antiferro- or ferrimagnetic materials.

Different types of magnetic materials are categorized according to this electronic behavior and interatomic exchange interactions (Figure 2.1). For diamagnetic materials, repulsion will be observed when an external magnetic field is applied, as the applied field reduces the effective current of a single electron orbit, creating a magnetic moment opposing the applied field [1].

Paramagnetic materials (Figure 2.1d) are weakly attracted to the external applied magnetic field, this attraction decreases with increasing temperature. In the absence of an external magnetic field, the magnetic moment in each atom is randomly oriented and cancels each other out, resulting in zero magnetization of the specimen. When a magnetic field is applied, these magnetic moments tends to align with the external field while thermal agitation tends to randomize this alignment. Hence, only partial magnetic moment alignment can be achieved, which results in small positive susceptibility. With increasing temperature, the value of the susceptibility decreases.

Ferromagnetic materials retain magnetization in zero applied magnetic field. With no applied field, the magnetic moment in each atom exchange interacts with the magnetic moment of other atoms and favors the parallel alignment of moments. This internal exchange interaction is very large and tries to keep the magnetic moments aligned even at

room temperature or elevated temperatures. However, when sufficiently high temperature is reached, the thermal energy can overcome this exchange energy, resulting in a ferromagnetic – paramagnetic transition in the material. This temperature is known as the Curie temperature T_C, and it can be used as a measure of the strength of the exchange interaction. Typical ferromagnetic materials include Fe, Co, Ni, etc.

Antiferromagnetic materials possess a small positive susceptibility at all temperatures and the susceptibility varies in a specific fashion with temperature. There are exchange interactions between the magnetic moments of the atoms. But these interactions favor an antiparallel alignment of the magnetic moments. When the temperature increases until thermal energy exceeds this exchange energy, the moments will be randomly oriented. This temperature is termed as the Neel temperature (T_N). Typical antiferromagnetic materials include MnO, FeO, CoO, NiO, etc.

In ferrimagnetic materials, due to the exchange interactions, the neighboring magnetic moments are also aligned in an antiparallel fashion, but the two opposing moments do not cancel, resulting in a net spontaneous magnetization. Macroscopically, such materials behave like ferromagnetic materials but the magnetization tends to be smaller. Typical examples include Fe_3O_4, Fe_2O_3 and spinel ferrites.

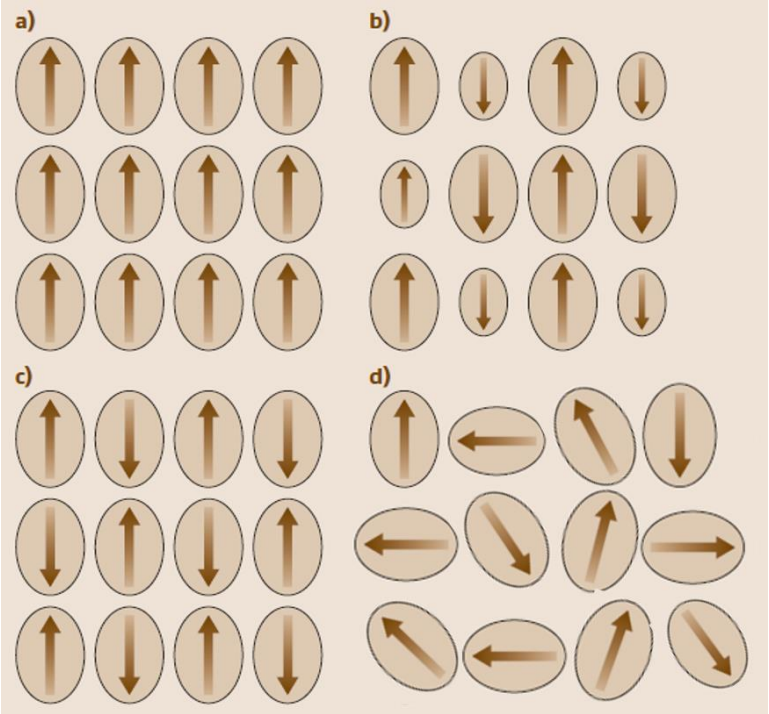

Figure 2.1. Illustration of magnetism in (a) ferromagnetic materials, (b) ferrimagnetic materials, (c) antiferromagnetic materials and (d) paramagnetic materials /ferromagnetic materials above T_c.

2.1.2 Fundamental concepts in permanent magnetic materials

In this section, the fundamental concepts of magnetism, including exchange interactions, magnetic anisotropy, thermal stability, coercivity reversal mechanism and the origin of hysteresis loops will be introduced and discussed. Their influence on permanent magnetic materials, especially NdFeB will be emphasized.

2.1.2.1 Exchange interactions

In the previous section, the different categories of magnetism have been discussed. For ferromagnetic or antiferromagnetic materials, the magnetic moments within these materials are coupled in either parallel (↑↑) or antiparallel (↑↓) fashion. This coupling originates from the exchange interactions. There are two main types of exchange interactions, 1. intra-

atomic exchange interactions which determine the atomic moments, 2. interatomic exchange interactions which influences the interactions between neighboring magnetic atoms.

The intra-atomic exchange interactions are usually predictable by Hund's rules, which favors parallel spin and determines the atomic magnetic moment. However, the inter-atomic exchange interactions are more difficult to predict. If the inter-atomic exchange interactions are considered as Heisenberg interactions, the energy associated with this interaction can be expressed as:

$$E_{ex} = -2J_{ex}S_1S_2cos\theta \quad (2.3)$$

where J_{ex} is the exchange integral, θ is the angle between two neighboring spins S_1 and S_2. If the exchange interaction J_{ex} is positive, a spontaneous parallel alignment of magnetic moments will be observed. All ferromagnetic materials behave in this manner below their Curie temperatures. If the exchange interaction J_{ex} is negative, spontaneous antiparallel alignment of magnetic moments will be favored. Antiferromagnetism will be observed if the magnetic moments cancel each other out, with zero net moment. On the other hand, ferrimagnetism will be observed if the moments do not cancel each other out, resulting in a non-zero spontaneous net magnetic moment.

2.1.2.2 Magnetic anisotropy

Magnetic anisotropy refers to the phenomenon in which the magnetic energy varies, depending on the different crystallographic direction. Hence the ease of magnetization varies in different direction. The axis which permits the easiest magnetization is called the easy axis, the direction associated with the most arduous magnetization is the hard axis. The energy required to rotate the magnetization from the easy axis direction is termed as the anisotropy energy, and can be expressed as:

$$E_a = K_1Vsin^2\theta$$

where K_1 represents the anisotropy constant, V indicates the magnetic volume and θ refers to the angle between the easy axis and the magnetization axis.

There are various factors which contribute to magnetic anisotropy, including crystal anisotropy (or magnetocrystalline anisotropy) and shape anisotropy. Crystal anisotropy results from the fixed arrangement of atoms within a lattice structure, hence magnetic properties vary with crystallographic direction. This effect can be explained physically by the spin-orbit interactions of electrons within an atom. There is coupling between the spin and the orbital motion of each electron. The spin of the electron will be reoriented under an applied external magnetic field, which also influences the orbit of the electron. However, the orbit of an electron is strongly bound to the lattice, hence it also resists spin reorientation. Therefore, energy, termed as the anisotropy energy is required to overcome this spin-orbit interaction and reorient the spin from the easy axis direction. The crystal anisotropy is an intrinsic property of the material and it is temperature dependent. Typically, it decreases with increasing temperature and vanishes near the Curie temperature.

Shape anisotropy, on the other hand, is an extrinsically shape dependent property. It originates from the demagnetizing effect. For example, for a needle shape magnet, the demagnetizing field is lower along the long axis, therefore the easy axis lies along the long axis.

For a polycrystalline material consisting of randomly oriented crystals, the individual anisotropy will average out, leading to zero anisotropy in the bulk. However, for a polycrystalline material with a preferred orientation or texture, the anisotropy of individual grains cannot cancel out. The overall anisotropy will be the weighted average of the relevant anisotropy in individual crystals. Texture or preferred orientation can be induced via different processing routes or shaping.

2.1.2.3 Thermal property

The magnetic properties of all materials, other than diamagnetic materials, are determined by the competition between the exchange energy which orders the system and thermal agitation which tend to disorder the system. For ferromagnetic materials, the Curie

temperature (T_C) and the temperature coefficients (α and β) can describe their thermal properties.

The Curie temperature marks the point where the effect of thermal agitation overrides the effect of exchange interactions, and the behavior of the material changes from ferromagnetism to paramagnetism. In other words, the ferromagnetic exchange interactions set the scale of T_C. The Curie temperature (T_C) can be related to exchange energy via the expression below:

$$T_C = \frac{2ZJ_{ex}S(S+1)}{3k_B} \tag{2.4}$$

Where J_{ex} represents the strength of the exchange interaction, S refers to the total spin angular momentum, Z represents the nearest neighbor coordination number and k_B is the Boltzmann constant.

A Bethe-Slater curve is constructed to empirically relate the variation of the exchange energy to the interatomic distance (Figure 1.3). Important information on the influence of alloying on the Curie temperature of ferromagnetic materials can be provide with Equation 2.4 and this curve [2, 3].

Although the Curie temperature identifies the temperature at which thermal agitation overrides magnetic exchange interactions, it cannot provide information on how thermal agitation influences the magnetic properties. The temperature coefficient of coercivity (α) and the temperature coefficient of remanence or magnetization (β) are widely used to quantify reversible changes of magnetic properties due to thermal effects. These temperature coefficients in the temperature range between two temperatures, say T_1 and T_2, can be calculated by the following expressions:

$$\alpha(H_C) = \frac{H_C(T_2) - H_C(T_1)}{H_C(T_1)(T_2 - T_1)} \times 100\% \tag{2.5}$$

$$\beta(M_r) = \frac{M_r(T_2) - M_r(T_1)}{M_r(T_1)(T_2 - T_1)} \times 100\% \tag{2.6}$$

Table 2.1 lists the Curie temperature (T_C) and thermal coefficients (α and β) of select conventionally processed magnets.

Table 2.1. Magnetic properties of selected commercial permanent magnets.

Magnets	Processing method	B_r	H_C	$(BH)_{max}$	T_C	$\alpha(H_C)$*	$\beta(B_r)$*	Ref.
		T	kA/m	kJ/m^3	^{0}C	%/^{0}C	%/^{0}C	
Alnico	Cast	1.3	60	55.5	~ 850	-0.02	-0.02	[4]
	Sintered	0.85~0.9	115~127	35.8~63.3	~ 850	-0.02	-0.02	[5]
Barium ferrite	Sintered	0.38	180	27	~450	+0.3	-0.2	[6]
Strontium ferrite	Sintered	0.4	275	30	~450	+0.3	-0.2	[7]
Sm_2Co_{17}	-	0.96	1600	175	~825	-0.19	-0.035	[8]
$SmCo_5$	-	0.85	1750	155	~825	-0.19	-0.04	[8]
Nd-Fe-B	Sintered	1.43	950	398	~310	-0.49 ~ -0.53	-0.1	[9-11]
	Die upset	1.31	1280	334	~310	-0.45	-0.16	[12]

2.1.2.4 Hysteresis

Hysteresis (or irreversibility) occurs in ferro- and ferromagnetic materials. After the material is field-saturated, removal of the applied field leaves behind a non-zero remanence magnetization. It was first measured and documented by Ewing in 1885 [13]. The specimen is first placed in zero external magnetic field (H) and at this stage, both the magnetization (M) and polarization (J) is zero. The external magnetic field (H) is increased from zero to a magnitude which can align all the magnetic moments in the direction of the external field (saturation field (H_S)). M and J increase until they reach their saturation value, i.e., saturation magnetization (M_S) and saturation polarization (J_S).

When the applied field is decreased from H_S to zero, the values of both M and J decrease, however the resultant reverse B-H and J-H curve does not follow the original curve (dotted lines) and a finite value of B/J is associated with this sample, termed as remanence

magnetization Br or Jr. The difference between the forward and reverse magnetization curve is known as hysteresis. The magnitude of external field which can bring the value of B/J back to zero is termed as the intrinsic coercivity. The saturation magnetization and intrinsic coercivity are intrinsic properties of the magnet, which can be related to the composition and temperature. Another important parameter, i.e. $(BH)_{max}$, which is shown in the blue shaded area in Figure 2.2. It is calculated from the maximum B×H value in the second quadrant of the B-H curve. With higher $(BH)_{max}$, a larger amount of energy will be stored in the magnet, hence more useful work will be done. The value of $(BH)_{max}$ depends not only on B_r and H_c, but also on the shape of the hysteresis loop. A square loop results in higher $(BH)_{max}$. For example, in a magnetically aligned Nd-Fe-B magnet, $(BH)_{max}$ will be larger in a direction parallel to the alignment direction [14].

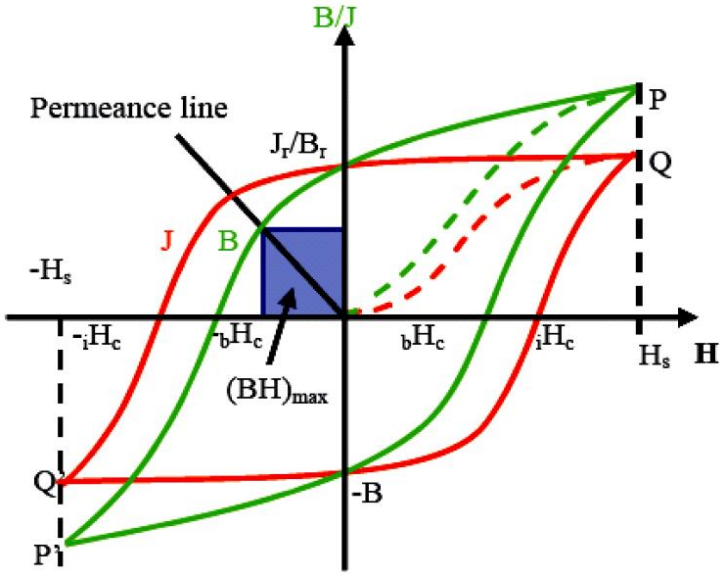

Figure 2.2.B-H and J-H hysteresis loops [15].

2.1.2.5 Coercivity reversal mechanism

Coercivity, the reverse field required to obtain magnetization reversal, is one of the most important indicators of a permanent magnet. It is an extrinsic property of the magnets and originates from the crystal structure and microstructure of the magnets. Different types of magnets usually have different coercivity origins, hence, similar microstructures may lead to different influences on coercivity. For example, lattice defects tend to increase coercivity

of soft magnetic materials, they can act as pinning points during domain wall movement. However, lattice defects in hard magnetic materials may decrease coercivity values, some defects decrease magnetocrystalline anisotropy within the crystal structure and are the weak points in the magnetic reversal process [6].

For hard magnetic materials, especially Nd-Fe-B, the origin of high coercivity arises from the strong magnetocrystalline anisotropy, which prevents coherent rotation during magnetization reversal [16]. However, if magnetization reversal involves only coherent rotation, the intrinsic coercivity of the material should be equal to its anisotropy field (Equation 2.7). This is the explanation of coercivity in the Stoner and Wohlfarth model where magnetization reversal is accomplished by coherent rotation of all magnetic moments [7].

$$H_{ci} = H_A \tag{2.7}$$

However, for all permanent magnetic materials, the measured coercivity values are far inferior to their $\boldsymbol{H_A}$ values. For example, $\boldsymbol{H_A}$ is ~ 73 kOe for $Nd_2Fe_{14}B$ at room temperature. If the shape anisotropy is excluded, the coercivity of a $Nd_2Fe_{14}B$ particle should be:

$$H_{ci} = H_A - N(4\pi M_s) \tag{2.8}$$

where N indicates the demagnetization factor. For spheres, N = 1/3, the corresponding H_{ci} of this magnet should be ~ 70 kOe, which is much larger than the maximum coercivity of an aligned $Nd_2Fe_{14}B$ magnet (~ 20 kOe). This disparity is also observed in other hard magnets and is known as the Brown Paradox (Figure 2.3).

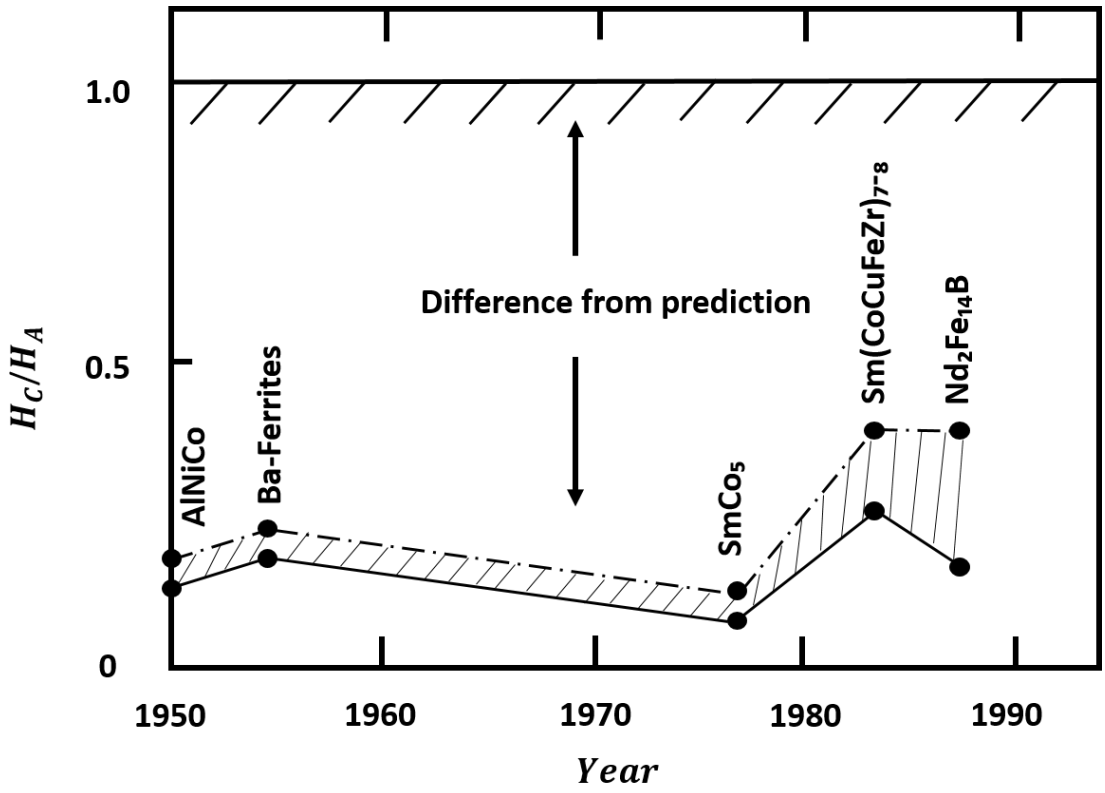

Figure 2.3. Critical fields of magnets compared to their anisotropy field H_A[16].

This difference between the coercivity value and the anisotropy field suggests the existence of incoherent reversal processes due to the heterogeneous microstructure, including defects such as grain boundaries, in hard magnetic materials. Givord et. al. [17] categorized the reversal process as follows:

1. Nucleation of a magnetic moment reversal site and the formation of a domain wall at the defect region.
2. Passage of the domain wall from the defect region to the principal hard magnetic phase.
3. Propagation of the domain wall within the principal phase.
4. Pinning and de-pinning of the domain wall on defect sites.
5. Complete magnetization reversal.

There is an associated critical field which allows the process to go from one stage to the subsequent stage. Both nucleation of reverse sites and pinning of domain wall can exist in the same material during its magnetization reversal, the controlling mechanism is

determined by the microstructure of the hard magnetic material [16, 18]. Nucleation of reversed sites usually starts at surface irregularities and impurities with low anisotropy, and is widely used to explain the behaviour of sintered Nd-Fe-B magnets [19, 20]. The domain wall pinning process indicates that impurities within the magnetic phase prevent/slow down domain wall motion, increasing H_C. This process was found to relevant to the behaviour of melt spun Nd-Fe-B ribbons and Sm-Co magnets.

The coercivity mechanism of magnets are closely related to its type, preparation process as well as microstructure. Although the coercivity mechanism of most conventional permanent magnets are well studied, the mechanism is not yet well established for novel magnets or magnets processed by novel processing routes. Researchers are studying the coercivity mechanism of materials processed by various processing routes. For example, Lisfi et al. found that domain wall pinning is responsible for magnetization reversal in $L1_0$ FePt thin films prepared by sputtering [21]. A combination of strong domain-wall pinning and nucleation of reversed domains was found in melt-spun $(Nd_{0.8}Ce_{0.2})_{2.4}Fe_{12}Co_2B$ melt-spun ribbons by Li et al. [22]. Domain wall pinning was found to be the controlling coercivity mechanism in $Sm_{1-x}Pr_xCo_5$ nanoflakes processed by surfactant assisted ball milling [23]. Tan et al. proposed a combined effect of domain wall pinning and magnetic interactions in bulk $Nd_{60}Fe_{30}Al_{10}$ magnets [18].

Although it was widely accepted that the coercivity mechanism of sintered Nd-Fe-B is nucleation of reversed domains and that of melt-spun Nd-Fe-B alloy is domain wall pinning, the coercivity mechanism for Nd-Fe-B synthesized by other processing routes and for Nd-Fe-B nanoparticles is still under debate. Understanding the coercivity mechanism has a substantial impact on developing and improving Nd-Fe-B through novel and cost-effective methods. The magnetic hysteresis loop can provide information on the magnetization reversal process and aids in coercivity mechanism analysis. Several numerical models have also been put forward and are presented in the following section.

The magnetic hysteresis loop illustrates the direct influence of an external magnetic field on coercivity and shows the magnetization and magnetization reversal process for the

magnet. The initial magnetization curve provides valuable information on the coercivity mechanism. A high initial susceptibility is expected for nucleation-type magnets while a low initial susceptibility is observed in pinning-type magnets (Figure 2.4). However, the shape of the initial magnetization curve only provides qualitative information on the type of magnet, hence numerical methods have also been developed to identify the types of magnets.

There are 4 types of commonly used numerical models, they can be used separately or combined. The methods include temperature dependence of the coercive field, magnetic viscosity, activation volume analysis, evaluation of the dipolar contribution to magnetization reversal, and the angular dependence measurement of the coercive field. Due to the ease of measurement, the temperature dependence of the coercive field analysis is widely used. It will be illustrated in the following section.

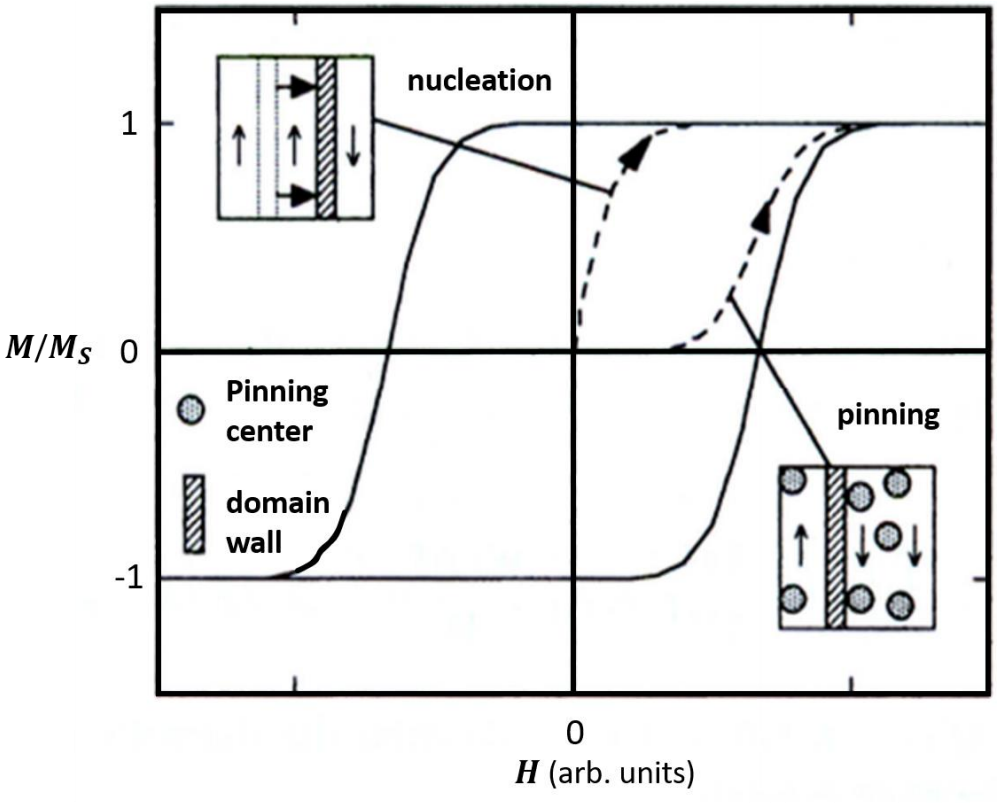

Figure 2.4. Difference in initial magnetization curve in pinning and nucleation-type magnets [24].

Measuring of temperature dependent coercivity

The coercivity value H_c is highly sensitive to microstructure. The coercivity can be described by Brown's equation, based on a nucleation type coercivity mechanism. If the demagnetization process of these samples are governed by the nucleation field, a modified form of Brown's equation can be used to describe the temperature dependence of coercivity, as described below [22, 25, 26]:

$$\mu_0 H_c(T) = \alpha_K \mu_0 H_N^{min}(T) - N_{eff} M_s(T) \quad (2.9)$$

Where $H_c(T)$ is the coercivity measured at different temperatures, $H_N^{min}(T)$ is the minimum nucleation field, α_K and N_{eff} are microstructure related parameters, $M_s(T)$ is the spontaneous magnetization at different temperatures [27]. Due to the difficulty in finding the H_N^{min} value, a simpler version of this equation is often employed to analyze the temperature dependence of H_c.

$$\mu_0 H_c(T) = \alpha H_A(T) - N M_s(T) \quad (2.10)$$

In Equation (2.10), $\alpha H_A(T)$ is interpreted as the nucleation field of a reverse domain, $N M_s(T)$ describes the average local demagnetizing effects. It was reported that the α value varies with grain size and that the N value varies with the smoothness of the grain boundaries [19, 20]. This equation is relevant to a nucleation-controlled mechanism [16]. From this equation, a straight line should be resulted from a $\frac{\mu_0 H_c(T)}{M_s(T)}$ vs. $\frac{\mu_0 H_A(T)}{M_s(T)}$ plot, with a slope of α and an intercept of $-N$.

The fitting of temperature dependent magnetic properties can also be tested by a pinning dominated model [28], as shown below.

$$\left(\frac{H_C}{H_0}\right)^{1/2} = 1 - \left(\frac{75 k_B T}{4bf}\right)^{2/3} \quad (2.11)$$

where H_c is the coercivity, H_0 is the critical field in the absence of thermal activation, k_B is the Boltzmann constant, $4b$ is the interaction range of a pin equating with the domain wall width and f is the maximum restoring force per pin. All parameters (except H_c and T) are constants for a given sample. Thus, for a pinning dominated magnet, a linear relationship should be obtained in the $(H_c)^{1/2}$ versus $(T)^{2/3}$ plot.

2.2 Permanent magnetic materials

An overview of types of permanent magnetic materials in the market and their magnetic properties is presented in this section, with an emphasis on Nd-Fe-B type permanent magnetic materials.

2.2.1 Overview of permanent magnetic materials

Permanent magnetic materials are characterized by their high anisotropy field, high coercivity, and large energy product $(BH)_{max}$. A large external magnetic field is required to fully saturated them. Once saturated, part of the magnetization is retained after removal of the external field. They are widely used and extremely useful in energy conversion systems, such as motors, generators, wind turbines, etc. [29, 30]. The first known permanent magnet is lodestone, which is an impure form of iron oxide, and the ancient Chinese used it as a compass in navigation thousands of years ago. The major breakthrough of permanent magnets was after the discovery of Alnico (Fe-Al-Ni-Co) in 1932 by Mishima. The early Alnico magnets possess a typical coercivity of ~ 600 Oe and energy product of ~ 1MGOe. Their coercivity values nearly doubled that of the best magnet steel at that time. They have been widely used in a wide range of areas since their discovery, including loud speakers, motors etc. Alnico has been partially replaced by ferrites or rare-earth based magnets.
After Alnico, barium ferrite ($BaO{\bullet}6Fe_2O_3$) became the next popular commercial magnet material with a typical (BH)max of ~ 3.5 MGOe. This material is very brittle and its magnetic properties haven't improved for many years.

A remarkable improvement in permanent magnets was achieved by the discovery of high magnetocrystalline anisotropy $RECo_5$, especially $SmCo_5$. These rare earth transition metal magnets possess high coercivity and good temperature stability, as the 3d-3d exchange interactions stabilize the magnet ordering against temperature, while the 4f-3d interaction provides high anisotropy.

The most important progress in permanent magnetic materials so far is the discovery of ternary Nd-Fe-B alloys in 1983 [31, 32]. Nd-Fe-B based magnets are considered as the 3rd generation rare earth permanent magnets. They possess the highest energy product among all known magnets. In this ternary magnet system, the 3d orbital of Fe provides large magnetization and useful Curie temperature, while the 4f orbital of Nd gives rise to large magnetocrystalline anisotropy.

Although Nd-Fe-B type magnets possess high energy product, the search for next generation permanent magnet has never been stopped, especially in the area of rare earth lean permanent magnets. Among all the newly investigated magnets, Sm-Fe-N shows some promising properties. Sm-Fe-N powders possess (BH)max of ~25 MGOe, and have been considered as a high-performance permanent magnet comparable to Nd-Fe-B. However, due to the poor thermal stability of Sm-Fe-N powder, bulk magnets cannot be produced by conventional processing methods. Though non-conventional consolidation techniques such as shock compaction, compression shearing, spark plasma sintering have been utilized, the coercivity of bulk magnets are still much lower than the original powder [33, 34].

The evolution of permanent magnets and their respective (BH)max is shown in Figure 2.5: It is worth noticing that in 2002, high energy product exchange coupled Fe_3O_4/FePt was synthesized with (BH)max of ~ 21 MGOe, exceeding the single phase FePt assembly by 37% [35].

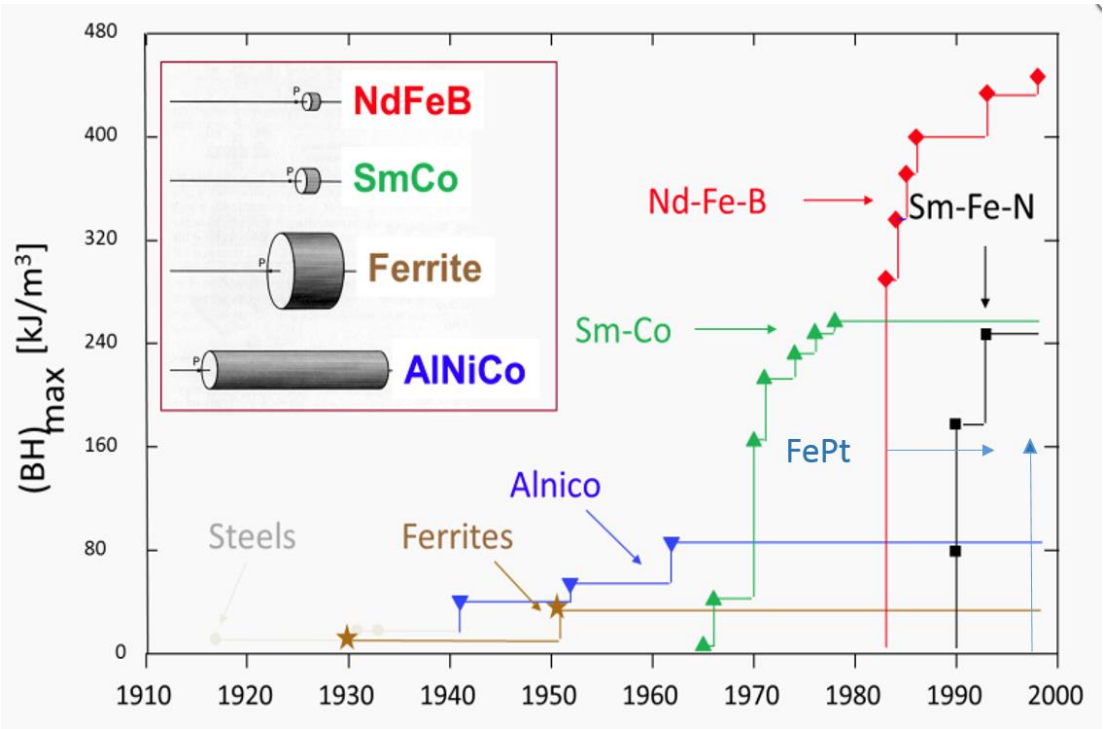

Figure 2.5. Development of the energy product $(BH)_{max}$ of permanent magnets at room temperature and comparison of energy density of various magnets [36].

2.2.2 Nd-Fe-B type permanent magnetic materials

Nd-Fe-B type permanent magnets have a majority phase of $Nd_2Fe_{14}B$. These magnets were independently developed by General Motors and Sumitomo Special Materials [31, 32]. The discovery of Nd-Fe-B type permanent magnets is the most important milestone in permanent magnet history. The commercial Nd-Fe-B type permanent magnet today exhibits a high energy product (BH)max of ~ 52 MGOe and a Curie temperature of ~ 310 ^{O}C. Due to its superior magnetic properties, it soon replaced other magnets in various high-end applications, including electric cars, hard disk motors, wind turbines, magnetic resonance imaging (MRI) machines, etc [36-39]. The origin of these excellent magnetic properties is mainly due to two reasons: 1. high magnetocrystalline anisotropy which give rises to large coercivity; 2. large magnetic dipole moment which provides high saturation magnetization. The properties of Nd-Fe-B type magnet depend on alloy composition, microstructure as well as processing technique.

The crystal structure of $Nd_2Fe_{14}B$ was first revealed through neutron-diffraction studies using the Rietveld method. $Nd_2Fe_{14}B$ crystallizes in a tetragonal unit cell (space group $P4_2/mnm$) having four formula units with 68 atoms per unit cell, with a typical lattice constant a = 0.882 nm, c = 1.224 nm (Figure 2.6) [40].

The $Nd_2Fe_{14}B$ crystal structure is a layered structure: there are eight vertically stacked layers, the Nd layers (in which all the B atoms are located) are separated by Fe layers, where almost all the Fe atoms are located. There are six crystallographically different ion sites, two rare earth sites and one boron site in the trigonal prisms which contain boron atoms (Figure 2.6). The boron atom occupies the center of this trigonal prism formed by three nearest iron atoms above, and three below the basal plane. These prisms link the Fe layers to Nd and B and contribute to the stability of the tetragonal structure [41, 42].

The crystal structure of $Nd_2Fe_{14}B$ determines its intrinsic properties. The Curie temperature (T_C) is determined by collective exchange interactions between the Fe-Fe, Fe-Nd and Nd-Nd pairs of atoms. However, the magnet moment in Nd atoms arise from 4f electrons, which have an electric shell thickness of ~ 0.03 nm, which is much smaller than the interatomic spacing in Nd-Nd or Nd-Fe atomic pairs (~0.3 nm). Hence, there is a negligible contribution from these atomic pairs and the main contribution towards T_C is Fe-Fe exchange interactions. The magnet moment in Fe atoms mainly arises from 3d electrons, with a radius of 0.125 nm. If the interatomic spacing between Fe-Fe atoms is larger than 0.25nm, positive exchange interactions occur. Negative exchange interactions occur for spacings less than 0.25 nm. These positive and negative effects oppose each other, leading to weak overall exchange interactions, resulting in relatively low T_C of ~ 310 °C. The large magnetocrystalline anisotropy of $Nd_2Fe_{14}B$ mainly results from Nd atoms. The coercivity is dramatically enhanced through the interaction of anisotropic 4f electron clouds with the crystal electric field of surrounding charges. This interaction and the spin-orbit coupling yields a preferential alignment of the Nd magnetic moments along a specific crystalline direction and pinning of the moments [43]. The uniaxial magnetic anisotropy of $Nd_2Fe_{14}B$ can be expressed by:

$$E_a = K_1 V sin^2\theta + K_2 V sin^4\theta + K_3 V sin^4\theta sin4\varphi \quad (1)$$

where θ and φ are the magnetization angles with respect to the easy axis. The first order anisotropy constant K_1 is negative at 4.2 K and increases with temperature and becomes positive at 133 K, the second order anisotropy constant K_2 and third order anisotropy constant K_3 are positive at 4.2 K and reduce to a value close to zero at room temperature.

The saturation magnetization (M_s) of $Nd_2Fe_{14}B$ is mainly contributed by the magnetic moment of Fe atoms. The magnetic moment is different for Fe atoms at different crystallographic sites. Fe at $8j_2$ sites have the highest moment of 2.8 μ_B, 4c sites have a lower magnetic moment of 1.95 μ_B.

A summary of the intrinsic magnetic properties of $Nd_2Fe_{14}B$ is listed in Table 2.2:

Table 2.2. The intrinsic properties of $Nd_2Fe_{14}B$ [41].

Temperature	Anisotropy (room temperature)			Magnetization
T_C	K_1	K_2	$\mu_0 H_a$	J_s
310 ^{0}C	4.2 MJ/m^3	0.7 MJ/m^3	6.7 T	1.61 T

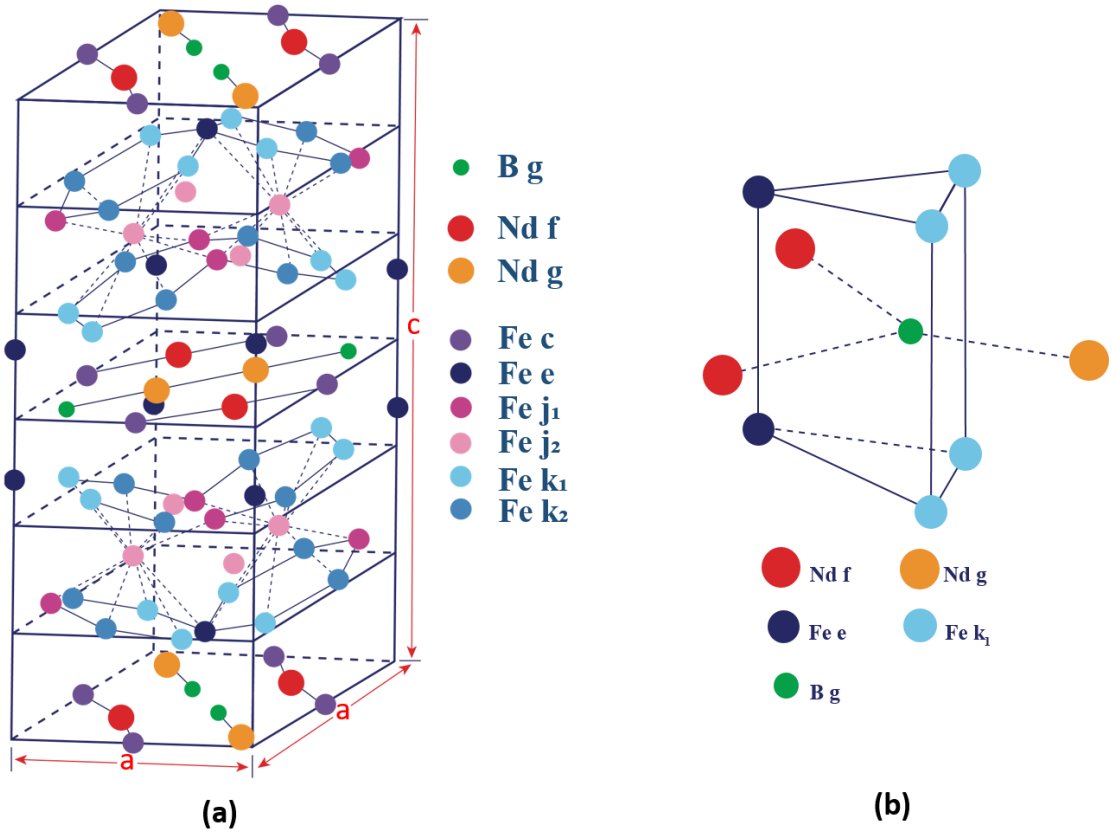

Figure 2.6. (a) Unit cell of tetragonal $Nd_2Fe_{14}B$, (b) the boron atom sits inside the trigonal prism in the $Nd_2Fe_{14}B$ structure [40].

2.3 Alloying effects

Considerable attention has been paid to improve magnetic properties by composition modification via different processing methods. Usually Nd and Fe are substituted by other elements to increase e.g., coercivity, anisotropy, Curie temperature or thermal stability. However, the substitution of one element may lead to an increase of one property but also the deterioration of some other properties. Hence, co-substitution is commonly performed in Nd-Fe-B based magnets. In this section, alloying effects will be introduced.

2.3.1 Substitution of Nd

Rare earth elements (R = La, Ce, Pr, Sm, etc) can fully replace Nd in the tetragonal $Nd_2Fe_{14}B$ structure, and their influence on magnetic properties has been studied [41]. A

summary of the magnetic properties of various $R_2Fe_{14}B$ compounds was made by Herbst et. al. and listed in Table 2.3. The magnetic properties of the $(R,Nd)_2Fe_{14}B$ phases can be estimated by a simple linear approximation through the rule of mixtures. The recent rare earth crisis in 2010 again motivated interest to look for more abundant and low-cost alternatives to Nd. Light rare earth elements, such as Ce and La, drew considerable attention. However, the intrinsic magnetic properties, including spontaneous magnetization (Js) and anisotropy field (H_a) of $Ce_2Fe_{14}B$/ $La_2Fe_{14}B$ are far inferior to those of $Nd_2Fe_{14}B$. If they were used to replace Nd, microstructural optimization needs to be done to improve the extrinsic properties, especially coercivity. Ito et. al. put forward a method to infiltrate Nd-Cu into the grain boundary of hot deformed $(Ce, Nd)_2Fe_{14}B$ magnets, forming a $(Ce, Nd)_2Fe_{14}B$ core-shell structure, whereby the $(Ce, Nd)_2Fe_{14}B$ core is separated by a non-magnetic grain boundary phase. The coercivity of the infiltrated core-shell structure was found to improve the coercivity [44]. Various novel microstructures have been investigated to improve the magnetic properties of La/Ce substituted $R_2Fe_{14}B$. For example, an inhomogeneous distribution of La/Ce into the 2:14:1 phase helps to promote exchange coupling and results in high $(BH)_{max}$ [45], Ce-Co co-alloying in Nd-Fe-B permanent magnets helps to enhance the high temperature magnetic properties [46]. With a specific La:Ce ratio of 1:3 and Nd concentrated in the grain boundary region, Toyota announced in Feb 2018 that they obtained a neodymium-reduced, heat-resistant magnet for electric motor applications.

Besides the light rare earth elements, scientists found that heavy rare earth elements, especially Tb and Dy, can greatly enhance thermal stability of $Nd_2Fe_{14}B$ while maintaining the $(BH)_{max}$ value. Tb and Dy are still the indispensable alloying elements in $Nd_2Fe_{14}B$ magnets for high temperature applications [47-53]. 10-15 wt% Dy/Tb is commonly required to compensate the deterioration in coercivity of Nd-Fe-B magnets due to elevated operating temperatures of ~ 200 °C. Because of the high price volatility and the forecasted long term criticality of heavy rare earth elements, this amount will be expensive and a concern in the supply of permanent magnets. Therefore, the reduction of Dy and other heavy rare earth elements in Nd-Fe-B magnets without losing magnetic performance is an important subject of permanent magnet research. Researchers have tried various methods

to reduce Tb/Dy content in Nd-Fe-B based magnets. Most of these methods are physical processing methods.

Sagawa and Fujimoto of Intermetallics Co. Ltd, Kyoto, Japan patented a method for producing NdFeB sintered magnet having high coercivity and high squareness. This method consists of forming a layer containing Dy and/or Tb on the surface of NdFeB sintered magnet base material and then performing grain boundary diffusion to diffuse Dy and/or Tb by heating the material to a temperature equal to or lower than the sintering temperature[54]. Oono et al. present a novel grain boundary diffusion (GBD) treatment with a Dy-Ni-Al eutectic alloy powder, which allowed Dy to penetrate into sintered Nd-Fe-B plates with 5mm thickness [55]. As the GBD treatment allows preferred Dy distribution to improve coercivity without any marked decrease in remanence, other researchers investigated the effects of GBD with different Dy containing alloy systems, including Pr-Cu, Dy-Cu and Pr-Dy-Cu[56], Dy-Fe-Cu[57], DyF_3[58-60] and DyNiAl[61]. The coercivity enhancement mechanism of the GBD process on sintered Nd-Fe-B magnets has been studid. It was found that the formation of a $(Nd,Dy)_2Fe_{14}B$ shell in the outer region of the $Nd_2Fe_{14}B$ grains and the presence of a Nd-Dy rich phase in the grain boundary region increased coercivity. The former increased the nucleation field from GBs and the latter weakened intergranular exchange coupling, both these factors contributed to property enhancement [62, 63]. Beneficial property changes were also found in Dy_2O_3 alloyed Nd-Fe-B magnets[64].

Table 2.3. Magnetic properties of the $R_2Fe_{14}B$ alloys [41].

	4 K			295 K			
Compound	M_s (μ_B/f.u.)	$4\pi M_s$ (kG)	H_a (kOe)	M_s (μ_B/f.u.)	$4\pi M_s$ (kG)	H_a (kOe)	T_C (K)
$La_2Fe_{14}B$	30.6	14.8	12	28.4	13.8	20	530
$Ce_2Fe_{14}B$	29.4	14.7	26	23.9	11.7	26	424
$Pr_2Fe_{14}B$	37.6	18.4	~200	31.9	15.6	75	565
$Nd_2Fe_{14}B$	37.7	18.5	~170	32.5	16.0	73	585
$Sm_2Fe_{14}B$	33.3	16.7	>200	30.2	15.2	>150	616
$Gd_2Fe_{14}B$	17.9	9.2	19	17.5	8.9	24	661
$Tb_2Fe_{14}B$	13.2	6.6	~300	14.0	7.0	~220	650
$Dy_2Fe_{14}B$	11.3	5.7	~170	14.0	7.1	~150	598
$Ho_2Fe_{14}B$	11.2	5.7	>100	15.9	8.1	75	573
$Er_2Fe_{14}B$	12.9	6.6	~260	17.7	9.0	8	554
$Tm_2Fe_{14}B$	18.1	9.2	~170	22.6	11.5	8	541
$Yb_2Fe_{14}B$	~23	~12		~23	~12		524
$Lu_2Fe_{14}B$	28.2	14.7	20	22.5	11.7	26	535
$Y_2Fe_{14}B$	31.4	15.9	18	27.8	14.1	26	565
$Th_2Fe_{14}B$	28.4	12.2	~20	24.7	14.1	26	481

2.3.2 Substitution of Fe

One major disadvantage of Nd-Fe-B permanent magnets is their low Curie temperature and poor thermal stability, as explained in the previous section. Substitution of Fe by most of the transition metal elements has been investigated to mitigate this problem. Co can substitute for the Fe in $Nd_2(Fe_{1-x}Co_x)_{14}B$ tetragonal structure in the entire range of $0 \leq x \leq 1$. Co substitution of Fe can significantly enhance Curie temperature, with a minor decrease in coercivity [30, 65, 66]. The increase in Curie temperature led to an enhancement in the temperature coefficients. The thermal coefficient of remanent magnetization α decreased from ~0.12%/K for $x = 0$, to ~0.08%/K for $x = 0.1$ and ~0.06%/K for $x = 0.2$[67]. The maximum room temperature magnetization of $Nd_2(Fe_{1-x}Co_x)_{14}B$ occurred at x of ~ 0.1. This improvement is expected by analogy to the $R(Co_{1-x}Fe_x)_2$ and $R_2(Co_{1-x}Fe_x)_{17}$ systems. In the $R_2(Co_{1-x}Fe_x)_{17}$ system, the maximum saturation magnetization is found at x of ~ 0.4, while similar behavior is found in the $Co_{1-x}Fe_x$ binary system[67]. This phenomenon was explained by the rigid band model. With the substitution of Co in Fe, the electrons first fill in the up-spin half of the *d* band. With further Co substitution, the down-spin band begins to fill, lead to a decrease in net magnetic moment. However, in Fe-Co-B ternary systems,

saturation magnetization decreased monotonically with Co substitution. This is because B acts as an electron donor and the up-spin band of the Fe *d* band is entirely filled even in the absence of Co [68, 69]. In the case of $Nd_2(Fe_{1-x}Co_x)_{14}B$, researchers believe that it behaves in between the above two cases. The B content in this alloy system is lower than that in Fe-Co-B alloys, hence the up-spin band is not entirely full. This leaves room for additional electrons to be transferred from Co atoms, leading to maximum saturation magnetization at a relatively small substitution content *x* of ~ 0.1. Due to the decrease of anisotropy and saturation magnetization by further Co substitution, a reasonable substitution range of $x \leq 0.2$ is usually selected for commercial sintered Nd-Fe-B magnets [67].

Partial substitution of Fe by Co increased the Curie temperature because the exchange constants of J_{Co-Co} and J_{Co-Fe} are larger than J_{Fe-Fe}, as can be inferred from the Bethe-Slater curve (Figure 2.7). The Curie temperature is directly related to the exchange energy (J_{ex}) according to the mean field model or Equation 2.4. An increase of J_{ex} leads to a linear increase of Curie temperature.

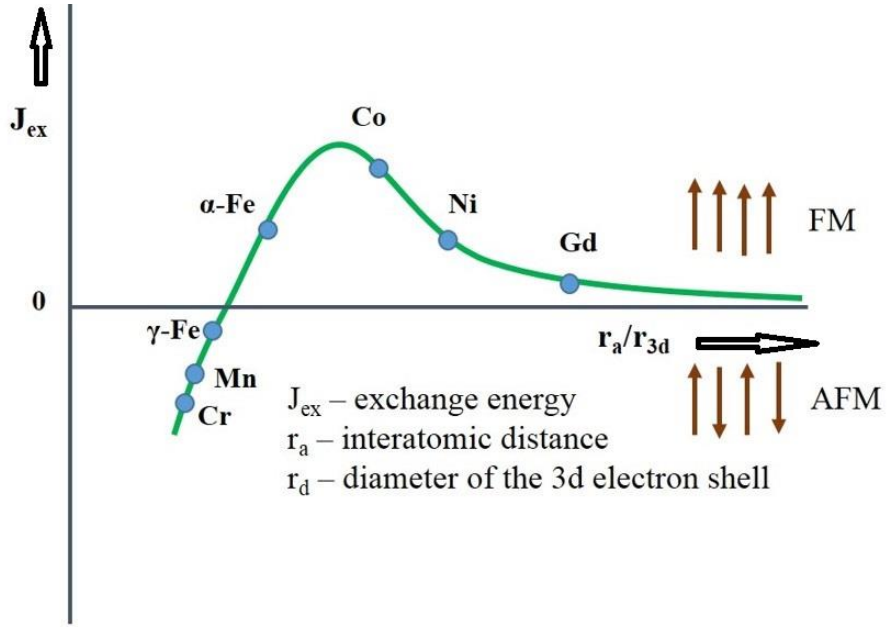

Figure 2.7. The Bethe-Slater curve, the relationship between the exchange interaction and r_a/r_{3d}.r_a represents the interatomic distance, r_{3d} represents the diameter of the 3d electron shell. The exchange energy between Co atoms is larger than that between Fe atoms.

Co substitution in $Nd_2Fe_{14}B$ has been accomplished via various processing methods. The difference in microstructure of Co substituted Nd-Fe-B magnets may lead to different effects. A systematic investigation of the magnetic properties in $Nd_{16}(Co_xFe_{77-x})_{14}B_7$ system is shown in Table 2.4, in which we can see that T_c increases monotonically with increasing cobalt content. However, coercivity, remanence and maximum energy product decrease slightly. Though Co substitution effects in single phase $Nd_2Fe_{14}B$ have been extensively studied, its effects in exchange coupled $Nd_2Fe_{14}B$/α-Fe were only investigated recently. Chang et al. [70] and Rong et al. [71] have investigated the effect of Co substitution for Fe in melt spun $Nd_2Fe_{14}B$/α-Fe and ball milled $Nd_2Fe_{14}B$/α-Fe respectively, and found that partial substitution of Co in the hard magnetic phase improves saturation magnetization, coercivity and energy product. Co addition in the hard phase may lead to inter-diffusion of the transition metals and also strengthen exchange coupling between the two phases [71].

These studies suggest that Co addition gives rise to substantially different effects in single phase $Nd_2Fe_{14}B$ and composite $Nd_2Fe_{14}B$/α-Fe. For rapidly quenched ribbons, it is usually assumed that the Fe: Co ratio is the same in both $Nd_2(Fe, Co)_{14}B$ and bcc-(Fe,Co) phases; similar observations are also reported for mechanically alloyed/milled powders [71, 72]. However, the influence of Co substitution should be carefully analyzed for Nd-Fe-B magnets processed by chemical methods.

Table 2.4. Magnetic performance and *Tc* of Co-alloyed Nd-Fe-B magnets.

Composition	B_r **(T)**	$_jH_c$ **(kA·m^{-1})**	$(BH)_{max}$ **(kT·m^{-3})**	T_c **(^{0}C)**	***Ref***
$Nd_{16}Fe_{77}B_7$	1.26	811.72	295.24	318	
$Nd_{16}Fe_{76.95}Co_{0.05}B_7$	1.23	987.84	280.12	374	
$Nd_{16}Fe_{76.9}Co_{0.1}B_7$	1.22	373.23	275.35	433	[31]
$Nd_{16}Fe_{76.8}Co_{0.2}B_7$	1.11	344.58	227.60	490	
$Nd_{16}Fe_{76.7}Co_{0.3}B_7$	1.08	289.67	215.66	553	
$Nd_{16}Fe_{79}B_6$ + 20 wt% Fe		397.9	108.2		
$Nd_{16}Fe_{69}Co_{10}B_6$ + 20 wt% Fe		477.48	135.3		
$Nd_{16}Fe_{64}Co_{15}B_6$ + 20 wt% Fe		557.06	167.1		
$Nd_{16}Fe_{59}Co_{20}B_6$ + 20 wt% Fe		540	165.5		[71]
$Nd_{16}Fe_{54}Co_{25}B_6$ + 20 wt% Fe		530	157.6		
$Nd_{16}Fe_{49}Co_{30}B_6$ + 20 wt% Fe		461.56	124.6		
$Nd_{16}Fe_{29}Co_{50}B_6$ + 20 wt% Fe		410	85.9		
$(Nd_{0.8}Dy_{0.2})_{13}(Fe_{0.95}Co_{0.05})_{81}B_6$	0.44	1530	38		
$(Nd_{0.8}Dy_{0.2})_{13}(Fe_{0.92}Co_{0.08})_{81}B_6$	0.48	1540	42		
$(Nd_{0.8}Dy_{0.2})_{13}(Fe_{0.90}Co_{0.1})_{81}B_6$	0.51	1560	43		[73]
$(Nd_{0.8}Dy_{0.2})_{13}(Fe_{0.87}Co_{0.13})_{81}B_6$	0.49	1590	42		
$(Nd_{0.8}Dy_{0.2})_{13}(Fe_{0.85}Co_{0.15})_{81}B_6$	0.46	1580	40		
$Nd_{9.5}Fe_{51.5}Co_{20}B_{15}Nb_4$	0.61	754	56.4		[74]
$Nd_9Fe_{51.5}Co_{20}B_{15.5}Nb_4$	0.80	784	94.3		
$Nd_{13.7}Fe_{73.5}Co_{6.7}Ga_{0.5}B_{5.6}$	0.85				

*Br: remanence induction at zero external field
*$_jH_c$: intrinsic coercivity, or the reverse field required to reduce induction back to zero
*$(BH)_{max}$: maximum energy product
*T_c: Curie temperature

The influence of other transition elements has also been studied. Sometimes co-substitution of Fe in Nd-Fe-B magnets is employed to obtain better magnetic properties. In $Nd_2(Fe_{1-x}T_x)_{14}B$ magnets, substituted elements and their content are 1.5Al, 0.2Cu, 1Si, 1Ni, 1V, 3Mn, 3Cr, 0.5Nb, 0.2Zr, 0.2Ti etc[15]. Pandian et.al. investigated the effect of individual Al, Cu, Ga and Nb additions on the microstructure and magnetic properties of sintered

NdFeB (Table 2.5). Each elemental substitution leads to improvement in coercivity but the extent of improvement differs from one element to the other. Al or Ga is known to cause enhancement in H_C due to its influence on a better distribution of the Nd-rich intergranular phase along the grain boundaries [75-77]. Minor additions of Cu or Nb can enhance coercivity due to the improved second quadrant characteristics. It is believed that inhibition of grain growth can be induced by Nb and nucleation enhancement can be induced by Cu [78]. Appropriate substitution of Si can improve coercivity, while substitution of Mn and Cr are not beneficial to the magnetic properties due to antiferromagnetic coupling between Fe and Mn or Cr. However, small amounts of these elements can be added for other properties such as corrosion resistance. The transition metal substitution of Fe in the $Nd_2Fe_{14}B$ phase alter its intrinsic properties. Addition of certain elements in the grain boundary or intergranular region helps to improve extrinsic magnetic properties via microstructural refinement. Cui et.al. recently studied the effect of intergranular addition of Ni in sintered Nd-Fe-B magnets and found that Ni atoms not only enter the matrix phase but also concentrate at the intergranular region. This results in improved coercivity and only a slight decrease in remanence and maximum energy product [79].

Table 2.5. Magnetic properties of $Nd_2(Fe_{1-x}T_x)_{14}B$ (T = transition metal) based magnets.

Composition	B_r (T)	H_c (kA·m^{-1})	M_S (emu/g)	T_c (^{0}C)	Ref
$Nd_{36}Fe_{62.8}B_{1.2}$	1.22	710		312	
$Nd_{16}Fe_{76.95}Co_{0.05}B_7$	1.07	820		297	
$Nd_{16}Fe_{76.9}Co_{0.1}B_7$	1.15	880		307	[80]
$Nd_{16}Fe_{76.8}Co_{0.2}B_7$	1.18	820		317	
$Nd_{16}Fe_{76.7}Co_{0.3}B_7$	1.20	1050		312	
$Nd_{10}Fe_{84}B_6$		406	123		
$Nd_9Fe_{84}B_6Nb_{0.5}Cu_{0.5}$		295	169		
$Nd_9Fe_{84}B_6Nb_1$		342	143		[78]
$Nd_9Fe_{84}B_6Nb_{0.5}Cu_{0.5}$		485	148		
$Nd_{12}Fe_{81}B_6Nb_1$		875	106		

Many other elements can substitute for Nd or Fe in $Nd_2Fe_{14}B$ while maintaining the tetragonal crystal structure. Figure 2.8 indicates the influence of elemental substitution on the Curie temperature (T_C), saturation magnetization (M_s) and anisotropy field (H_A).

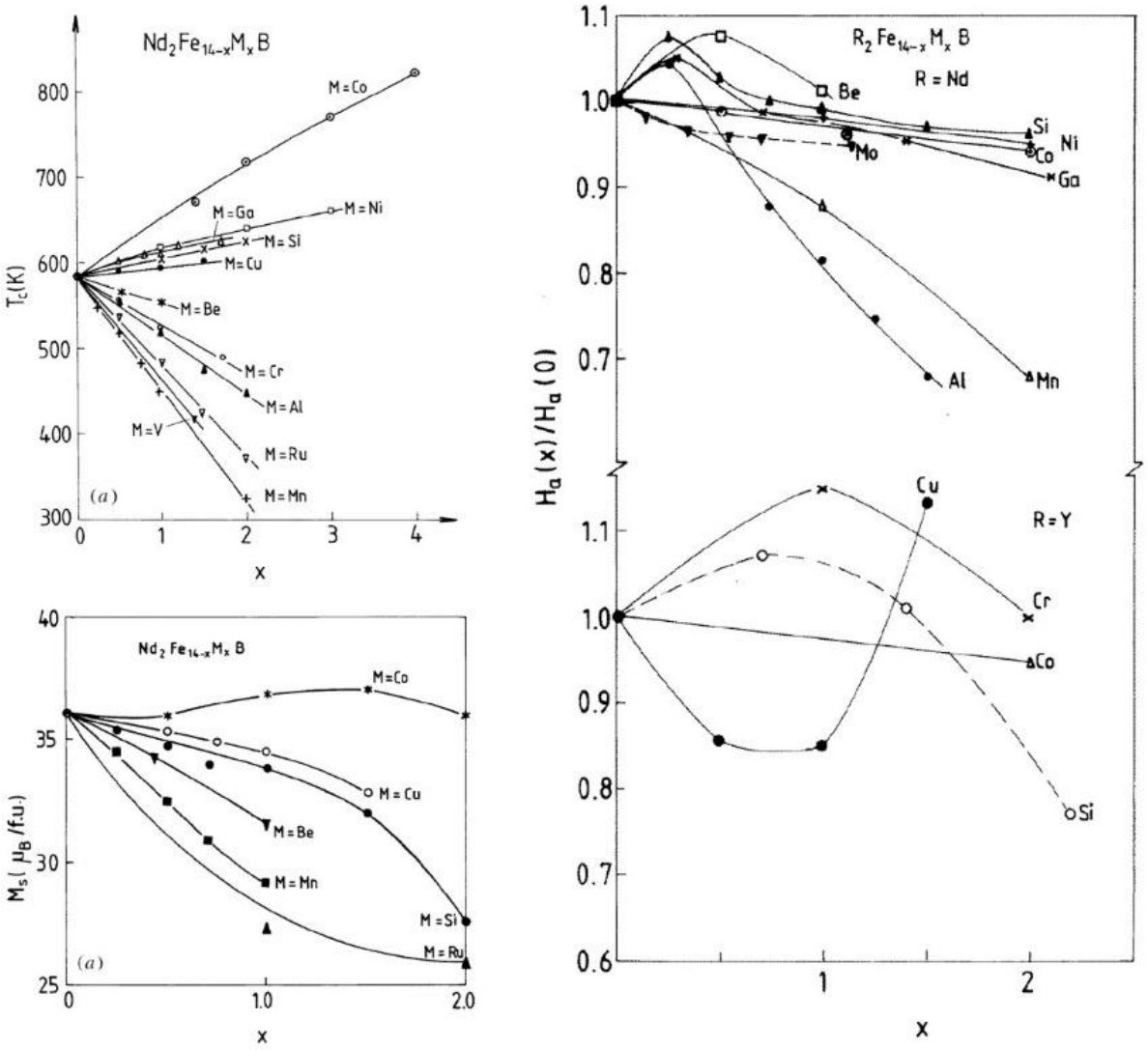

Figure 2.8. The influence of elemental substitution on Curie temperature (T_C), anisotropy field (H_A) and saturation magnetization (M_s) in $Nd_2Fe_{14}B$ [81].

2.3.3 Substitution of B

After the discovery of $Nd_2Fe_{14}B$, a search for other structures which can provide superior magnetic properties was conducted. Sagawa et al. systematically searched in $Nd_{15}Fe_{72}X_{13}$ for X = B, C, Mg, Al, Si, P, Ca, Ti, V, Cr, Mn, Ni, Cu, Zn, Ga, Ge, Zr, Nb, Mo, In, Sn, Sb, Hf, Ta, W, Pb and Bi and could not find a stable compound with higher Curie temperature and better magnetic properties than $Nd_2Fe_{14}B$. Although C can fully replace B in the $Nd_2Fe_{14}B$ structure and possesses a higher H_a, the saturation magnetization of $Nd_2Fe_{14}C$ is still less than that of $Nd_2Fe_{14}B$.

2.4 Synthesis of NdFeB nanostructures

A variety of methods have been employed to synthesize Nd-Fe-B, including both physical and chemical methods. Physical methods such as powder metallurgy, melt spinning and mechanical milling have been developed [82-86]. Sputtering [87] and pulsed laser deposition (PLD)[87] are also attractive methods to produced thin film Nd-Fe-B magnets for multi-layered structures or giant magnetoresistance (GMR) devices. However, the cost of physical methods are high as they need to start with elemental rare earth metals/powders. Chemical methods, on the other hand, can require only rare earth salts or oxides as precursors, greatly reducing the raw material cost in processing of Nd-Fe-B. Hence, chemical methods, such as thermal decomposition and reductive annealing [88], micro-wave reduction[89], sol-gel based method [90] and mechanochemical methods [91-93], are of great interest after the rare earth crisis. They can easily tune composition and control the particle or grain size of nanostructured Nd-Fe-B magnets. However, possible incorporation of intermediates, by-products and chemical impurities limits wider application of chemical synthesis, more investigations are needed before these methods can be widely applied in industry.

2.4.1 Mechanical milling

Mechanical milling is a solid-state powder processing technique, which involves continuous welding, fracturing, and re-welding of powder particles, resulting in the formation of ultrafine layered structures [94]. It has been employed to process a wide range of equilibrium and non-equilibrium alloy phases. The starting material can be either in the form of elemental powders or pre-alloyed ingots [95].

2.4.1.1 Process parameters

Various parameters affect the steady state condition and microstructure of as milled powder, such as type of mill, milling speed, milling time and ball-to-powder weight ratio (BPR). The possible effects of these parameters on the as milled powder are listed below.

2.4.1.1.1 Type of mill

Type of mill refers to the different designs of high-energy ball milling machines and also the material used for ball and vials.

There are various kinds of ball/vial materials including hardened steel, sintered corundum, tungsten carbide, zirconium oxide, etc. The choice of the appropriate material is important for ball milling. Usually the vial and balls should be made of the same material to avoid severe wear and contamination. In this study, tungsten carbide balls and vials were selected due to their high density and strength. It is the hardest material among the commercially available balls and vials, so less contamination and higher impact energy is expected from this kind of ball and vials.

High-energy ball milling design gives a range of ball milling capacity and efficiency, some designs can also provide a controlled milling environment (temperature control, magnetic field control, etc). A brief illustration of the different types of mills that are commercially available are shown below.

Planetary ball mills

An example of a laboratory planetary ball mills (referred to as Pulverisette) is manufactured by Fritsch GmbH in Germany. Ball milling speeds can be up to 1000 rpm. Two or four milling vials can be loaded into the milling machine on top of a rotating support disk (Figure 2.9). The vials rotate around their own axes in a direction opposite to the rotating support disk. The planet-like motion gives rise to the name of planetary ball mill.

During milling, the milled particles and milling balls experience a centrifugal force due to the rotation of the milling vials and the supporting disk. The force induced by milling leads

to friction and impact on the balls and milled powders. Friction is induced by the motion of the milling balls sliding down the inner wall of the milling vial. Impact is induced by the collisions between the balls and between the balls and the inner wall of the milling vial. The main advantages of planetary ball mills are their high milling capacity and high linear velocity of balls. The Pulverisette 7 high energy ball miller was used in this study.

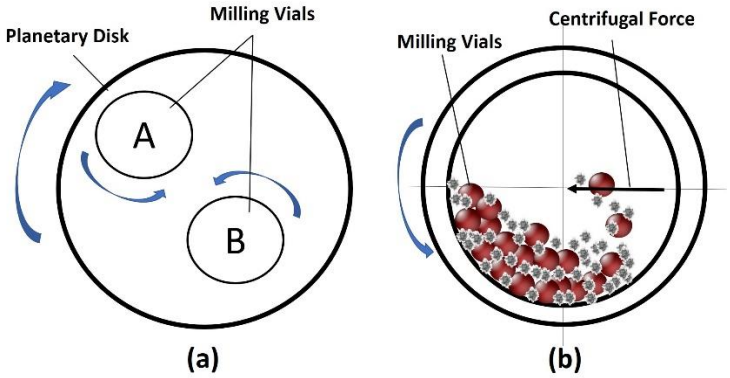

Figure 2.9. (a) Layout of planetary ball miller, (b) horizontal section of the milling vial.

Spex shaker mills

Another type of commonly used mill is the SPEX shaker mills. In this type of ball mill, the milling vial is clamped inside the machine and swung back and forth to follow a figure "8" at frequency of 10-50 Hz. During milling, the milling balls collide with the milled powder and the milling balls, creating a large impact force.

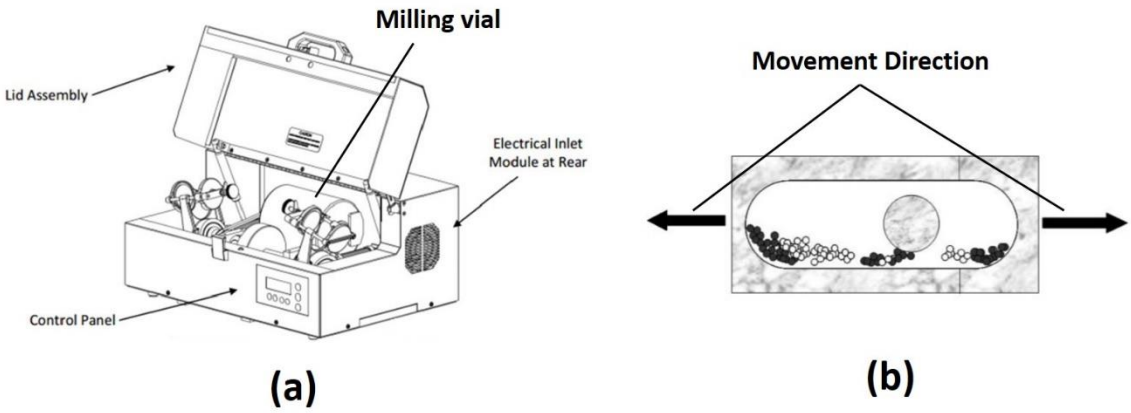

Figure 2.10. (a). Schematic of a Spex shaker mill, (b). vertical section of the milling vial [96].

2.4.1.1.2 Milling speed and time

Milling speed is an important parameter during ball milling since it directly reflects the amount of energy imparted to the powder particles. Usually the higher the milling speed, the larger the energy impact. However, this is not always true. For each design of ball mill, there is a critical value of milling speed. If the applied milling speed exceeds this value, balls can get stuck on the vial wall and no impact can be made onto the milled powders. High milling speed may lead to contamination. Hence, a suitable ball milling speed should be selected to prevent these situations.

Ball milling time is also a critical parameter. The milling time should be optimized with milling speed, ball to powder ratio and milling temperature to achieve the desired structure. Prolonged milling time should always be avoided to reduce contamination and formation of undesired phases. In this study, a milling time of 6 h was found to be sufficient for the desired phase formation.

2.4.1.1.3 Ball to powder weight ratio (BPR)

Like milling speed, BPR also determines the energy input to the milled powder. Usually the higher the BPR, the higher the rate of elemental mixing and alloying process, and shorter milling time will be needed. Frequently used BPR lies in the range between 10:1 and 20:1, a BPR of 14:1 was selected for this study.

2.4.1.1.4 Mechanical milling to synthesis Nd-Fe-B

Extensive studies have been made to synthesize Nd-Fe-B type permanent magnets using mechanical milling [97]. It was established as a third preparation route besides rapid quenching and sintering. Schultz et al [97, 98] first prepared magnetically isotropic $Nd_2Fe_{14}B$ powder via mechanical alloying and subsequent annealing at 700 °C. The resulting powder showed magnetic properties and a fine microstructure comparable to rapidly quenched samples. They also showed that milling of NdFeB alloy or alloying of

neodymium, iron and boron elemental powders led to the formation of nanocrystalline Fe precipitates in an amorphous matrix. Further heat treatment is needed to crystallize the as-milled powder into the tetragonal structure of $Nd_2Fe_{14}B$. During this process, the material goes through crystal – amorphous – crystal transformations. Figure 2.11 shows a typical X-ray diffraction pattern for as milled and annealed Nd-Fe-B powder [97].

After the concept of exchange coupling was proposed, Wecker et al [99] subjected Fe rich compositions of Nd-Fe-B system to mechanical alloying and successfully prepared exchange coupled $Nd_2Fe_{14}B/\alpha$-Fe nanocomposites with enhanced remanence. They studied a range of compositions, from Nd rich to Fe rich, and used hot compaction to synthesize $Nd_2Fe_{14}B/\alpha$-Fe nanocomposites, with an average grain size of ~30 nm.

Miao et al [100] studied the magnetic properties and the structure of mechanically alloyed and mechanically milled Fe rich Nd-Fe-B system. Both methods led to the formation of $Nd_2Fe_{14}B/\alpha$-Fe nanocomposites, but the mechanically milled samples had a more uniform and finer grain structure and exhibited higher remanence and coercivity after annealing. They also performed Mossbauer spectroscopy and found that mechanical milling led to decomposition of Nd-Fe-B alloys into a Nd-rich amorphous phase and α-Fe nanocrystals. The volume fraction of the amorphous phase decreased with increasing iron content, regardless of the initial composition.

Doping of various alloying elements at the Re and TM sites using the mechanical milling method have been investigated. Dy substitution of Nd was studied by Jurczyk et al [101, 102] in mechanically milled Nd-Fe-B alloys. It was shown that increasing Dy content led to an increase of the coercive field. Yan et al [103] investigated the influence of combined doping of Ti and Al or Cu, and showed that an appropriate amount of Ti should be selected to improve the coercivity of Nd-Fe-B magnets. Small amount of Pb doped in the TM site increased the coercivity [104]. The corrosion behavior of $Nd_2(Fe, Co,Al,Cr)_{14}B/\alpha$-Fe was studied by Jakubowicz et al [105], who found good corrosion resistance as well as high temperature stability.

Table 2.6 summarizes the magnetic properties of Nd-Fe-B type permanent magnets synthesized by the mechanical milling/alloying method.

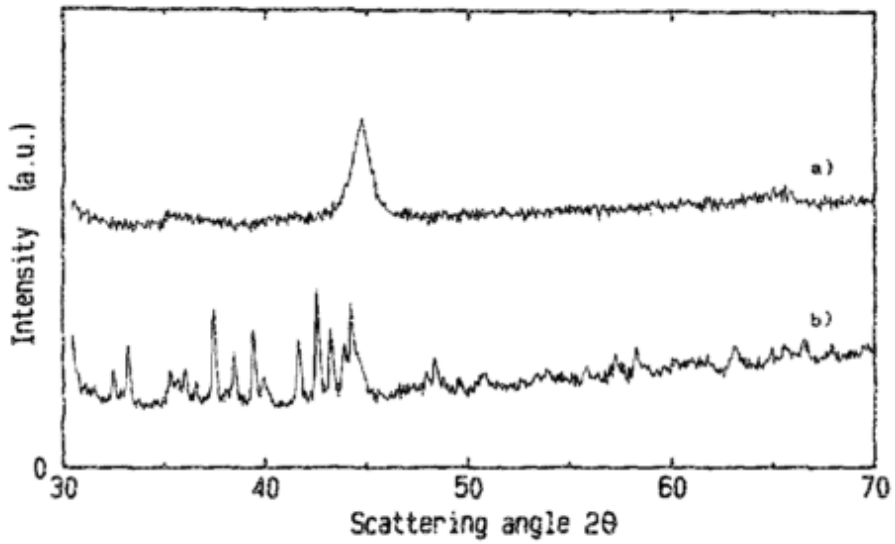

Figure 2.11. Typical X-ray diffraction pattern of (a) as milled Nd-Fe-B powder and (b) heat treated Nd-Fe-B powder, an amorphous phase is induced by mechanical milling which crystallizes into the $Nd_2Fe_{14}B$ tetragonal structure during heat treatment [106].

Table 2.6. Summary of magnetic properties of Nd-Fe-B type magnets prepared by mechanical milling.

Composition	**Particle Size /grain size**	**Magnetic Properties**			**Ref.**
		Br (T)	*Hc* (Oe)	$(BH)_{max}$ (MGOe)	
$Nd_{15}Fe_{77}B_8$	-	0.8	12750	12.8	[97]
$Nd_{16}Fe_{76}B_8$	~50nm (grain size)		15300		[98]
$Nd_{12}Fe_{82}B_6$	25-35nm (grain size	0.73	7665	13.9	[106]
$Nd_{10}Fe_{(84-x)}Pb_xB_6$ Best property at x=0.5	40-80nm (grain size)	0.87	3769	-	[104]
$Nd_2Fe_{14}B$ $Nd_2Fe_{12}Co_2B$ $Nd_2Fe_{11.49}Co_2Al_{0.17}Cr_{0.34}B$ $Nd_2Fe_{11.49}Co_2Al_{0.17}Cr_{0.34}B$/Fe (10vol% Fe) $Nd_2Fe_{11.49}Co_2Al_{0.17}Cr_{0.34}B$/Fe (37.5vol% Fe)	~90nm (grain size)	0.66 0.54 0.61 0.88 1.02	11000 5000 11600 10100 8600	-	[105]
$Nd_{15}Fe_{79-x}Co_xB_6$/ 20wt%Fe x=0 x=10 x=15 x=20 x=30 x=50	-		 5300 6200 8300 7000 5800 5000	 13 15 21 20 15 11.8	[70]
$Nd_7Fe_{82.5}Co_{6.5}Zr_{0.5}B_{3.5}$ $Nd_8Fe_{78}Co_9Si_1B_4$ $Nd_9Fe_{77}Co_{8.5}Si_1B_{4.5}$	-	1.21 1.19 1.11	4200 5000 6000	16.2 18.7 18.5	[71]

2.4.2 Chemical processing

Since the rare earth crisis, Coey's prediction of giant energy product for anisotropic $Sm_2Fe_{17}N_3/Fe_{67}Co_{33}$ nanocomposite magnets [108] and the high value of coercivity and $(BH)_{max}$ reported in nano-composite thin films [109] has created more interest in the chemical synthesis of Nd-Fe-B based materials. The chemical methods use much cheaper precursors and provide better microstructural control than physical methods. Table 2.7 summarizes the magnetic properties of chemically synthesized Nd-Fe-B based magnets. Among all the methods, the microwave-assisted auto combustion method, thermal decomposition and reduction annealing, spray dry and reduction diffusion process, as well as the mechanochemical method produce nanoparticles with superior magnetic properties. The mechanochemical method stands out as it utilizes the cheap metal oxides as the raw material. Besides, the milling occurred in an enclosed milling vial, which provides well-defined parameters for process optimization. In addition, this process is scalable for industrial applications. Hence it can be considered as a most promising chemical method for Nd-Fe-B based magnetic nanoparticle synthesis.

Table 2.7. Structure and magnetic properties of Nd-Fe-B based magnetic materials synthesized by chemical methods.

Synthesis method	Phases	As-synthesised properties		After by-product removal properties		Size (nm)	Ref.
		Hc (kOe)	Ms (emu/g)	Hc (kOe)	Ms (emu/g)		
Sol-gel		6.1	20.7	3.9	102.3	~65	[90]
Microwave		8.0	40	4.00	90	20-80	[109]
Microwave	$Nd_2(Fe,Co)_{14}B$	-	-	4-8	106-75	25-75	[89]
Microwave	$Nd_2Fe_{14}B/\alpha$-Fe	11.8	37	9	123	~62	[110]
Mechanochemical [1]	$Nd_2Fe_{14}B$	-	-	6.25	-	~50	[111]
One-pot synthesis[2]	$Nd_2Fe_{14}B$	-	-	0.5	11	~25	[112]
	$Nd_2Fe_{14}B/\alpha$-Fe	-	-	0.27	20	~25	
One-pot synthesis[2]	Nd-Fe-B	-	-	0.05	131	150-200	[113]
Sol-gel[3]	$Nd_2Fe_{14}B/\alpha$-Fe			0.13	89	50-70	[114]
	$Nd_2Fe_{14}B/Nd_2Fe_{17}/\alpha$-Fe	-	-	3.32	127.7	35	[115]
Reduction-diffusion	$Nd_2Fe_{14}B$	0.7	112	-	-	~80	[116]
Thermal decomposition and reductive annealing	$Nd_2Fe_{14}B/Fe_3B$	11	72	-	-	-	[88]
Spray dry & reduction diffusion[4]	$Nd_2Fe_{14}B$	10.6	25	5.1	125	<50	[117]
Mechanochemical [5]	$Nd_2(Fe,Co)_{14}B$	-	-	9.6	68	~70	[118]
	$Nd_2(Fe,Co)_{14}B$	12.4	20	8.8	100	~45	[14]
	$Nd_2Fe_{14}B$	10.3	50	3.3	150	~100	[91]
	$Nd_2Fe_{14}B$	14.7	~15	4.6	150	60-140	[92]
	$(Nd_{0.75}Dy_{0.25})_2Fe_{14}B$	18.9	~12	6.2	125		
	$Nd_2Fe_{14}B$	12	~75	-	-	50-70	[93]

[1]: hydrogen disproportionation induced by reactive milling
[2]: Glycine autocombustion of precursor metal nitrates to metal oxides, followed by H_2 reduction.
[3]: Pechini-type sol-gel method which converts precursor metal chlorides into metal oxides mixture, followed by CaH_2 reduction.
[4]: Spray drying of precursor metal chlorides to mixed metal oxides, followed by annealing in H_2 and additional reduction with Ca and CaO (as dispersant).
[5]: Mechanical milling of precursor metal oxides with Ca as reducing agent, followed by annealing.

2.4.2.1 Mechanochemical processing

In mechanochemical processing (MCP), chemical reactions are generated by mechanical energy [120]. The fact that mechanical action can initiate chemical reactions was first reported by Lea in the 19th century when he found that fine grinding in a mortar can decompose metal halides into halogen and metal [121]. The application of mechanical forces to chemical systems, whether by mechanical milling or ultrasound led to exciting developments, especially in synthesizing intermetallic compounds [122]. During the mechanochemical process in a high energy ball miller, either a reduction or metathesis reaction usually takes place. These chemical reactions can be steady-state or in a self-propagating combustive manner. The combustive reaction usually generates micron-sized particles, it is difficult to control the particle size due to the necessity of high temperatures. The steady state reaction usually results in nano-sized product. In most cases, mechanochemical combustion is deliberately avoided to control the particle size, either by selecting a suitable milling parameter to reduce milling energy, or by adding inert diluents to the reactants to reduce reaction rate. In some cases when heat treatment of the as milled powder is necessary, the inert diluent can also serve as the solid matrix to avoid particle agglomeration [120, 123, 124].

By selecting suitable parameters, such as reaction path, milling conditions, starting material stoichiometry, diluent, the mechanochemical process can form the desired phase with particles as small as 10-20 nm [125]. Common reducing agents include Ca, Na, Mg, graphite, etc, and their respective diluents include $CaCl_2$, NaCl, MgCl, CaO, MgO, etc. Many products have been synthesized using the mechanochemical process, ranging from

metal hydrides, oxides, organics, metal-organic frameworks to intermetallic compounds. Examples of some mechanochemical process that have been studied are listed in Table 2.8.

Table 2.8. Examples of reactions in the mechanochemical process.

	Reactions	Ref.
1.	$NiCl_2$+2 Na → Ni + 2 NaCl $CuCl_2$+2 Na → Cu + 2 NaCl $FeCl_3$+3 Na → Fe + 3 NaCl $CoCl_2$+2 Na → Co + 2 NaCl	[120]
2.	$2AlCl_3 + CaO \rightarrow Al_2O_3 + 3CaCl_2$	[126]
3.	$GdCl_3 + 3NaOH \rightarrow Gd_2O_3 + 3NaCl + 1.5H_2O$	[127]
4.	$Na_2Cr_2O_7 + S \rightarrow Cr_2O_3 + Na_2SO_4$	[128]
5.	$SnCl_2 + Na_2CO_3 + O_2 \rightarrow SnO_2 + 2NaCl + CO_2$	[129]
6.	$ZnCl_2 + Na_2CO_3 \rightarrow ZnO + 2NaCl + CO_2$	[130]
7.	Sm_2O_3+CoO + Ca → Sm_2Co_{17} + CaO	[131]
8.	La_2O_3 + 10Co + 3Ca → $2LaCo_5$ + 3CaO	[132]
9.	Y_2O_3 + 10Co + 3Ca → $2YCo_5$ + 3CaO PrO_2 + 5Co + 2Ca → $PrCo_5$ + 2CaO Sm_2O_3+ 10Co + 3Ca → $2SmCo_5$ +3 CaO	[132]
10.	Nd_2O_3+ 13Fe + FeB + 3Ca → $Nd_2Fe_{14}B$ +3 CaO	[93]
11.	Nd_2O_3+ Fe_2O_3 + B2O3 + 3Ca → $Nd_2Fe_{14}B$ +3 CaO	[91, 92]

Recently, $Nd_2Fe_{14}B$ alloy nanoparticles have been synthesized by various processing methods, for example, the surfactant-assisted ball milling [133, 134] and many chemical synthesis [90, 110, 135, 136], only the group of Hadjipanayis has synthesized $Nd_2Fe_{14}B$ through the mechano-chemical process (MCP) (Table 2.8) [91-93]. The high energy induced by ball milling initiates the reduction reaction of neodymium oxide or other oxides, as shown in the equation below:

$Nd_2O_3 + 13Fe + FeB + 3Ca \rightarrow Nd_2Fe_{14}B + 3CaO$, or

$Nd_2O_3 + Fe_2O_3 + B_2O_3 + 3Ca \rightarrow Nd_2Fe_{14}B + 3CaO$

They have achieved high coercivity of up to 14 kOe before separating $Nd_2Fe_{14}B$ and Nd-rich nanoparticles from the byproduct (CaO). However, after by-product removal, the

coercivity drops drastically to only ~ 4 kOe. Besides, no systematic study has been performed to study the mechanism of milling and to evaluate the influence of process parameters on the properties of synthesized particles. One focus of this work is to remove the by-product with minimal degradation of magnetic properties. In other mechanochemically synthesized material, it was found that ball milling speed, reductant/oxide ratio, reactants/diluent ratio and volume percentage of reductant in the milling vial can affect the microstructure and properties of the synthesized particles [137, 138]. The effects of these parameters still need to be systematically investigated in this Nd-Fe-B system for a deep understanding of mechanochemical milling.

2.5 Questions unaddressed in nanostructured Nd-Fe-B magnets processing and innovative aspects of the current work:

It is shown from the literature review that Nd-Fe-B type magnetic materials are the highest performance magnets. The recent discovery of high energy product nanocomposite magnets stimulated interest in nanosized or nanostructured Nd-Fe-B magnets. There are very few investigations of the mechanochemical synthesis of Nd-Fe-B magnets. The earlier studies focused on the successful synthesis of the high coercivity $Nd_2Fe_{14}B$ phase, but the effect of process parameters and reaction mechanism remained unclear, although they are of vital importance to optimize process.

Hence, in this study, we focused on investigating the effect of process parameters on the structure and properties of mechanochemically synthesized Nd-Fe-B based nanoparticles. We investigated the influence of diluent (CaO) on the structure and magnetic properties of the nanoparticles, as well as the influence of diluent on the formation mechanism. Thus we can optimize the diluent content.

We also focused on the kinetics of the mechanochemical milling process. Such studies have not yet been performed by other researchers, we proposed a numerical model which calculates milling efficiency at different ball milling speeds. It helps to identify the milling speed for highest energy utilization efficiency, which is of significant interest.

The literature also revealed that alloying can improve magnetic properties. However, only Gabay et al. [92] synthesized $(Nd_{0.75}Dy_{0.25})_2Fe_{14}B$ nanoparticles to investigate the influence of Dy on the mechanochemically processed Nd-Fe-B nanoparticles. We systematically investigated the influence of Dy substitution on the magnetic and structural properties of mechanochemically synthesized $Nd_2(Fe,Co)_{14}B$ nanoparticles. This study revealed the ease of alloying via the mechanochemical method. The coercivity reversal mechanism of these nanoparticles was also studied.

References

[1] P. Langevin. *Ann. chim. phys*. 1905, 5, 70-127.

[2] M. E. McHenry, M. A. Willard, and D. E. Laughlin. *Progress in Materials Science*. 1999, 44, 291-433.

[3] R. Cardias *et al. Scientific Reports*. 2017, 7, 14878.

[4] M. Leonowicz, "Modern hard magnetic materials," PhD, Warsaw University of Technology, Poland, 1996.

[5] P. Ripka, *Magnetic Sensors and Magnetometers*. Boston: Artech House, 2001.

[6] J. Coey. *Journal of Magnetism and Magnetic Materials*. 1995, 140, 1041-1044.

[7] B. Slusarek and K. Zakrzewski. *Przeglad Elektrotechniczny*. 2012, 88, 123-126.

[8] J. Liu and M. Walmer. *IEEE Transactions on Electron Devices*. 2005, 52, 899-902.

[9] T. Sebastian. *IEEE Transactions on Industry Applications*. 1995, 31, 353-357.

[10] B. Ma, J. Herchenroeder, B. Smith, M. Suda, D. Brown, and Z. Chen. *Journal of Magnetism and Magnetic materials*. 2002, 239, 418-423.

[11] G. Bai, R. Gao, Y. Sun, G. Han, and B. Wang. *Journal of Magnetism and Magnetic Materials*. 2007, 308, 20-23.

[12] C. Fuerst and E. Brewer. *Journal of Applied Physics*. 1993, 73, 5751-5756.

[13] J. A. Ewing. *Proceedings of the Royal Society of London*. 1885, 38, 58-62.

[14] Y. Zhong, V. Chaudhary, X. Tan, H. Parmar, and R. Ramanujan. *Nanoscale*. 2017, 9, 18651-18660.

[15] S. Pan, *Rare Earth Permanent-Magnet Alloys High Temperature Phase Transformation*. Springer, 2013.

[16] J. Herbst. *Reviews of Modern Physics*. 1991, 63, 819-898.

[17] M. R. D. Givord, D. Taylor. *Journal de Physique IV Colloque*. 1992, 02, 95-104.

[18] X. H. Tan, S. F. Chan, K. Han, and H. Xu. *Scientific Reports*. 2014, 4, 6805.

[19] A. Fukuno, K. Hirose, and T. Yoneyama. *Journal of Applied Physics*. 1990, 67, 4750-4752.

[20] S. Hirosawa. *IEEE Transactions on Magnetics*. 1989, 25, 3437-3439.

[21] A. Lisfi, S. Pokharel, O. Akioya, N. Alqhtany, and M. Wuttig. *AIP Advances*. 2017, 7, 056206.

[22] H. Li, Y. Liang, X. Tan, H. Xu, P. Hu, and K. Ren. *Materials*. 2017, 10, 1-10.

[23] M. Xu, M. Yue, Q. Wu, Y. Li, and Q. Lu. *AIP Advances*. 2016, 6, 056020.

[24] R. Skomski and J. Coey, *Permanent Magnetism*. Bristol, UK; Philadelphia, PA: Institute of Physics Pub., 1999.

[25] G. Martinek and H. Kronmüller. *Journal of Magnetism and Magnetic Materials*. 1990, 86, 177-183.

[26] W. F. Brown Jr. *Reviews of Modern Physics*. 1945, 17, 15-19.

[27] P. Kharel *et al. Journal of Physics D: Applied Physics*. 2013, 46, 095003.

[28] P. Gaunt. *Philosophical Magazine B*. 1983, 48, 261-276.

[29] N. Poudyal and J. P. Liu. *Journal of Physics D: Applied Physics*. 2012, 46, 043001.

[30] C. B. Rong *et al. Journal of Physics D: Applied Physics*. 2013, 46, 045001.

[31] M. Sagawa, S. Fujimura, H. Yamamoto, Y. Matsuura, and K. Hiraga. *IEEE Transactions on Magnetics*. 1984, 20, 1584-1589.

[32] J. J. Croat, J. F. Herbst, R. W. Lee, and F. E. Pinkerton. *Journal of Applied Physics*. 1984, 55, 2078-2082.

[33] T. Saito, T. Deguchi, and H. Yamamoto. *AIP Advances*. 2017, 7, 056204.

[34] D. V. Dudina and A. K. Mukherjee. *Journal of Nanomaterials*. 2013, 2013, 5-17.

[35] H. Zeng, J. Li, J. P. Liu, Z. L. Wang, and S. Sun. *Nature*. 2002, 420, 395.

[36] O. Gutfleisch, M. A. Willard, E. Brück, C. H. Chen, S. Sankar, and J. P. Liu. *Advanced Materials*. 2011, 23, 821-842.

[37] J. Pyrhönen *et al. IEEE Transactions on Industrial Electronics*. 2015, 62, 857-865.

[38] S. Hamidizadeh, N. Alatawneh, R. R. Chromik, and D. A. Lowther. *IEEE Transactions on Magnetics*. 2016, 52, 1-4.

[39] D. Brown, B.-M. Ma, and Z. Chen. *Journal of Magnetism and Magnetic Materials*. 2002, 248, 432-440.

[40] J. F. Herbst, J. J. Croat, F. E. Pinkerton, and W. Yelon. *Physical Review B*. 1984, 29, 4176-4178.

[41] J. Herbst. *Reviews of Modern Physics*. 1991, 63, 819.

[42] D. Givord, H. Li, and J. Moreau. *Solid State Communications*. 1984, 50, 497-499.

[43] D. Haskel *et al. Physical Review Letters*. 2005, 95, 217207.

[44] M. Ito *et al. AIP Advances*. 2016, 6, 056029.

[45] J. Jin, T. Ma, Y. Zhang, G. Bai, and M. Yan. *Scientific Reports*. 2016, 6, 32200.

[46] A. K. Pathak *et al*. *Advanced Materials*. 2015, 27, 2663-2667.

[47] H. Rahimi, A. Ghasemi, R. Mozaffarinia, and M. Tavoosi. *Journal of Magnetism and Magnetic Materials*. 2017, 424, 199-206.

[48] H. Rahimi, A. Ghasemi, R. Mozaffarinia, and M. Tavoosi. *Journal of Magnetism and Magnetic Materials*. 2017, 429, 182-191.

[49] H. Ucar, D. S. Parker, I. Nlebedim, R. McCallum, S. McCall, and M. Parans Paranthaman. *Advances in Materials Research*. 2015, 4, 227-233.

[50] X. Liu and Z. Altounian. *Journal of Applied Physics*. 2012, 111, 07A701.

[51] W. Li, H. Sepehri-Amin, T. Ohkubo, N. Hase, and K. Hono. *Acta Materialia*. 2011, 59, 3061-3069.

[52] L. Yu, J. Zhang, S. Hu, Z. Han, and M. Yan. *Journal of Magnetism and Magnetic Materials*. 2008, 320, 1427-1430.

[53] L. Yu, Y. Wen, and M. Yan. *Journal of Magnetism and Magnetic Materials*. 2004, 283, 353-356.

[54] M. Sagawa and N. Fujimoto, "NdFeB sintered magnet and method for producing the same," ed, 2013, p. US8562756 B2.

[55] N. Oono, M. Sagawa, R. Kasada, H. Matsui, and A. Kimura. *Journal of Magnetism and Magnetic Materials*. 2011, 323, 297-300.

[56] K. Lu, X. Bao, M. Tang, L. Sun, J. Li, and X. Gao. *Journal of Magnetism and Magnetic Materials*. 2017, 441, 517-522.

[57] L. Liang, T. Ma, P. Zhang, J. Jin, and M. Yan. *Journal of Magnetism and Magnetic Materials*. 2014, 355, 131-135.

[58] F. Xu, L. Zhang, X. Dong, Q. Liu, and M. Komuro. *Scripta Materialia*. 2011, 64, 1137-1140.

[59] F. Xu, J. Wang, X. Dong, L. Zhang, and J. Wu. *Journal of Alloys and Compounds*. 2011, 509, 7909-7914.

[60] S. Sawatzki, I. Dirba, L. Schultz, and O. Gutfleisch. *Journal of Applied Physics*. 2013, 114, 133902.

[61] S. Sawatzki, A. Dirks, B. Frincu, K. Löwe, and O. Gutfleisch. *Journal of Applied Physics*. 2014, 115, 17A705.

[62] H. Sepehri-Amin, T. Ohkubo, and K. Hono. *Acta Materialia*. 2013, 61, 1982-1990.

[63] T. Ohkubo, T. Abe, S. Hirosawa, and K. Hono. *Journal of Alloys and Compounds*. 2014, 617, 884-892.

[64] T. Ma *et al. Materials Express*. 2016, 6, 93-99.

[65] A. Melsheimer, M. Seeger, and H. Kronmüller. *Journal of Magnetism and Magnetic Materials*. 1999, 202, 458-464.

[66] C. Fuerst, J. Herbst, and E. Alson. *Journal of Magnetism and Magnetic Materials*. 1986, 54, 567-569.

[67] Y. Matsuura, S. Hirosawa, H. Yamamoto, S. Fujimura, and M. Sagawa. *Applied Physics Letters*. 1985, 46, 308-310.

[68] M. C. Cadeville and A. Meyer. *Comptes Rendus Hebdomadaires des Seances de L Academie des Sciences*. 1962, 255, 3391-3400.

[69] N. Lundquist and H. P. Myers. *Arkiv for Fysik*. 1961, 21, 463-471.

[70] W. C. Chang, S. H. Wu, B. M. Ma, C. O. Bounds, and S. Y. Yao. *Journal of Applied Physics*. 1998, 83, 2147-2151.

[71] C. B. Rong *et al. Journal of Physics D: Applied Physics*. 2013, 46, 045001.

[72] V. Neu and L. Schultz. *Journal of Applied Physics*. 2001, 90, 1540-1544.

[73] W. Chen *et al. Journal of Magnetism and Magnetic Materials*. 2003, 261, 222-227.

[74] X. Cui, Z. Liu, X. Zhong, H. Yu, and D. Zeng. *Journal of Applied Physics*. 2012, 111, 07B508.

[75] K. Knoch, E.-T. Henig, and J. Fidler. *Journal of Magnetism and Magnetic Materials*. 1990, 83, 209-210.

[76] X. Kou, X. Sun, Y. Chuang, T. Zhao, R. Grössinger, and H. Kirchmayr. *Journal of Magnetism and Magnetic Materials*. 1989, 82, 327-334.

[77] K. Knoch, B. Grieb, E.-T. Henig, H. Kronmuller, and G. Petzow. *IEEE Transactions on Magnetics*. 1990, 26, 1951-1953.

[78] D. Salazar, A. Martín-Cid, R. Madugundo, J. Garitaonandia, J. Barandiaran, and G. Hadjipanayis. *Journal of Physics D: Applied Physics*. 2016, 50, 015305.

[79] X. Cui *et al. Journal of Alloys and Compounds*. 2017, 726, 846-851.

[80] S. Pandian, V. Chandrasekaran, G. Markandeyulu, K. Iyer, and K. Rama Rao. *Journal of Applied Physics*. 2002, 92, 6082-6086.

[81] E. Burzo. *Reports on Progress in Physics*. 1998, 61, 1099-1266.

[82] F. Vial, F. Joly, E. Nevalainen, M. Sagawa, K. Hiraga, and K. Park. *Journal of Magnetism and Magnetic Materials*. 2002, 242, 1329-1334.

[83] S. Öztürk, K. Icin, B. Öztürk, U. Topal, and H. K. Odabaşi. *International Journal of Materials Science and Applications*. 2017, 6, 241.

[84] M. Hussain, L. Zhao, C. Zhang, D. Jiao, X. Zhong, and Z. Liu. *Physica B: Condensed Matter*. 2016, 483, 69-74.

[85] S. Shukla, D. T. Wu, H. Ramanarayan, D. Srolovitz, and R. V. Ramanujan. *Acta Materialia*. 2013, 61, 3242-3248.

[86] S. Shukla, A. Banas, and R. V. Ramanujan. *Intermetallics*. 2011, 19, 1265-1273.

[87] R. Fujiwara *et al. Sensors and Actuators A: Physical*. 2016, 251, 219-224.

[88] L. Yu, Y. Zhang, Z. Yang, J. He, K. Dong, and Y. Hou. *Nanoscale*. 2016, 8, 12879-12882.

[89] X. Tan, H. Parmar, Y. Zhong, V. Chaudhary, and R. V. Ramanujan. *IEEE Magnetics Letters*. 2017, 1-5.

[90] P. K. Deheri, V. Swaminathan, S. D. Bhame, Z. Liu, and R. V. Ramanujan. *Chemistry of Materials*. 2010, 22, 6509-6517.

[91] O. Koylu-Alkan, J. Barandiaran, D. Salazar, and G. Hadjipanayis. *AIP Advances*. 2016, 6, 056027.

[92] A. M. Gabay, X. C. Hu, and G. C. Hadjipanayis. *Journal of Alloys and Compounds*. 2013, 574, 472-476.

[93] A. Pal, A. Gabay, and G. C. Hadjipanayis. *Journal of Alloys and Compounds*. 2012, 543, 31-33.

[94] C. C. Koch and J. Whittenberger. *Intermetallics*. 1996, 4, 339-355.

[95] D. Zhang. *Progress in Materials Science*. 2004, 49, 537-560.

[96] A. L. Garay, A. Pichon, and S. L. James. *Chemical Society Reviews*. 2007, 36, 846-855.

[97] L. Schultz, J. Wecker, and E. Hellstern. *Journal of Applied Physics*. 1987, 61, 3583-3585.

[98] L. Schultz, K. Schnitzke, and J. Wecker. *Journal of Applied Pysics*. 1988, 64, 5302-5304.

[99] J. Wecker, K. Schnitzke, H. Cerva, and W. Grogger. *Applied Physics Letters*. 1995, 67, 563-565.

[100] W. Miao, J. Ding, P. McCormick, and R. Street. *Journal of Applied Physics*. 1996, 79, 2079-2083.

[101] V. Villas-Boas, J. M. González, F. Cebollada, M. F. Rossignol, D. W. Taylor, and D. Givord. *Journal of Magnetism and Magnetic Materials*. 1998, 185, 180-186.

[102] M. X. P. N.J.Yu, P.Y.Zhang, and H.L.Ge. *Journal of Magnetics*. 2013, 18, 235-239.

[103] A. Yan, X. Song, Z. Chen, and X. Wang. *Journal of Magnetism and Magnetic Materials*. 1998, 185, 369-374.

[104] W. Kaszuwara and M. Leonowicz. *Journal of Magnetism and Magnetic Materials*. 2002, 242, 1366-1368.

[105] J. Jakubowicz and M. Giersig. *Journal of Alloys and Compounds*. 2003, 349, 311-315.

[106] S. Pan, *Rare Earth Permanent-Magnet Alloys' High Temperature Phase Transformation*. Springer, 2013.

[107] S. Gang, H. Lianxi, and W. Erde. *Journal of Magnetism and Magnetic Materials*. 2006, 301, 319-324.

[108] R. Skomski and J. Coey. *Physical Review B*. 1993, 48, 15812-15816.

[109] W. B. Cui, Y. K. Takahashi, and K. Hono. *Advanced Materials*. 2012, 24, 6530-6535.

[110] V. Swaminathan, P. K. Deheri, S. D. Bhame, and R. V. Ramanujan. *Nanoscale*. 2013, 5, 2718-2725.

[111] H. Parmar, T. Xiao, V. Chaudhary, Y. Zhong, and R. V. Ramanujan. *Nanoscale*. 2017, 9, 13956-13966.

[112] A. Bollero, O. Gutfleisch, M. Kubis, K.-H. Müller, and L. Schultz. *Acta Materialia*. 2000, 48, 4929-4934.

[113] A. P. Jadhav, A. Hussain, J. H. Lee, Y. K. Baek, C. J. Choi, and Y. S. Kang. *New Journal of Chemistry*. 2012, 36, 2405-2411.

[114] A. P. Jadhav, H. Ma, D. S. Kim, Y. K. Baek, C. J. Choi, and Y. S. Kang. *Bulletin of the Korean Chemical Society*. 2014, 35, 886-890.

[115] A. Hussain, A. P. Jadhav, Y. K. Baek, H. J. Choi, J. Lee, and Y. S. Kang. *Journal of Nanoscience and Nanotechnology*. 2013, 13, 7717-7722.

[116] H. Rahimi, A. Ghasemi, R. Mozaffarinia, and M. Tavoosi. *Journal of Magnetism and Magnetic Materials*. 2017, 444, 111-118.

[117] C. Km, Y. Km, H. Cha, and Y. Kang. *Physica Scripta*. 2007, 2007, 321-325.

[118] Y. Wang *et al. Journal of Magnetism and Magnetic Materials*. 2017, 439, 91-94.

[119] Y. Zhong, V. Chaudhary, X. Tan, H. Parmar, and R. Ramanujan. *Journal of Alloys and Compounds*. 2018, 747, 755-763.

[120] T. Tsuzuki and P. G. McCormick. *Journal of Materials Science*. 2004, 39, 5143-5146.

[121] M. C. Lea. *American Journal of Science*. 1893, 241-244.

[122] S. L. James and T. Friščić. *Chemical Society Reviews*. 2013, 42, 7494-7496.

[123] P. G. McCormick, T. Tsuzuki, J. S. Robinson, and J. Ding. *Advanced Materials*. 2001, 13, 1008-1010.

[124] F. G. Tatiana, P. B. Antonina, and Z. L. Nikolai. *Russian Chemical Reviews*. 2001, 70, 45-63.

[125] J. Ding, T. Tsuzuki, P. McCormick, and R. Street. *Journal of Alloys and Compounds*. 1996, 234, L1-L3.

[126] F. Stenger, M. Götzinger, P. Jakob, and W. Peukert. *Particle & Particle Systems Characterization*. 2004, 21, 31-38.

[127] T. Tsuzuki and P. G. McCormick. *Journal of the American Ceramic Society*. 2001, 84, 1453-1458.

[128] T. Tsuzuki and P. McCormick. *Acta Materialia*. 2000, 48, 2795-2801.

[129] A. Dodd, A. McKinley, M. Saunders, and T. Tsuzuki. *Nanotechnology*. 2006, 17, 692-698.

[130] R. Aghababazadeh, B. Mazinani, A. Mirhabibi, and M. Tamizifar. *Journal of Physics: Conference Series*. 2006, 26, 312-314.

[131] W. Liu and P. G. McCormick. *Journal of Magnetism and Magnetic Materials*. 1999, 195, 279-283.

[132] A. Gabay, X. Hu, and G. Hadjipanayis. *Journal of Magnetism and Magnetic Materials*. 2014, 368, 75-81.

[133] H. G. Cha, Y. H. Kim, C. W. Kim, H. W. Kwon, and Y. S. Kang. *The Journal of Physical Chemistry C*. 2007, 111, 1219-1222.

[134] N. G. Akdogan, G. C. Hadjipanayis, and D. J. Sellmyer. *Nanotechnology*. 2010, 21, 295705.

[135] H. G. Cha, Y. H. Kim, C. W. Kim, and Y. S. Kang. *Nanotechnology Materials and Devices Conference, 2006. NMDC 2006. IEEE*. 2006, 1, 656-657.

[136] C. Yang and Y.-L. Hou. *Rare Metals*. 2013, 32, 105-112.

[137] W. F. Li, A. M. Gabay, X. C. Hu, C. Ni, and G. C. Hadjipanayis. *Journal of Physical Chemistry C*. 2013, 117, 10291-10295.

[138] D. Restrepo *et al. Chemical Communications*. 2013, 49, 707-709.

Chapter 3

Experimental Methodology

The experimental procedures and characterization techniques utilized in this thesis are illustrated in this chapter. The procedures employed for the synthesis of the magnetic particles are described. Several characterization methods, including X-ray diffractometry (XRD), scanning electron microscopy (SEM), transmission electron microscopy (TEM), physical property measurement system (PPMS) and etc. were used for structural and property evaluation of these particles. The working principles and the parameters used for characterization are described. The rationale for method selection is also illustrated.

3.1 Rationale for methods selection

Conventional physical methods to process Nd-Fe-B based magnetic materials include melt spinning, hydrogenation-disproportionation-desorption-recombination (HDDR), sintering and etc. [1]. All these methods requires high purity elemental powders as precursors, which greatly increases the processing cost. Recently, chemical methods such as the reduction-diffusion process, sol-gel process, solvothermal process etc. were developed to overcome the limitation of high precursor cost. However, these chemical methods are difficult to scale up and they produce Nd-Fe-B based magnetic particles with limited magnetic properties. The mechanochemical method, which uses high energy ball mill, initiates chemical reactions through the mechanical energy input of ball milling has been employed in various applications, for example, the synthesis of metal-organic frameworks, pharmaceutical co-crystals, inorganic and intermetallic materials and etc. It has also been used to prepare hard magnetic particles including Sm_2Co_{17}, $Nd_2Fe_{14}B$ and $LaCo_5$ [2-5]. The mechanochemical method is low cost, scalable, and provides reasonable microstructural control. It also benefits from the advantages of physical ball milling, e.g., (a) well-defined process parameters, due to an enclosed reaction environment, (b) producing particles with grain size in the nanometer range, (c) alloying of elements which are difficult to incorporate by conventional methods. Hence, the mechanochemical method was chosen to produce Nd-Fe-Co-B based magnetic particles.

3.2 Synthesis of $Nd_2(Fe, Co)_{14}B/(Nd_{1-x}Dy_x)_2(Fe,Co)_{14}B$ based magnetic particles

In this section, the synthesis of single phase $Nd_2(Fe, Co)_{14}B/(Nd_{1-x}Dy_x)_2(Fe,Co)_{14}B$ based magnetic particles by mechanochemical milling, annealing and by-product removal is described. The procedure for magnetic alignment of these synthesized particles is also described.

3.2.1 Synthesis of $Nd_2(Fe, Co)_{14}B/(Nd_{1-x}Dy_x)_2(Fe,Co)_{14}B$ based magnetic particles – high energy ball milling

Commercially available Nd_2O_3 (99.9%, Alfa Aesar), Dy_2O_3 (99.9%, Alfa Aesar), (Fe_2O_3 (99.9%, Sigma Aldrich), CoO (99.9%, Alfa Aesar), B_2O_3 (99.9%, Alfa Aesar) powders and Ca granules (99.9%, ~ 6 mesh, Sigma Aldrich) were selected as starting materials during the mechanochemical ball milling process. Additional CaO powder (99.9% Sigma Aldrich) was added as diluent into the precursors. Before processing, CaO, Nd_2O_3 and Dy_2O_3 powders were heated at 1000 °C for 10 h to eliminate crystalline hydrates and moisture. The precursors and diluent were weighed and mixed via hand grinding in a mortar prior to be placed in the milling bowl. The composition of the mixture was determined by the following reaction:

$$xDy_2O_3 + (1-x)Nd_2O_3 + 6Fe_2O_3 + 2CoO + 0.5B_2O_3 + 24.5Ca \rightarrow (Nd_{1-x}Dy_x)_2Fe_{12}Co_2B + 24.5\,CaO$$

50 wt% excess Dy_2O_3 and Nd_2O_3 were added to offset potential elemental loss during processing. Superaddition of 100 wt% Ca granules were placed to ensure complete reduction. Additional CaO (0 wt%, 25 wt%, 50 wt% and 75 wt%) was also added as a diluent into the precursors, serving as a dispersant to prevent agglomeration.

In a typical experiment, 5 g of precursors + diluent were mixed, loaded and sealed in a tungsten carbide milling vial in a glovebox with argon atmosphere. A Fritch Pulverisette-7 planetary ball mill was utilized to perform high energy ball mill with a ball to powder ratio (BPR) of 14:1, over a range of ball milling speeds (450 rpm, 500 rpm, 550 rpm and 600 rpm) and a range of milling durations (5 min to 6 h). These sets of milling speeds and milling times were selected to ensure the deformation of the precursors during the milling process. High milling speeds or prolonged milling times were avoided to minimize contamination. The BPR of 14:1 was selected to keep a ball charge filling ratio of ~ 25% - 35 %, which is recommended to maximize throughput [6]. To avoid temperature rise, the ball mill was pulsed for 20 min for every 10 min of run. Then the black pyrophoric as milled powder samples were gathered in an argon glove box, followed by cold pressing to form pellets for further processing. Figure 3.1 shows a schematic of this mechanochemical synthesis process to produce Nd-Fe-B based magnetic particles. It can be seen from Figure 3.1b that both physical deformation and chemical reaction were experienced by the precursor oxides during high energy milling.

3.2.2 Synthesis of $Nd_2(Fe, Co)_{14}B/(Nd_{1-x}Dy_x)_2(Fe,Co)_{14}B$ magnetic particles – annealing

After the as milled powders were cold pressed into pellets, the pellets were loaded into a vacuum furnace for heat treatment in high vacuum (better than 10^{-5} torr) at 850 °C for 90 min, followed by furnace cooling. The melting temperature of metallic Ca is 849 °C. The annealing time of 90 min and temperature of 850 °C were selected to ensure reduction of the precursor oxides to form $Nd_2(Fe, Co)_{14}B/(Nd_{1-x}Dy_x)_2(Fe,Co)_{14}B$.

3.2.3 Synthesis of $Nd_2(Fe, Co)_{14}B/(Nd_{1-x}Dy_x)_2(Fe,Co)_{14}B$ magnetic particles – by-product removal

The heat treated pellets were removed from the vacuum furnace after cooling. The pellets were then hand ground into fine powders in a mortar. These powders mainly contains 2 phases: the desired $Nd_2(Fe,Co)_{14}B/(Nd_{1-x}Dy_x)_2(Fe,Co)_{14}B$ phase and the by-product CaO phase. By dissolving 2 grams of NH_4Cl (99.9%, Sigma Aldrich) in every 100 ml of methanol (99.99%, Fisher UK), a by-product removal recipe was prepared. The powder samples were mechanically stirred within the NH_4Cl/methanol solution for 30 min at a stirring speed of 500 rpm, followed by magnetic separation and 3 h vacuum drying to remove CaO. The NH_4Cl/methanol solution has been previously used for CaO removal from other nanoparticles [7, 8]. This solution was selected due to the following reasons: (1) NH_4Cl reacts with CaO to form $CaCl_2$, which can be easily dissolved in methanol; (2) the reaction is not exothermic, which minimizes oxidation of Nd-Fe-B based nanoparticles; (3) no water-based solution was used in order to prevent formation of the soft $Nd_2(Fe,Co)_{14}BH_x/(Nd_{1-x}Dy_x)_2(Fe,Co)_{14}BH_x$ phases. The desired $Nd_2(Fe,Co)_{14}B$ or the $(Nd_{1-x}Dy_x)_2(Fe,Co)_{14}B$ phase can be obtained after by-product removal (Figure 3.1e).

3.2.4 Synthesis of $Nd_2(Fe, Co)_{14}B/(Nd_{1-x}Dy_x)_2(Fe,Co)_{14}B$ magnetic particles – magnetic alignment

For better sample properties, magnetic alignment were performed on selected samples. A small amount of powder sample was sonicated within an adhesive and then aligned and dried on a glass slide under 1.8 T magnetic field for 20 min. The 1.8 T uniform magnetic field was provided by an electromagnet (DXSB-178, Dexing Magnet Tech. Co., Ltd). Figure 3.2a indicates the electromagnet setup for magnetic alignment, a uniform magnetic field was provided during the immobilization of sample particles in the adhesive. Figure 3.2b illustrates the effects of magnetic induced crystallographic alignment on the magnetic properties. Magnetic alignment greatly improves the remanent magnetization M_r and the maximum energy product $(BH)_{max}$.

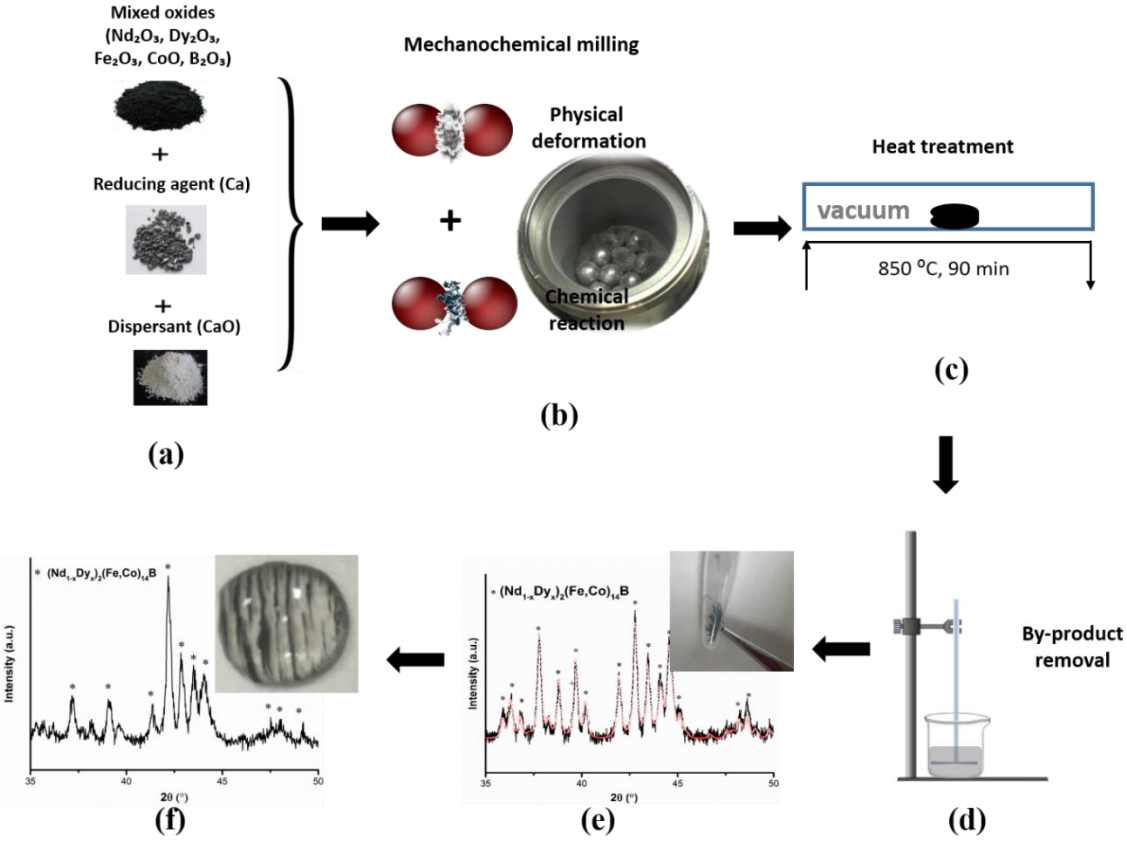

Figure 3.1. (a) Schematic of the mechanochemical process to produce $(Nd_{1-x}Dy_x)_2(Fe,Co)_{14}B$ particles: (a) low cost precursors (Nd_2O_3, Dy_2O_3, Fe_2O_3, CoO, B_2O_3, CaO powders and Ca granules); (b) mechanochemical milling induced physical deformation and chemical reactions in the precursors; (c) heat treatment of the as-milled sample at 850 ^{0}C for 90 min; (d) mechanical stirring assisted removal of by-product (CaO) in a NH_4Cl/methanol solution; (e) generation of $(Nd_{1-x}Dy_x)_2(Fe,Co)_{14}B$ magnetic particles; (f) magnetic aligned $(Nd_{1-x}Dy_x)_2(Fe,Co)_{14}B$ particles embedded in an adhesive.

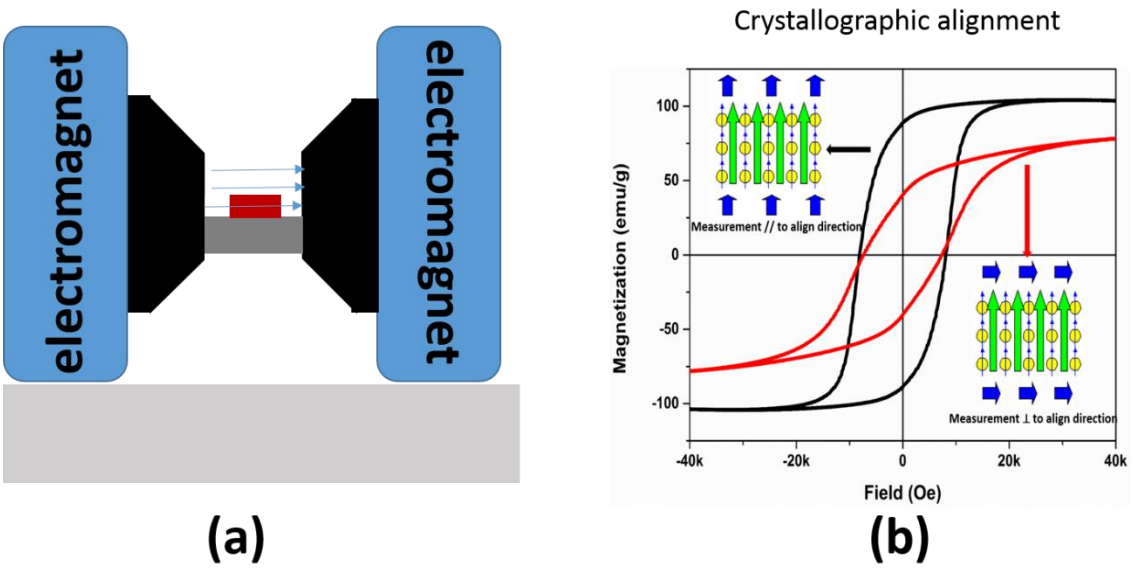

Figure 3.2. (a). Illustration of the magnetic alignment setup, the aligned samples were placed under the uniform magnetic field provided by an electromagnet; (b) illustration of the influence of magnetic alignment on the sample properties.

3.3 Materials characterizations

After the synthesis of Nd-Fe-Co-B based magnetic particles, suitable characterization techniques were utilized to determine their properties, including morphology, structure, magnetic properties and etc. XRD and the Rietveld refinement method were used to provide both crystallographic and quantitative information of each phase. The working principles of each characterization technique used in this thesis are briefly introduced.

3.3.1. X-ray diffraction

A Nobel Prize in Physics was given to Wilhelm Conrad Rontgen in 1901 for the discovery of the X-rays. After that, the X-ray diffraction was discovered by Max von Laue in 1912 [9]. Soon after that, Bragg and his father succeeded in analyzing crystal structure via X-ray diffractions, which grand them the Nobel Prize in 1915. Since then, X-ray diffraction has been utilized as a new method for chemical analysis. As A. W. Hull points out, in X-

ray diffraction, each crystalline substance has its own “footprint”. This “footprint” can be used to identify the corresponding crystalline substance in a multiphase system [10]. The X-ray diffraction patterns is a fingerprint of that substance, X-ray diffraction is an excellent characterization method to identify crystalline phases. More than 300,000 entries of diffraction patterns have been stored as references in a database. Through a simple search/match procedure within the database, the phases in a certain sample can be identified. In addition, by correlating the area under the diffraction peaks to the content of each phase in the sample, semi-quantitative analysis can be performed.

When the atom within a solid sample is hit by an incident X-ray beam, the electrons surrounding the atom will oscillate at the same frequency as the incident X-ray. If the atoms in a solid crystal are orderly patterned, constructive interference of the scattered X-rays will be observed in some directions. Constructive interference is due to in-phase electromagnetic waves.

Figure 3.3 illustrates the working principle of a X-ray diffractometer. A beam of incident X-rays will be generated by the cathode tube. When this beam interacts with the crystal lattice, interference patterns will be created. If the diffraction angle θ meets the requirements of Bragg’s law ($2dsin\theta = n\lambda$), the diffracted beam will be picked up by the XRD detector and shows up in the XRD diffractogram. The electron distribution within the unit cell determines the intensity of the diffraction peaks in the XRD diffractogram. Due to the high electron density around the atoms, planes with a high atomic density will reflect strongly and show high diffraction intensity in XRD patterns. Therefore, XRD can be used to identify different crystal structures using Bragg’s law ($2dsin\theta = n\lambda$), where d refers to the lattice spacing, θ represents the diffraction angle, n represents an integer and λ corresponds to the wavelength of incident beam.

To investigate the sample crystal structure, a Bruker D8 ADVANCE Diffractometer which operated at 40 kV, 30 mA and employed Cu Kα radiation (λ=1.5418 Å) as the X-ray source was utilized to measure the X-ray diffractions (XRD) of the samples. Powder samples were pressed against the sample holder using a glass slide. The XRD measurements were

performed over a 2θ range from 10^0 to 120^0, at a step size of 0.01^0 and a scan rate of 0.1^0/s. Phase identification of the samples was performed by matching the diffraction peak positions to reference data using the MATCH program. TOPAS 4.1 program was employed for quantitative analysis and crystal structure analysis.

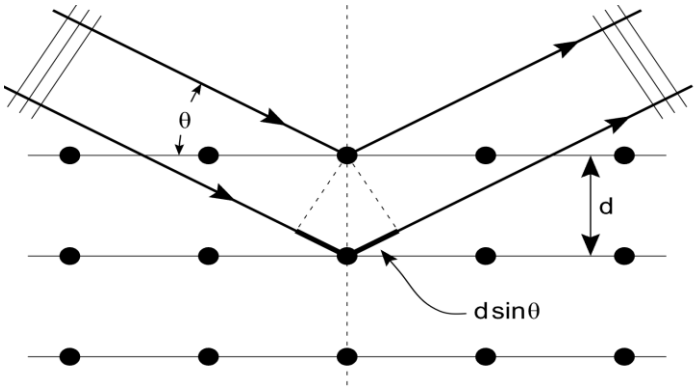

Figure 3.3. Schematic of X-ray diffraction from a crystal lattice [11].

3.3.1.1. The Rietveld method

Conventional powder diffraction is a good method for the identification of compounds. However, phase determination and microstructural parameters become difficult to obtain when diffraction peaks overlap in a multiphase system. This limitation can be overcome by utilizing the Rietveld method. In this method, the contribution of individual phases to the overlapping peaks can be separated using suitable structural models, allowing determination of the structure which is usually of comparable accuracy with the results obtained by single crystal diffraction techniques. Since most materials are not available as single crystals, the Rietveld method has found many applications in the characterization of polycrystalline powder.

In the Rietveld method, the experimental pattern (observed data) was compared with a profile model which is simulated from the instrumental parameters and the hypothesized crystal structure, the user-input parameters were refined to reduce the variance between them via a least squares refinement algorithm (Equation 3.1). Crystallographic information,

including atomic coordinates, lattice parameters, crystal symmetry and site occupancies with suitable physical and chemical meaning are input into this model. These crystallographic parameters are then systematically and independently varied to obtain the best fit between calculated and observed data. The crystallographic and quantitative information of each phase in a mixed phase system can be obtained through fitting. The criteria is that S defined below, should be a minimum.

$$S = \sum_i w_i(y_i(obs) - y_i(calc))^2 = Minimum \tag{3.1}$$

w_i: statistical weight, which is related to the standard deviation.

y_i: the observed (or calculated) intensity at each step

The mass fraction of each crystalline phase in a multiphase system can be estimated through a relationship put forward by Hill and Howard in 1987 [12]:

$$W_\alpha = \frac{S_\alpha(ZMV)_\alpha}{\sum_{j-1}^{n} S_j(ZWV)_j} \tag{3.2}$$

where S_α is the Rietveld scale factor for phase α, *n* is the number of phases in the Rietveld analysis, ZM is the unit cell mass and *V* represents the unit cell volume. This method assumes that there is no amorphous phase in the sample and all phases are considered during the analysis.

Although the quantitative analysis for crystalline materials via the Rietveld method is straightforward, it is difficult to use this method for poorly crystalline or amorphous materials. The traditional Rietveld method yields only the relative phase amounts for a multiphase system, and omits the amorphous phases. When poorly crystalline or amorphous phases are present, the analyzed mass fractions of the crystalline phases may be significantly over-estimated. Hence, it is essential to have another quantitative analysis method for the analysis of amorphous content. In the TOPAS software, different quantitative methods can be used together with the Rietveld refinement method to determine the actual phase content in a multiphase system with amorphous phases. The two categories used are listed as below.

1. When the individual unidentified and amorphous phases can be distinguished in the diffraction pattern, direct methods can be used. In these methods, through analyzing the intensity contribution of amorphous phase to the overall diffraction pattern, the amount of amorphous content can be estimated. If data quality is sufficient, the content of more than one amorphous phase can be identified. However, direct methods can only applied when the intensity contribution of the amorphous phases can be clearly identified.
2. When the individual unidentified and amorphous phases are hard to distinguish from the diffraction pattern, indirect methods are needed. In these methods, known amount of internal standards were added into the sample before XRD measurement. During the XRD analysis, only crystalline components are considered and analyzed. Then an absolute scale is put onto the amount of the crystalline components. The content of amorphous phase can be subsequently calculated by difference. However, these methods only estimates the sum of the amorphous phase content and the unidentified phase content, they cannot resolve the difference between these phases. In the case where no evident intensity contribution from amorphous phases to the diffraction pattern was observed, indirect methods are usually used.

In this project, the indirect method was used to analyze the amorphous phase content. An internal standard material (with a known weight fraction) is added to the sample, which allows the phase content calculated by the Rietveld method to be corrected according to Equation 3.3:

$$Corr(W_\alpha) = W_\alpha \frac{STD_{known}}{STD_{measured}} \tag{3.3}$$

where $Corr(W_\alpha)$ is the corrected weight percentage, STD_{known} represents the weight fraction of the internal standard, $STD_{measured}$ is the weight fraction derived from the Rietveld refinement method.

Once the corrected contents of the crystalline phases are calculated, the amount of the amorphous phases $W_{amorphous}$ can be derived by Equation 3.4:

$$W_{amorphous} = 1 - \sum_{j-1}^{n} Corr(W_j) \quad (3.4)$$

TOPAS 4.1 program was used to perform Rietveld refinement analysis of the diffraction patterns via the above-mentioned least-square fitting procedure. A pseudo-Voigt peak profile, which combines both Lorentzian and Gaussian functions, was employed to simulate the observed diffraction peak shape. The refinement starts with fitting the full scale experimental XRD pattern (2θ = 10^0 - 120^0) using a polynomial function of degree 1-2, zero error correction, refinement of scale factors and lattice parameters of each phase and finally, refinement of crystal size using both the Lorentzian and the Gaussian function. Systematic refinement was performed until the refinement converged with a GOF (goodness of fitting) less than 2. For quantitative analysis and determination of the amorphous phase content, the indirect approach together with the Rietveld refinement method was utilized, ~ 5wt% standard CeO_2 or Si (NIST, 99.9%) was added to the powder sample as an internal standard, before collecting X-ray diffraction patterns.

3.3.2. Transmission electron microscopy

Transmission electron microscopy (TEM) is a technique to observe high-resolution images of nanomaterials. An electron beam with a high accelerating voltage is emitted from the electron gun and interacts with an ultrathin specimen (usually less than 100 nm). Morphological, compositional and crystallographic information can be obtained as the electron beam is transmitted through and interacts with the specimen. Currently, the TEM technique is a powerful tool to provide detailed information on nanomaterials, including crystallinity, grain boundary, particle size, interphase distance and elemental composition. The morphology and size of the synthesized Nd-Fe-B based nanoparticles can be directly observed via TEM images.

The reason for the high resolution of TEM is due to the high speed of electrons in the electron beam. Electrons have a much smaller de Broglie wavelength ($\lambda = \frac{h}{\sqrt{2meV}}$) compared to light. According to Abbe's equation (resolution = $\frac{0.61 * \lambda}{n * sin\alpha}$), the smaller

wavelength enables better resolution, which allows detailed observation of samples by the TEM.

High resolution TEM images (HR-TEM) and selected area diffraction (SAED) patterns were used in crystal structure and crystal orientation analysis of the Nd-Fe-B based nanoparticles. The HR-TEM images can also be used for particle size determination. By measuring the distance between the crystal lattice fringes in HR-TEM images, the distance between those crystal lattice planes can be estimated. This method can also be used to deduce the crystallinity. In the HR-TEM mode, the amorphous region will not display a crystal lattice while lattice fringes will be shown in crystalline regions. The SAED patterns can also provide information on the crystallinity of the sample. For example, the SAED patterns of single crystals are usually bright dots while polycrystalline samples have a ring-like pattern. In this study, the different phases in a multiphase system were deduced via HR-TEM by measuring the distance between the lattice fringes. The crystallinity of the Nd-Fe-Co-B particles was obtained from the SAED patterns. The composition and elemental distribution within these particles can be identified by the EDS spectra and the corresponding element maps.

Powder samples were prepared by dispersing powders in ethanol by ultra-sonication for 10 min. This dispersion was dropped onto the copper grid and vacuum dried for several hours. TEM observations were made in bright field, high resolution and diffraction modes using a JEOL 2010 or JEOL 2100 F transmission electron microscope at an operating voltage of 200 kV under a vacuum better than 10^{-5} torr.

3.3.3. Scanning electron microscopy

Scanning electron microscopy was employed to determine sample morphology, size distribution and elemental analysis. Scanning electron microscopy provides information on sample morphology by scanning the sample surface with a focused electron beam. The sample interacts with the incident electron beam and the different signals containing information on the sample morphology and composition will be emitted and picked up by

various signal detectors. Figure 3.4 shows the typical signals emitted from different parts of the interaction volume during the sample - electron beam interaction [13].

Typical modes in scanning electron microscopy includes backscattered electron image (BEI), secondary electron image (SEI), and energy dispersive X-ray (EDX). The most common mode is the SEI mode, which provides information by detecting the interaction signals from secondary electrons. The secondary electrons (<50 eV) are generated from the k-shell of the atoms in the specimen by inelastic scattering interactions with the electron beam. These electrons are usually generated within the top few nanometers from the sample surface, and can provide topographic information. The backscattered electron image mode is another common mode. The BEI image is formed by collecting the reflected or back-scattered high-energy electrons from the incident electron beam after elastic scattering interactions between the atoms of the sample and the electron beam. As the heavy atoms with large atomic numbers reflect/scatter electrons more strongly than light atoms with smaller atomic numbers, regions with heavier atoms will appear brighter in the BEI images. The BEI mode is usually used to differentiate regions with different chemical compositions or identify different phases in a multi-phase sample. Another commonly used mode is the energy dispersive X-ray analyser (EDX) mode. In this mode, elemental analysis or chemical characterization of a sample can be performed. In the ground state, electrons with discrete energy levels are in different shells of an atom. Upon interaction of the sample with the incident electron beam, the electrons of an inner shell can be excited and ejected from their original position, leaving behind a “hole”. As all electrons favor lower energy state, an electron originally in the outer shell will subsequently jump to the “hole” and emits the excess energy in the form of X-rays, which will be picked up by the energy-dispersive spectrometer. The atomic structure and the difference in energy between shells vary with composition. Hence, EDX allow characterization of the composition of the specimen.

In this study, FESEM JEOL7600 was utilized to reveal the sample morphology and composition.

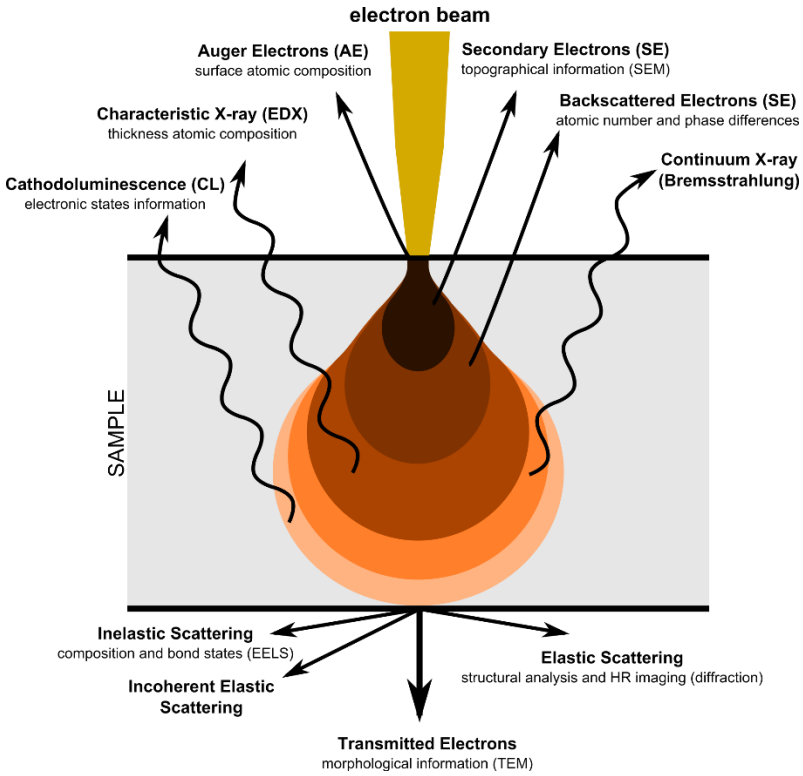

Figure 3.4. Signals from various parts of the interaction volume upon interaction of electron beam and the sample [13].

3.3.4 Differential scanning calorimeter

Measurements done by a differential scanning calorimeter (DSC) was utilized to perform the activation energy calculations for the chemical reactions taking place during the mechanochemical process. DSC is a thermoanalytical technique which records the heat absorbed/released in an isochronal or isothermal condition (Figure 3.5). In the isochronal mode, heat is measured by tracking the temperature difference between a reference and the sample. The temperature increase of the sample holders are usually pre-programed, any temperature deviation of the sample due to the energy released or absorbed will be revealed in the form of heat vs. temperature profile. This temperature deviation is usually caused by a chemical reaction or physical phase change, it leads to a peak (T_p) in the measured profile. For example, heat release or an exothermic peak is observed for crystallization or exothermic reactions. Heat absorption or an endothermic peak is usually observed for melting or endothermic reactions. For first order reactions, Kissinger model provides a

method to estimate the activation energy (E_a) for a specific reaction occurring at a certain temperature (T_p) [14, 15]. At different heating rate, different reaction occurring temperature(T_p) will be observed in the respective isochronal DSC thermograms, and the relationship between heating rate b and peak position (T_p) is shown below:

$$ln\frac{b}{T_p{}^2} = -\frac{E_a}{RT_p} + C_2 \tag{3.5}$$

In this study, the isochronal DSC thermograms were measured in a SDT Q600 DSC calorimeter from 25 °C to 900 °C for the thin Ca flakes and the precursor oxides, with various heating rates from 5 to 20 K/min, to calculate the overall activation energy E_a needed for the reduction reaction during the mechanochemical process. During the measurement, ~ 10 mg of precursors were loaded into the sample holder, with continuous argon purge to provide an inert reaction atmosphere.

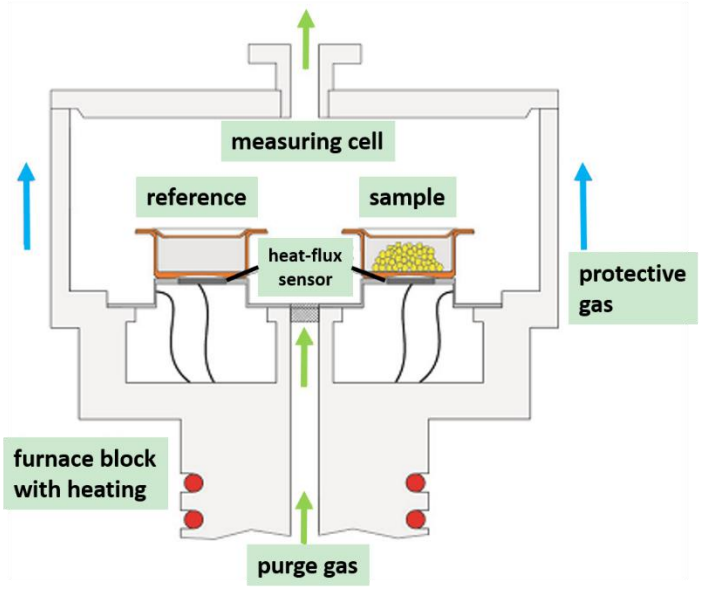

Figure 3.5. Schematic of a typical differential scanning calorimeter (SDT Q600).

3.3.5. Vibrating sample magnetometer

A vibrating sample magnetometer (Lakeshore VSM3.1) was employed to test the room temperature magnetic properties of selected samples at a maximum applied field of 1.45 T. The VSM magnetometer was first calibrated using a pure nickel standard sample. During sample measurement, about 10 mg of powder were wrapped in Teflon tape and placed into

the powder sample holder, then rigidly screwed to the tail of the sample rod. A head motor drives the sample rod to move up and down rapidly in a varying magnetic field. The sample's response to the external applied magnetic field was picked by a coil and recorded by the VSM to form a magnetic hysteresis loop.

Faraday's law governs the VSM working principle: a change in flux through the coil will induce an electric voltage in the coil. During the measurement, the magnetic sample vibrates in the vertical direction (Figure 3.6), therefore, a change in flux will be generated and picked up by the coil. A more detailed explanation is presented in section 3.3.6.

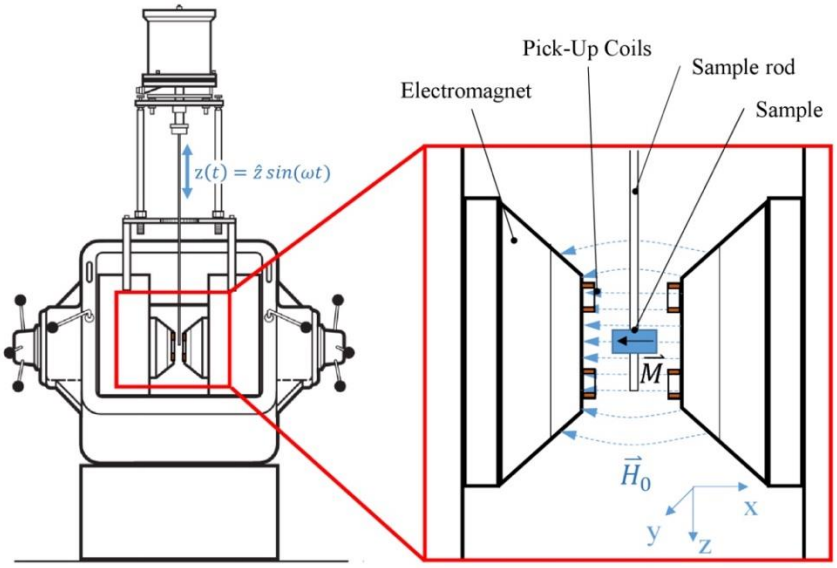

Figure 3.6. Schematic of a typical vibrating sample magnetometer [16].

3.3.6. Physical properties measurement system

A physical property measurement system (PPMS) (EverCool-II, Quantum Design Inc., USA), attached with a vibrating sample magnetometer (VSM) probe was used to measure the magnetic properties (e.g. coercivity and magnetization). This equipment is a fully automated, sensitive and fast DC magnetometer for magnetic properties measurement. It has a working temperature range of 1.9 K – 400 K, a maximum magnetic field of up to 5 T and a sensitivity of ~ 10^{-6} emu.

The main components in the VSM mode of the PPMS is listed as follows: a VSM head (linear motor) which drives the sample vibration, a pick-up coil set which pick up the signal, electronics which detects the response from the pick-up coils, and MultiVu software which control and automate the VSM in PPMS. During measurement, driven by the linear motor, the sample holder rod oscillates sinusoidally and sample is glued to the sample end tail. The design of PPMS and sample preparation make sure the sinusoidal oscillation centers at the vertical center of the pick-up coil. The oscillation of sample will induce a changing magnetic flux in the pickup coil. Based on Faraday's law of induction, a varying magnetic flux will introduce a voltage in the pickup coil, which is then amplified and detected in the detector.

The time-dependent induced voltage in coil can be described by equation below:

$$V_{Coil} = \frac{d\phi}{dt} = (\frac{d\phi}{dZ})(\frac{dZ}{dt})$$

where ϕ represents the magnetic flux, Z refers to the vertical position of the sample respect to the pickup coil and t is the time.

For a sinusoidally oscillating sample mode (typical oscillating mode in VSM), the induced voltage can be re-written as

$$V_{Coil} = 2\pi fCmAsin(2\pi ft)$$

where C refers to a coupling constant, m represents the sample DC magnetic moment, A indicates the oscillation amplitude and f indicates the oscillation frequency.

Figure 3.7 illustrates the operating principle of the VSM mode of the PPMS.

The working principle of the VSM mode in PPMS is similar to that of the VSM introduced in the previous section. The difference between these equipments lies in the strength of the applied field. In the PPMS system, the external magnetic field is supplied by superconducting magnets and cooled by helium, hence, much larger external magnetic field can be generated. In this PPMS, a magnetic field as large as 9 T can be generated. For the abovementioned vibrating sample magnetometer, a conventional electromagnet is utilized

to generate the applied field. Besides, only water assisted cooling is used to cool the system. Therefore, the VSM can only generate field of less than 2T.

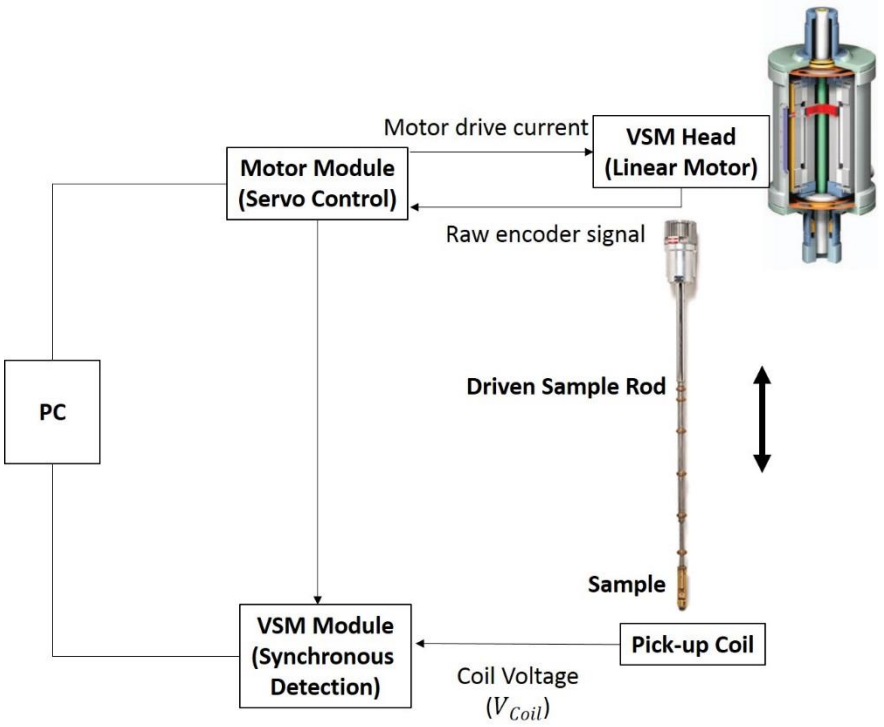

Figure 3.7. Operating principle of VSM mode in PPMS [17].

In this project, the room temperature magnetic hysteresis loops of all samples were measured at 300 K under an applied magnetic field of 5T. The temperature-dependent magnetic hysteresis loops of selected samples were measured from 100 K to 400 K in the same field. For measuring the spin re-orientation temperature, the temperature dependence of magnetization was measured in a 0.1 T applied magnetic field from 10 K to 300 K.

References

1] O. Gutfleisch. *European School on Magnetism: New Experimental Approaches in Magnetism*, Constanta. **2005**, 1-7.

[2] W. Liu and P. McCormick. *Journal of Magnetism and Magnetic Materials*. **1999**, 195, 279-283.

[3] A. Pal, A. Gabay, and G. C. Hadjipanayis. *Journal of Alloys and Compounds*. **2012**, 543, 31-33.

[4] A. Gabay and G. Hadjipanayis. *Journal of Physics D: Applied Physics*. **2014**, 47, 182001.

[5] A. Gabay, X. Hu, and G. Hadjipanayis. *Journal of Magnetism and Magnetic Materials*. **2014**, 368, 75-81.

[6] R. Schnatz. *International Journal of Mineral Processing*. **2004**, 74, S55-S63.

[7] T. Jang, D. Lee, and S. Namkung. *Reviews on Advanced Materials Science*. **2011**, 28, 212-216.

[8] S. Yamamoto and M. Tsujimoto. *RSC Advances*. **2015**, 5, 100084-100088.

[9] M. Eckert. *Annalen der Physik*. **2012**, 524, pA83-pA85.

[10] A. W. Hull. *Journal of the American Chemical Society*. **1919**, 41, 1168-1175.

[11] B. Borie. *Journal of the American Chemical Society*. **1965**, 87, 140-141.

[12] R. Hill and C. Howard. *Journal of Applied Crystallography*. **1987**, 20, 467-474.

[13] J. I. Goldstein, D. E. Newbury, J. R. Michael, N. W. Ritchie, J. H. J. Scott, and D. C. Joy, *Scanning Electron Microscopy and X-ray Microanalysis*. Boston, MA: Springer US, **2017**.

[14] P. Deheri, S. Shukla, and R. V. Ramanujan. *Journal of Solid State Chemistry*. **2012**, 186, 224-230.

[15] H. E. Kissinger. *Analytical Chemistry*. **1957**, 29, 1702-1706.

[16] LakeShoreCryotronics. *User's Manual 7300 Series VSM System.* **2001**, http://www.lakeshore.com/obsoleteAndReseaerchDocs/7300_Manual.pdf.

[17] QuantumDesign. *PPMS Vibrating Sample Magnetometer Application Note*. **2009**, https://www.qdusa.com/sitedocs/appNotes/vsmappnote_5-09.pdf.

Chapter 4 *

Effect of Diluent (CaO) Content on the Mechanochemical Synthesis of $Nd_2(Fe,Co)_{14}B$ Nanoparticles

With increasing demand of high performance permanent magnets in technological applications, the quest to develop novel processing methods to fabricate better permanent magnets becomes more urgent. Herein, a novel mechanochemical method for the process of high coercivity $Nd_2(Fe, Co)_{14}B$ magnetic nanoparticles is reported. During the process, the reduction of precursor oxides (Nd_2O_3, Fe_2O_3, CoO and B_2O_3) by Ca granules in the presence of a CaO diluent is observed. The role of process parameters, i.e., content of diluent (CaO), has been studied. The change of CaO content varied the $Nd_2(Fe, Co)_{14}B$ formation mechanism. The crystallite sizes of $Nd_2(Fe, Co)_{14}B$ particles increased and their coercivity enhanced with larger CaO content.

*The content of this section is published substantially as reference:

Y. Zhong, V. Chaudhary, X. Tan, H. Parmar and R. V. Ramanujan. Mechanochemical synthesis of high coercivity $Nd_2(Fe, Co)_{14}B$ magnetic particles. *Nanoscale* 9, 18651-18660 (2017).

4.1 Introduction

Nd-Fe-B type hard magnets are valuable materials for energy conversion systems due to their superior magnetic properties. The Curie temperature of Nd-Fe-B can be effectively increased by replacement of Fe by Co, with minimal deleterious effects on the magnetization and coercivity. Hence, Nd-Fe-Co-B magnets are commonly utilized in higher Curie temperature applications. The interest in high coercivity Nd-Fe-B nanoparticles has increased since Coey's prediction of the giant energy product of nanocomposite magnets. Novel chemical synthesis methods which involves less energy consumption and lower cost, including the sol-gel process, the microwave assisted combustion process, the mechanochemical process, etc. have attracted high interest due to their ability to produce hard magnetic nanoparticles with reasonable coercivity. The mechanochemcial method stands out among these methods, since it produces magnetic particles with comparatively better properties. The mechanochemical method has been employed to synthesis traditional inorganic, organic and intermetallic compounds, metal-organic frameworks, pharmaceutical co-crystals etc. [1]. For the synthesis of traditional intermetallics, the mechanochemical method exhibits advantages such as low cost, scalability, product homogeneity as well as size control [2-5]. It is now becoming a promising method to synthesis Nd-Fe-B based magnetic nanoparticles. It is a common practice to use a diluent in the mechanochemical process. Various studies have shown that the diluent content can affect the structure and properties of the synthesized particles. For the synthesis of Nd-Fe-B through the mechanochemical method, though CaO is commonly employed as a diluent, the diluent amount has been empirically determined and its influence on the properties has not yet been systematically investigated. Therefore, in this section, the influence of CaO content, was systematically investigated and the diluent content was optimized for best magnetic properties.

4.2 Results and Discussion

4.2.1 Effect of diluent (CaO) on structural properties

Only a few reports were made so far on the synthesis of $Nd_2Fe_{14}B$ magnetic particles via the mechanochemical process. In these reports, usually a diluent, such as CaO, was mixed into the reactant precursors [3, 4]. However, studies have yet been made on analyzing the effect of diluent (CaO) on the formation mechanism, properties and crystal structure of the synthesized Nd-Fe-B particles. A range of diluent content, from 0 wt% to 75 wt%, were added into the reactant mixture, and the effect of diluent (CaO) content on the magnetic and structure properties of the synthesized $Nd_2(Fe, Co)_{14}B$ were investigated. Figure 4.1 shows the X-ray diffraction diffractograms of as milled samples with different CaO content. With 0 wt% and 25 wt% CaO in the starting materials, no precursor oxide peaks were present and a new α-Fe phase was formed (Figure 4.1a and Figure 4.1b). These observation indicated that during milling process, a reduction reaction occurred and a reduced product, i.e., α-Fe phase, was introduced. In the case when larger CaO content (50 wt% and 75 wt%) was added into the precursors, only broadened oxide precursor peaks without new phase formation were observed (Figure 4.1c and Figure 4.1d). Hence, no reduction reaction occurred with larger CaO content and ball milling only induced the crystal size reduction, which led to the peak broadening. Therefore, CaO behaves as a diluent which decreases the reactant concentration in the starting materials and reduces the milling intensity. It slows the reduction reaction rate. With larger CaO content and slower reaction rates, a larger amount of precursor oxide would remain within the as milled samples.

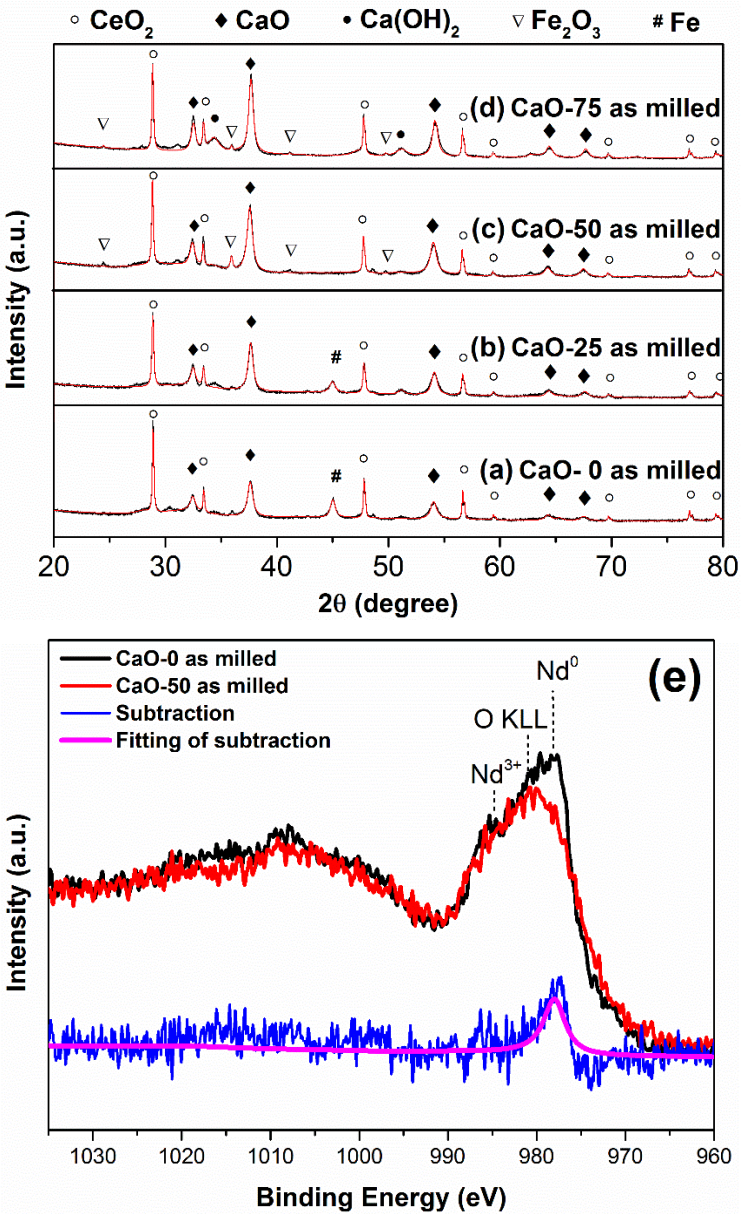

Figure 4.1. X-ray diffraction patterns and Rietveld refinements of as milled samples: (a) CaO-0, (b) CaO-25, (c) CaO-50 and (d) CaO-75. (CaO-0 indicates that there is 0 wt% CaO in the precursor materials). The formation of α-Fe phase was observed with small CaO content ((a) and (b)), only broadened oxide peaks with no new phase formation was observed with large CaO content ((c) and (d)). 5wt% crystalline CeO_2 was added in each sample for quantitative analysis. (e) High-resolution X-ray photoelectron spectroscopy of Nd element for as milled CaO-0 and CaO-50 sample.

Figure 4.1 presents the XRD of the as milled samples. With different CaO content, there are different phases present in samples, suggesting that the formation mechanism changes

with CaO content. For the case of CaO-50, only broadened Fe_2O_3 and CaO diffraction peaks were observed. The observation of the Fe_2O_3 peaks indicates that the reduction of the precursor oxides was not readily induced by milling. The milling only induced the reduction of crystal size, which gave rise to the broadened diffraction peaks. Hence, the formation of tetragonal $Nd_2(Fe, Co)_{14}B$ was introduced by the subsequent annealing process, where a solid-state reduction-diffusion took place. This is identical to the observation made during the sol-gel or microwave-assisted annealing processes [6, 7]. On the other hand, with less CaO content (CaO-0, CaO-25), only CaO peaks and broadened α-Fe peaks were found in the as milled samples (Figure 4.1a and b). These observations indicated that with smaller CaO content, majority of the reduction reactions were induced during the milling process. High resolution XPS in the Nd 3d region of the as milled CaO-0 and CaO-50 samples were analyzed to confirm this understanding (Figure 4.1e). Due to the overlapping of the Nd 3d peaks with the O KLL peak and insufficient literature on the O KLL peaks, experimental data fitting was not performed [8]. Instead, a subtraction was done between the CaO-0 profile and the CaO-50 profile to removes the O KLL peaks interference and highlight the signals from the Nd element. Contarini et al. performed a similar practice during their investigation to eliminate the disturbance of additives in the silicon carbide samples [9]. A Nd^0 peak (979 eV), O KLL peaks and a Nd^{3+} peak (982 eV) presented in the CaO-0 sample profile [8, 10]. Only the Nd^0 peak (979 eV) present after subtraction of the CaO-50 sample profile. This observation shows in the as milled CaO-0 sample, metallic Nd was introduced during milling due to partial reduction of Nd_2O_3. However, milling did not result in complete reduction of neodymium oxides, instead, the full reduction of the precursor oxides and the formation of the tetragonal $Nd_2(Fe,Co)_{14}B$ phase were only achieved during the annealing process.

Reduction of Nd_2O_3 usually presents after the reduction of Fe_2O_3. This is because there is a large difference between the redox potential of the rare-earth elements (e.g., -2.43 eV for $Nd^{3+/}Nd^0$) and the transition metals (e.g., -0.44 eV for $Fe^{3+/}Fe^0$). The reaction sequence in the reduction diffusion process during the sol-gel process to synthesis $Nd_2Fe_{14}B$ has been reported to be [11]:

Step 1: $Fe_2O_3 + 3\ CaH_2 \rightarrow 2\ Fe + 3\ CaO + 3\ H_2$

$$B_2O_3 + 3\ CaH_2 \rightarrow 2\ B + 3\ CaO + 3\ H_2$$

Step 2: $Nd_2O_3 + 3\ CaH_2 \rightarrow 2\ NdH_2 + 3\ CaO + 3\ H_2$

$$NdFeO_3 + 3\ CaH_2 \rightarrow NdH_2 + Fe + 3\ CaO + 2\ H_2$$

Step 3: $2\ NdH_2 + 14\ Fe + B \rightarrow Nd_2Fe_{14}B + 2\ H_2$

It can be seen that Fe_2O_3 reduction and B_2O_3 reduction takes place prior to Nd_2O_3 reduction. CaH_2 was commonly used as a reducing agent for the production of metal powders from their oxides (e.g. Ti, Zr, Nb, Th, U and etc.). It is proposed to operate via its decomposition to Ca metal. Therefore, in these reduction process, it is not the calcium hydride, but metallic calcium produced by thermal decomposition that acts as the actual reducing agent [11]. So we analogy the effect of Ca to the effect of CaH_2 on the metal oxide reduction process. For the mechanochemical milling process (CaO-0 and CaO-25), the presence of metallic Nd suggests that reduction was already in the final stage. The occurrence of Fe_2O_3 and CoO reduction was also confirmed by the observation of the Fe-Co phase in the as milled samples. Although neodymium oxides were not fully reduced during milling, the milling energy still served as the main driving force for precursor oxide (especially Fe_2O_3) reduction. With less CaO content (e.g., CaO-0, CaO-25), the intense milling first resulted in amorphization of all the precursor oxides. Next, the reaction between the calcium granules and precursor oxides led to the formation of the CaO and α-Fe phases. Formation of crystalline α-Fe phase was also found in the mechanical milling of Nd-Fe-B melt-spun ribbons [12, 13]. By analogy to the annealing induced reduction diffusion and pure mechanical milling process, for the case of CaO-0, there are two factors contributing to $Nd_2(Fe,Co)_{14}B$ formation: 1. the annealing induced reduction diffusion of unreacted precursor oxides by excess Ca; 2. the milling induced atomic ordering and crystallization of the disordered milled sample in the metallic state.

Hence, during the mechanochemical process, the CaO content crucially influences the $Nd_2(Fe, Co)_{14}B$ formation mechanism. For small CaO content, sufficient energy can be provided by milling to reduce the majority of the precursor oxides. However, the milling

energy is diluted with larger CaO content, and the annealing process is required to trigger the reduction of the oxides.

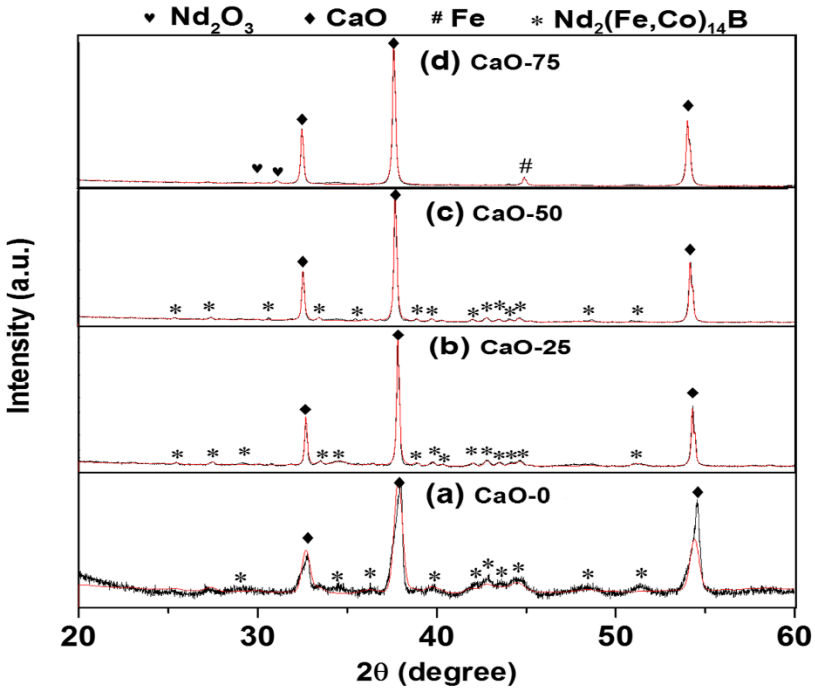

Figure 4.2. X-ray diffraction patterns and Rietveld analysis of annealed samples: (a) CaO-0, (b) CaO-25, (c) CaO-50 and (d) CaO-75. All samples were annealed in a furnace preheated to 850 ºC for 90 min and then quenched to room temperature. The tetragonal $Nd_2(Fe,Co)_{14}B$ phase was observed in (a), (b) and (c), but it cannot be found in (d).

Figure 4.2 shows the XRD patterns and Rietveld analysis of the annealed samples over a range of CaO content. The tetragonal $Nd_2(Fe, Co)_{14}B$ phase was formed in the annealed samples for CaO content of up to 50 wt% (Figure 4.2a - c). However, with addition of 75 wt% CaO, instead of the $Nd_2(Fe, Co)_{14}B$ phase, only the α-Fe phase was present after annealing. It could be in the case of CaO-75, the milling intensity was diluted too much by CaO, and the Ca granules were not able to convert into fine powders to reduce the precursor oxides, both in the milling process and the annealing process. This speculation can be validated by the observation of large metallic Ca granules in the as milled CaO-75 sample.

Rietveld analysis was utilized to calculate the average crystal size of all the samples (Table 4.1). For the as-annealed $Nd_2(Fe, Co)_{14}B$ particles, when CaO content was increased from

0 to 50 wt%, the crystallite size became larger from 11 nm to 38 nm. Small crystals with size of ~ 10 – 50 nm were also synthesized from the mechanochemical processing of Fe and FeB particles [14]. It could be that more intimate mixing occurred during the milling induced chemical reduction compared to the annealing induced reduction-diffusion, leading to the formation of smaller crystals.

Table 4.1. Average crystal size of $Nd_2(Fe, Co)_{14}B$ with different diluent (CaO) content.

		CaO-0	**CaO-25**	**CaO-50**	**CaO-75**
As-synthesized	R_{bragg}	2.476	2.291	2.568	Phase not formed
	Crystallite size $L_{vol\text{-}IB}$ (nm)	11.37 (65)	25.83 (56)	38.3 (12)	-
After by-product removal	R_{bragg}	0.971	0.929	1.195	Phase not formed
	Crystallite size $L_{vol\text{-}IB}$ (nm)	22.88 (21)	20.81 (16)	40.86 (71)	-

The by-product CaO needs to be removed due to the following reasons: 1. With additional non-magnetic byproduct CaO, the magnetization of this compound will be very low which make this material of small commercial value. 2. Due to the high melting point of CaO (2572 °C), it is very hard to compact the synthesized $Nd_2(Fe, Co)_{14}B$ together with CaO to make it a dense bulk magnet at a later stage. 3. Even a bulk magnet made of both $Nd_2(Fe, Co)_{14}B$ and CaO was achieved through compaction, the weight will need to be increased considerably to produce the same value of energy product, which is not economically efficient.

The XRD and Rietveld analysis of the by-product removed samples is shown in Figure 4.3 a-c, the TEM bright field image and diffraction pattern of the by-product removed CaO-50 is shown in Figure 4.3 d. Only the tetragonal $Nd_2(Fe,Co)_{14}B$ phase is present in both the XRD patterns and the TEM image. This proves the efficiency of the by-product removal process. The synthesized particles have sizes from 10 to 150 nm. The FWHM of diffraction peaks in Figure 4.3c are smaller comparing to the corresponding peaks in Figure 4.3a and Figure 4.3b, which indicates that the by-product removed CaO-50 possesses a larger crystal

size than the other two samples. By comparing the reference data for $Nd_2Fe_{13}CoB$ (JCPDF 04-005-2749) with the measured sample data, it can be seen there is a minor shift of the sample peaks to lower 2θ positions. This could be that minor amount of elemental H was introduced to the $Nd_2(Fe,Co)_{14}B$ structure during the by-product removal.

Figure 4.4 shows the influence of magnetic alignment on the XRD patterns of the samples. The XRD pattern of the random and the aligned $Nd_2(Fe,Co)_{14}B$ particles (by-product removed CaO-50) are shown in Figure 4.4a-4.4c, good matching was observed between the diffraction peaks of the randomly oriented sample and the $Nd_2Fe_{13}CoB$ reference (JCPDF 04-005-2749). Crystallographic alignment was induced with a magnetic alignment under a 1.8 T applied field. This field-induced texture increases the intensity of the hkl reflection peaks with large h values, e.g. (410), when measured ⊥ to the c-axis. It strengthens the hkl reflection peaks with large l values, e.g. (006), when measured // to the c-axis. Similar influence of alignment was also found in $Nd_2Fe_{14}B$ in Meisner's study [15]. This observation shows that the synthesized particles response strongly to the external magnetic field and can be crystallographic aligned.

Figure 4.4d displays the magnetic properties of random samples as well as the aligned samples, measured // and ⊥ to the alignment direction. The magnetic properties of the by-product removed $Nd_2(Fe,Co)_{14}B$ particles were very sensitive to the magnetic alignment process. M_r almost doubled, from 46.5 emu/g to 89 emu/g, after magnetic alignment. The average misalignment angle φ = 42º for our sample (calculated according to Equation 4.1) is comparable to the corresponding value of aligned $SmCo_5$ nanoparticles prepared by surfactant assisted ball milling [16].

$$\varphi = arctan\left(\frac{2M_r^{\perp}}{M_r^{//}}\right) \tag{4.1}$$

where $M_r^{\perp}$ represents the remanent magnetization measured ⊥ to the c-axis direction, $M_r^{//}$ refers to the remanent magnetization measured // to the c-axis direction [17].

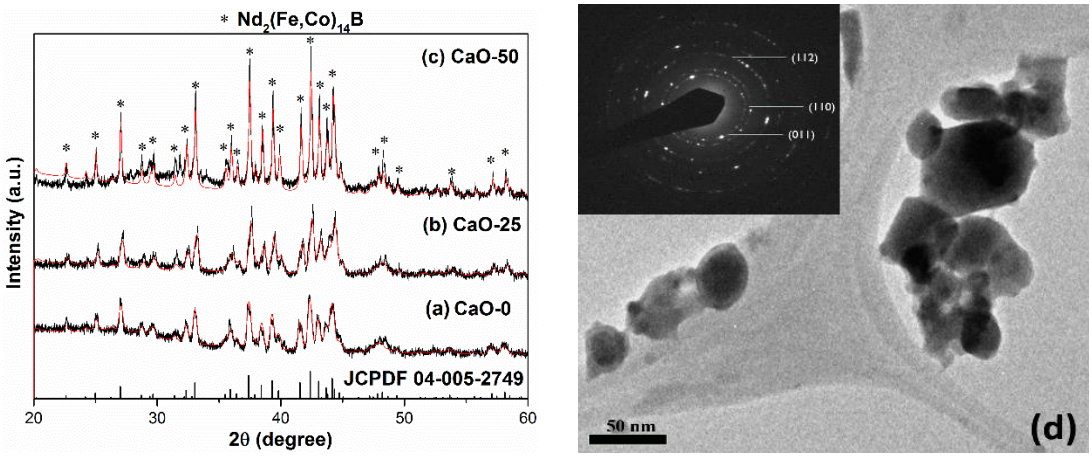

Figure 4.3. X-ray diffraction patterns and Rietveld analysis of by-product removed samples: (a) CaO-0, (b) CaO-25 and (c) CaO-50; (d). TEM bright field image and diffraction pattern of by-product removed CaO-50.

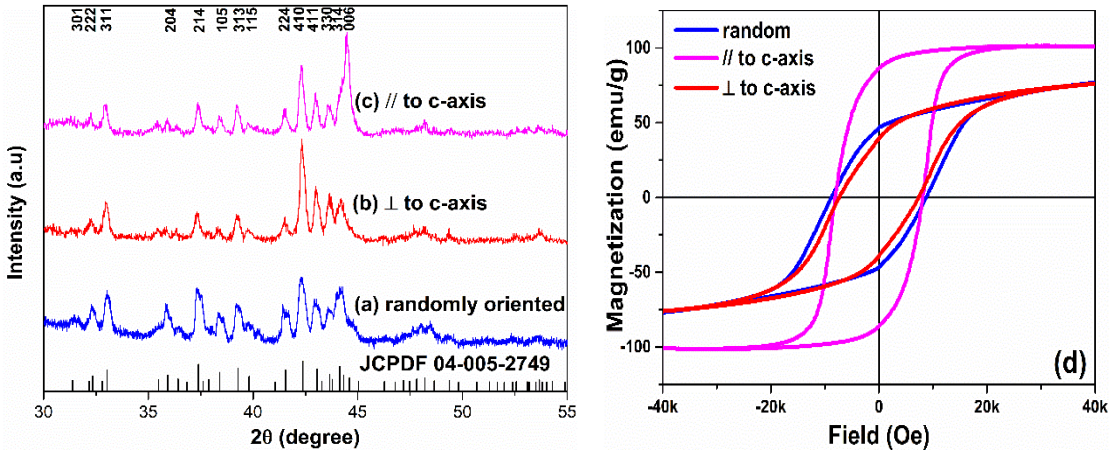

Figure 4.4. X-ray diffraction patterns of by-product removed CaO-50 powders (a) randomly oriented, (b) magnetic-aligned and measured ⊥ to c-axis, (c) magnetic-aligned and measured // to c-axis; (d) magnetic hysteresis loop of by-product removed CaO-50 powder sample, measured in random, // and ⊥ to the alignment direction.

4.2.2 Effect of diluent (CaO) on magnetic properties

The magnetic properties (M-H curve) of as annealed and by-product removed samples over a range of CaO content are shown in Figure 4.5a-b. With increasing CaO content from 0 wt% to 50 wt%, the coercivity of as annealed samples increased from 5.1 kOe to 12.4 kOe.

After by-product removal, all the coercivity dropped and a maximum coercivity of 8.8 kOe was observed for CaO-50.

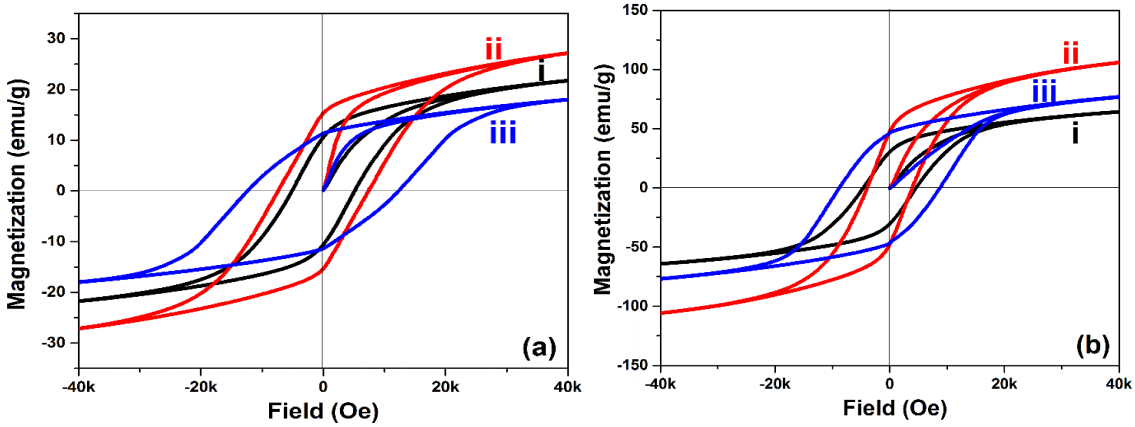

Figure 4.5. Magnetic hysteresis loop of (a) as annealed samples: i - CaO-0, ii - CaO-25, and iii - CaO-50; (b) by-product removed samples: i - CaO-0, ii - CaO-25 and iii - CaO-50.

The average crystal size of the as annealed $Nd_2(Fe, Co)_{14}B$ particles enlarged from 11 nm to 38 nm with increasing CaO content (Table 4.1), together with coercivity enhanced from 5.1 kOe to 12.4 kOe (Figure 4.5a). CaO-50 sample possessed the highest coercivity of 12.4 kOe and an average crystal size of 38 nm. For the first time, the relationship between crystal size and coercivity was revealed in the nanometer range for the mechanochemical processed particles. This trend suggested that the $Nd_2(Fe, Co)_{14}B$ particles with a crystal size larger than 38 nm should be produced to obtain better coercivity values during the mechanochemical process. To confirm whether this relationship continues at larger crystal sizes, further investigations are needed.

Table 4.2 summarizes the magnetic properties for the samples produced in this work and those synthesized by selected chemical methods. The by-product removed CaO-50 sample with coercivity of 8.8 kOe possesses the highest coercivity value among all the Nd-Fe-B nanoparticles processed from the mechanochemical method [2-4]. It is lower than the thermal decomposition processed $Nd_2Fe_{14}B$/ α-Fe samples [18], which may due to the smaller magnetic anisotropy and magnetization of the $Nd_2Co_{14}B$ phase [19]. For the mechanochemical methods, a high coercivity value of 12.2 kOe was obtained for unwashed $Nd_2Fe_{14}B$ samples by Pal et al. [2]. Very recently, several researchers used various by-

product removal method. However, in the study of Gabay et al. and Koylu et al., large degree of coercivity drop was observed after by-product removal process (coercivity values dropped from >12 kOe to 4.6 kOe and 3.3 kOe, respectively) [3, 4]. Till now, our by-product removal method has the least loss in coercivity.

All the Nd-Fe-B particles listed in Table 4.2 possess small crystallite sizes which are less than 100 nm. This is a common advantage in the chemically synthesized Nd-Fe-B particles.

Table 4.2. Magnetic and structure properties of Nd-Fe-B based magnetic powders synthesized from chemical methods.

Method	**Final phase**	**After by-product removal**		**Size (nm)**	**Ref.**
		Hc (Oe)	Ms (emu/g)		
Sol-gel	α-Fe, Nd_2Fe_{17}, $Nd_2Fe_{14}B$	1757	58.6	41	[20]
Auto-combustion	$Nd_2Fe_{14}B$	3280	~80	44.2	[21]
Thermal decomposition	$Nd_2Fe_{14}B$/ α-Fe	12000	41.2	25/10	[18]
Microwave-combustion	$Nd_2Fe_{14}B$	~4000	~95	80	[7]
Sol-gel	$Nd_2Fe_{14}B$	3900	102.3	50	[10]
Mechanochemical	$Nd_2Fe_{14}B$			50-70 *	[2]
Mechanochemical	$Nd_2Fe_{14}B$	4600	~100	10 – 500 *	[3]
Mechanochemical	$Nd_2Fe_{14}B$	3300	~130	158 *	[4]
Mechanochemical	$Nd_2(Fe,Co)_{14}B$	8800	78	40.8	This
Mechanochemical	$Nd_2(Fe,Co)_{14}B$	4000	109	20.8	work
Mechanochemical	$Nd_2(Fe,Co)_{14}B$	4500	66	22.8	

The by-product removal process usually introduces severe coercivity losses [3, 4, 22, 23], coercivity loss of up to 29% was experienced by our samples after by-product removal (Figure 4.5b). Two reasons might be associated with this coercivity loss: 1. Hydrogen diffuses into the $Nd_2(Fe,Co)_{14}B$ structure and promotes the formation of a soft magnetic $Nd_2Fe_{14}BH_x$ phase; 2. Increasing density of anisotropic defects at the particle surface.

Because the reaction between the by-product (CaO) and NH_4Cl is very mild and the product $CaCl_2$ has a high solubility in methanol, almost no heat was generated in our by-product removal process. Hence, there should not be much hydrogen dissolution into our samples. XRD of the by-product removed sample also verifies this statement, no peak shift or $Nd_2Fe_{14}BH_x$ phase formation could be observed (Figure 4.3). Therefore, the coercivity drop mainly results from the increasing number of anisotropic defects at the particle surface or minor particle surface oxidation. For the as synthesized samples, the $Nd_2(Fe,Co)_{14}B$ crystallites are located within a CaO matrix (Figure 4.6). The removal of the CaO matrix easily damages the surface of the $Nd_2(Fe,Co)_{14}B$ particles and introduces more reverse domain nucleation sites. Besides, the by-product removed $Nd_2(Fe,Co)_{14}B$ particles is also easy to get oxidized due to their small sizes. Both these reasons can lead to coercivity loss. In the sintered Nd-Fe-B alloy, the formation of a "wrapped structure", i.e., non-ferromagnetic phases (e.g., Nd-rich layer), wrapped around the $Nd_2Fe_{14}B$ grains, induces drastic enhancement of coercivity [24-26]. Similar to these non-ferromagnetic phases in sintered Nd-Fe-B alloys, the CaO matrix may protect the $Nd_2(Fe,Co)_{14}B$ particles or grain boundaries, improving the coercivity. Removing this CaO matrix eliminates this wrapping structure and can lead to lower coercivity.

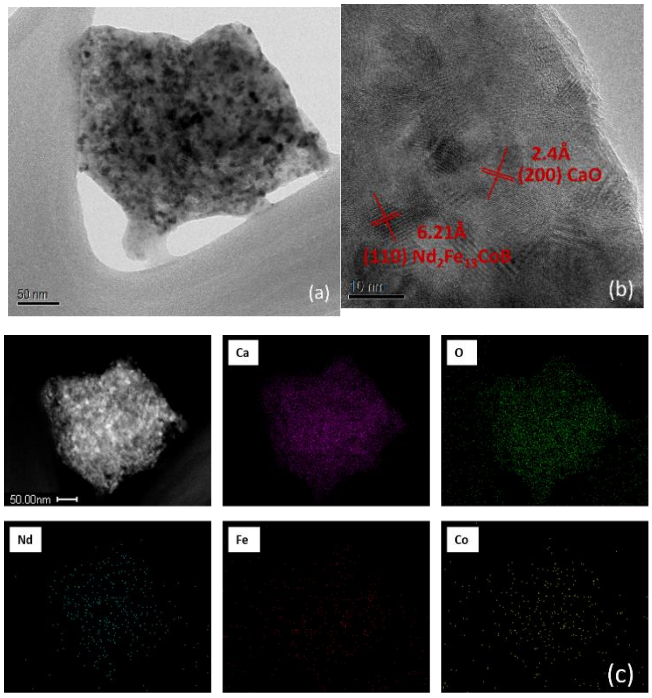

Figure 4.6. (a) TEM bright field image; (b) HRTEM image; and (c) EDS map of as annealed CaO-25.

4.3 Conclusions

High coercivity $Nd_2(Fe,Co)_{14}B$ magnetic powder were processed from the mechanochemical method. The process involves the reduction of Nd_2O_3, Fe_2O_3, CoO and B_2O_3 using Ca, with CaO as dispersant. The highest coercivity was obtained for CaO-50 sample (with additional 50 wt% CaO in the precursors). Prior to by-product removal, this sample possessed a coercivity of 12.4 kOe, after by-product removal, the coercivity reduced to 8.8 kOe. In this work, the influences of CaO content on the $Nd_2(Fe,Co)_{14}B$ formation and the $Nd_2(Fe,Co)_{14}B$ properties were investigated.

CaO behaves as a diluent upon adding into the precursors during the mechanochemical process. It lowered the milling intensity, reduced the chemical reaction rate in ball milling, and led to different $Nd_2(Fe,Co)_{14}B$ formation mechanisms with different CaO content. The average crystallite size of as synthesized $Nd_2(Fe,Co)_{14}B$ increases with increasing CaO amount, along with an enhancement in coercivity. This size-coercivity relationship was

experimentally observed for the first time and it helps to locate the optimum $Nd_2(Fe,Co)_{14}B$ nanoparticle size.

References

[1] S. L. James and T. Friščić. *Chemical Society Reviews*. **2013**, 42, 7494-7496.

[2] A. Pal, A. Gabay, and G. C. Hadjipanayis. *Journal of Alloys and Compounds*. **2012**, 543, 31-33.

[3] A. M. Gabay, X. C. Hu, and G. C. Hadjipanayis. *Journal of Alloys and Compounds*. **2013**, 574, 472-476.

[4] O. Koylu-Alkan, J. Barandiaran, D. Salazar, and G. Hadjipanayis. *AIP Advances*. **2016**, 6, 056027.

[5] D. Restrepo *et al. Chemical Communications*. **2013**, 49, 707-709.

[6] P. Deheri, S. Shukla, and R. Ramanujan. *Journal of Solid State Chemistry*. **2012**, 186, 224-230.

[7] V. Swaminathan, P. K. Deheri, S. D. Bhame, and R. V. Ramanujan. *Nanoscale*. **2013**, 5, 2718-2725.

[8] J. Ren *et al. CrystEngComm*. **2016**, 18, 3481-3487.

[9] S. Contarini, S. Howlett, C. Rizzo, and B. De Angelis. *Applied Surface Science*. **1991**, 51, 177-183.

[10] P. K. Deheri, V. Swaminathan, S. D. Bhame, Z. Liu, and R. V. Ramanujan. *Chemistry of Materials*. **2010**, 22, 6509-6517.

[11] P. Rittmeyer and U. Wietelmann. *Ullmann's Encyclopedia of Industrial Chemistry*. **1989**,

[12] S. Shukla, D. T. Wu, H. Ramanarayan, D. Srolovitz, and R. V. Ramanujan. *Acta Materialia*. **2013**, 61, 3242-3248.

[13] M. Jurczyk, J. Cook, and S. Collocott. *Journal of Alloys and Compounds*. **1995**, 217, 65-68.

[14] M. Mohammadi, A. Ghasemi, and M. Tavoosi. *Journal of Magnetism and Magnetic Materials*. **2016**, 419, 189-197.

[15] G. P. Meisner and E. G. Brewer. *Journal of Applied Physics*. **1992**, 72, 2659-2664.

[16] C.-b. Rong, V. V. Nguyen, and J. P. Liu. *Journal of Applied Physics*. **2010**, 107, 09A717.

[17] W. Fernengel, A. Lehnert, M. Katter, W. Rodewald, and B. Wall. *Journal of Magnetism and Magnetic Materials*. **1996**, 157, 19-20.

[18] L. Yu, C. Yang, and Y. Hou. *Nanoscale*. **2014**, 6, 10638-10642.

[19] C. B. Rong *et al. Journal of Physics D: Applied Physics*. **2012**, 46, 1-5.

[20] H. Rahimi, A. Ghasemi, R. Mozaffarinia, and M. Tavoosi. *Journal of Superconductivity and Novel Magnetism*. **2016**, 29, 2041-2051.

[21] H. X. Ma, C. W. Kim, D. S. Kim, J. H. Jeong, I. H. Kim, and Y. S. Kang. *Nanoscale*. **2015**, 7, 8016-8022.

[22] A. Gabay, X. Hu, and G. Hadjipanayis. *Journal of Magnetism and Magnetic Materials*. **2014**, 368, 75-81.

[23] A. Gabay and G. Hadjipanayis. *Journal of Physics D: Applied Physics*. **2014**, 47, 182001.

[24] B. Straumal, A. Mazilkin, S. Protasova, G. Schütz, A. Straumal, and B. Baretzky. *Journal of Materials Engineering and Performance*. **2016**, 25, 3303-3309.

[25] N. Watanabe, M. Itakura, and M. Nishida. *Journal of Alloys and Compounds*. **2013**, 557, 1-4.

[26] N. Watanabe, H. Umemoto, M. Ishimaru, M. Itakura, M. Nishida, and K. Machida. *Journal of Microscopy*. **2009**, 236, 104-108.

Chapter 5 *

Mechanism and Kinetic Study of the Mechanochemical Synthesis of $Nd_2(Fe,Co)_{14}B$ Hard Magnetic Nanoparticles

The mechanochemical method is a "green", cost-effective and low temperature technique to process $Nd_2(Fe,Co)_{14}B$ magnetic nanoparticles. However, to monitor, optimize and control this process is challenging. Therefore, a kinetic study was conducted on the mechanochemical process to synthesize $Nd_2(Fe,Co)_{14}B$ hard magnetic nanoparticles. The time-dependent CaO content during milling acted as an indicator to monitor the milling process. Three milling stages were observed: (i) precursor oxides amorphization, (ii) precursor oxides reduction and (iii) steady-state. A model was proposed to predict the milling kinetics and the predictions were compared to experiment. A maximum milling efficiency was obtained at a ball milling speed of 550 rpm. High coercivity of up to 9.4 kOe was achieved by the synthesized $Nd_2(Fe,Co)_{14}B$ particles. The coercivity values increased with increasing lattice parameter and crystallite size.

*The content of this section is published substantially as reference:

1. Y. Zhong, V. Chaudhary, X. Tan, H. Parmar and R. V. Ramanujan. Mechanochemical synthesis of high coercivity $Nd_2(Fe, Co)_{14}B$ magnetic particles. *Nanoscale* 9, 18651-18660 (2017).

2. Y. Zhong, V. Chaudhary, X. Tan, H. Parmar and R. V. Ramanujan. Kinetic study of the mechanochemical synthesis of $Nd_2(Fe, Co)_{14}B$ hard magnetic nanoparticles. *Journal of Alloys and Compounds* **747**, 755-763 (2018).

5.1 Introduction

Recently, exciting results have been obtained by the "green" mechanochemical synthesis method. During the processing, the application of mechanical forces occurs simultaneously with chemical reaction. This method has been used in a wide range of areas, ranging from new areas including metal-organic frameworks, supramolecular chemistry and pharmaceutical co-crystals to traditional areas such as catalysis, organic and inorganic chemical synthesis [1-4]. Different kinds of products, such as oxides, intermetallic compounds and metal hybrids have been processed. Hard magnetic nanoparticles with relatively good magnetic properties, including Sm_2Co_{17}, $Nd_2Fe_{14}B$ and $LaCo_5$, have also been synthesized via this "green" and low-cost method [5-8]. In this process, no expensive elemental metal precursors are needed, only metal oxide precursors, diluent and reducing agent are needed. Hence, the cost can be significantly reduced. Besides, this process is easily to scale up due to the use of high energy ball millers. Therefore, it is a cost-effective and "green" approach to produce Nd-Fe-B particles through the mechanochemical process.

Only a handful investigations were made to synthesis Nd-Fe-B based permanent magnets through the mechanochemical approach [6, 9-11]. The process parameters during milling have not been optimized and the kinetics of reactions during milling have not been studied. The main obstacle of these studies is the difficulty to monitor the phase transformation of samples inside the milling bowl. Recently, kinetic studies during the mechanochemical milling have been facilitated by some semi-situ and in-situ monitoring techniques [12-16]. During the mechanochemical milling process, the enclosed reaction environment within the milling bowl enables clearly identified process parameters, such as milling speed and milling time, to be controlled and optimized [12]. Therefore, the mechanochemical process can be monitored and optimized.

The mechanisms and kinetics of the reduction reactions taking place in the milling process were investigated in this study by both experimental and modelling methods. Based on energy transfer concepts, a kinetic model was proposed to predict reaction kinetics at various milling speeds and to calculate the respective milling efficiency [17-20]. The

kinetic model was compared with the experimental data. An analogical method was utilized to predict the reaction kinetics in the work of Liu et al., where the disproportionation of a $Nd_{12}Fe_{82}B_6$ alloy took place via mechanical milling [13]. Deeper understanding and better process parameter control of the mechanochemical process was obtained from this work.

5.2 Results and Discussion

5.2.1 Time-dependent phase transition process

The application of mechanical energy during the mechanochemical process led to the occurrence of chemical reactions, which introduced phase transition. An investigation was performed to study the time-dependent phase transitions during milling to understand the process better.

Figure 5.1 and Figure 5.2 show the XRD and Rietveld refinement study of CaO-0 (sample set with no additional CaO added in precursors) milled for different milling durations. To measure the amorphous phase content, an internal standard of 5wt% crystalline CeO_2 was placed in each sample. In the first 20 min of milling (Figure 5.1 a-c), only the diffraction peaks for the precursor oxides, i.e., Fe_2O_3, Nd_2O_3 and CoO, were present. After that, a sharp α-Fe peak at 45° appeared concurrently with CaO diffraction peaks. Additional milling after 20 min does not induce further phase transitions. To analysis the structural change after 20 min milling time, the Rietveld refinement was employed.

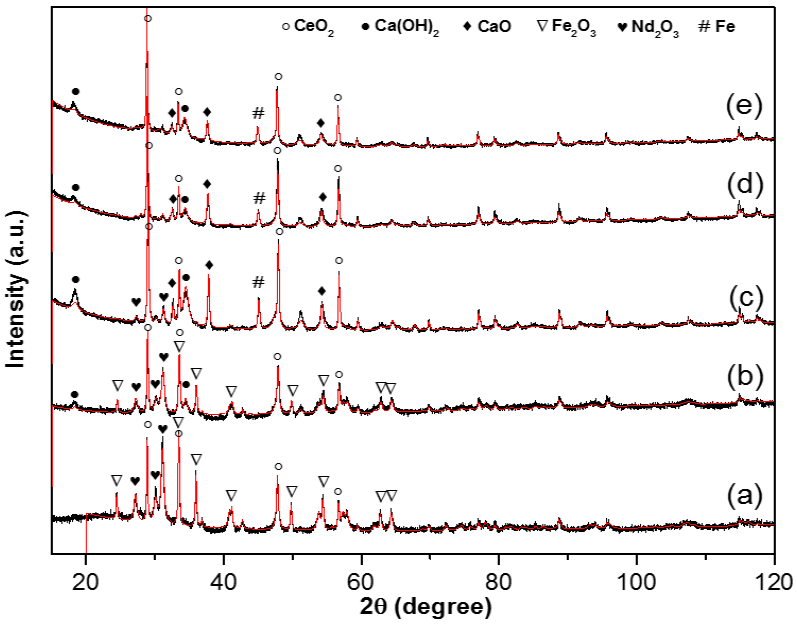

Figure 5.1. X-ray diffraction patterns and Rietveld refinement of as milled CaO-0 samples at different milling durations: (a) 5 min; (b) 10 min; (c) 20 min; (d) 30 min; (d) 50 min. α-Fe and CaO diffraction peaks was present after 20 min milling.

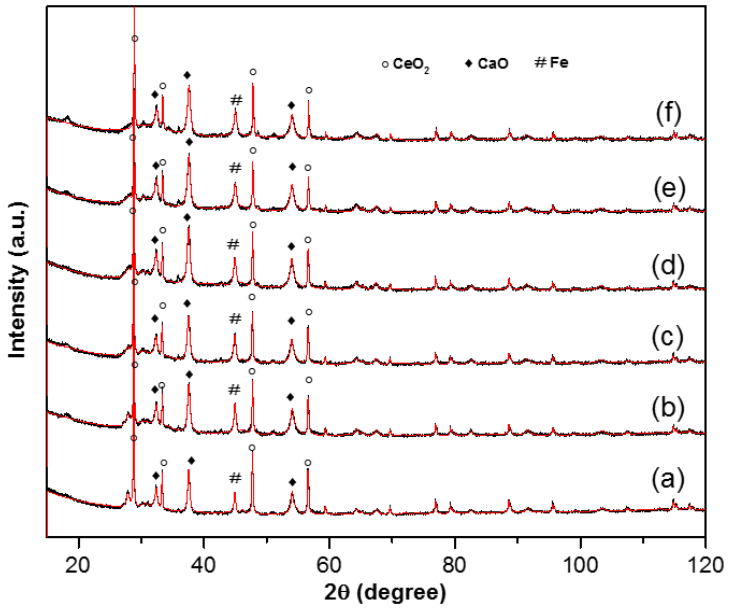

Figure 5.2. X-ray diffraction patterns and Rietveld refinement of as milled CaO-0 samples at different milling durations: (a) 1 h; (b) 2 h; (c) 3 h; (d) 4 h; (e) 5 h; (f) 6 h. No additional phase transition can be observed, and structural changes was analyzed by Rietveld refinement.

Figure 5.3 and Figure 5.4 illustrates the phase evolution with respect to milling time and the mass percentage of each phase at different milling times calculated through the Rietveld

refinement. Figure 5.3 clearly shows that after 30 min milling, the precursor oxides vanished. Instead, α-Fe phase, CaO phase and an amorphous phase appeared (Figure 5.3). The amorphous phase content drastically increased in the first 30 min of milling, then steadily decreased, followed by increasing CaO formation and formation of the α-Fe phase. After milling of 300 min, the mass fraction of each phase stabilized and steady state was observed at milling time of 300 – 360 min.

Hence, there is three stages during the mechanochemical milling: in the first 30 min milling, severe amorphization of precursor oxides was induced, which quickly decreased the peak intensity of the precursor oxides and simultaneously led to a rapid formation of amorphous phase. The main effect of milling during this time was to decrease particle size and induce intimate contact between the particles. After 30min milling, in the second milling stage, the milling energy drove the chemical reduction reactions. Therefore, the formation of CaO and α-Fe phase was observed, and the amorphous phase reduction was induced. In the last milling stage, at milling time of 300-360 min, a steady state was achieved. In the second milling stage, the steady increase of CaO content with milling time indicated a steady reduction of the precursor oxides. Hence, continuous input of milling energy is required to complete the reduction reactions. Therefore, this mechanochemical milling is not a self-propagating process.

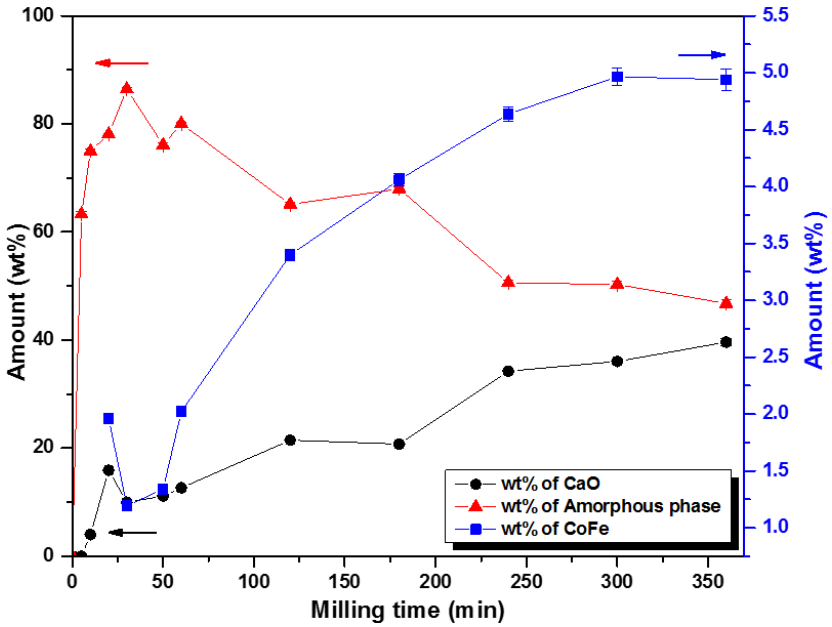

Figure 5.3. Phase evolution with respect to milling time in as milled CaO-0 sample. (Black line - CaO, blue line - α-Fe and red line - amorphous phase)

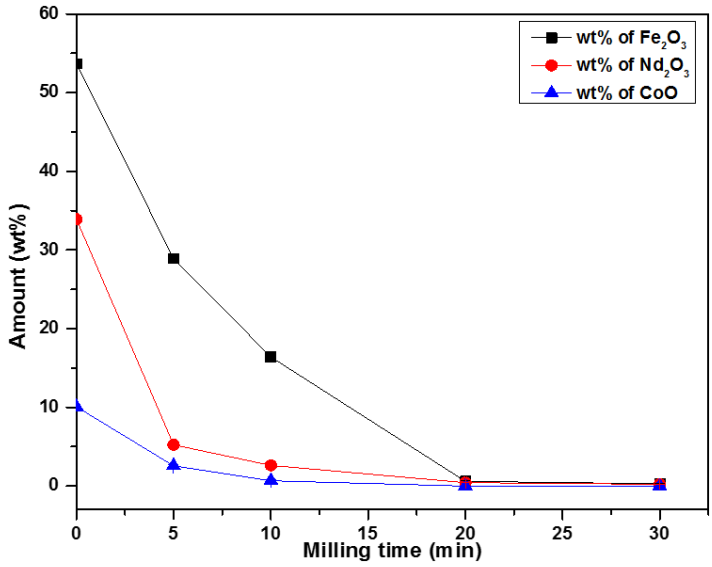

Figure 5.4. Phase evolution with respect to milling time in as milled CaO-0 sample (for the precursor oxides).

Sharp diffraction peaks were observed for the α-Fe phase at its initial appearance within the first 20 min of milling time (Figure 5.1c). However, additional milling led to decrease of the FWHM for the α-Fe diffraction peaks. The formation of sharp α-Fe diffraction peaks within the first 20 min indicates the start of the reduction reactions during milling. The

broadening of the α-Fe diffraction peaks indicates that the crystal size of α-Fe decreased with milling attrition. To calculate the α-Fe average crystallite size, Rietveld analysis was conducted. It was found that within the first 50 min milling the α-Fe crystallite size fluctuated, and after 50 min milling, it decreased exponentially with respect to milling time. $D = A * \exp(-t/B) + C$ can be used to describe this decrease, where D is the average crystallite size, t represents the milling time, and constants A = 26.9, B = 94.4 min, C = 13.1 nm (Figure 5.5).

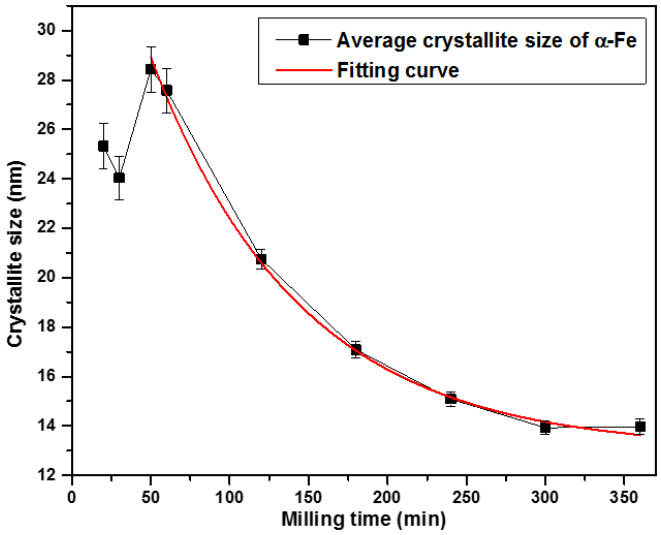

Figure 5.5. α-Fe average crystallite size evolution with respect to milling time and an exponential fitting for sizes after 50 min milling.

In mechanical milling of Nd-Fe-B melt spun ribbons, the milling induced structural changes are results from a competition between two processes: 1. free volume and anti-free volume (FV-AFV) induced diffusion, which promotes growth of crystal; 2. impact-induced crystal attrition which breaks down large crystals [21-23].

In analogy to mechanical milling, the driving force for structural and composition changes in the mechanochemical process could also be attributed to the competition between these two processes: 1. free volume and anti-free volume (FV-AFV) induced diffusion, which induced the reduction reaction and promoted the nucleation and growth of the α-Fe crystallites; 2. impact-induced crystal attrition which resulted in smaller crystal size. At early milling stage (within the first 50 min), the formation of α-Fe crystallite was just

initiated, hence the crystal size fluctuated. With further increasing of milling time, the impact induced crystal attrition override the crystal growth effect, resulted to the exponential decrease of crystal size. After 300 min milling, these two processes came to a dynamic equilibrium, leading to the presence of a steady state crystallite size. The phase evolution equilibrium occurred between 300 min – 360 min, which coincided with this dynamic equilibrium in crystallite size. Therefore, for this mechanochemical milling process, 6 h is an optimum milling time.

To further understand the process over a wide range of milling speeds, mechanochemical milling was performed at different milling speeds: 450, 500, 550 and 600 rpm. Experimental and theoretical studies were performed to understand the relationship between milling speed w_p, milling efficiency λ and milling time t.

The XRD and Rietveld refinement analysis of as milled samples processed at 450, 500, 550 and 600 rpm for various milling durations are shown in Figure 5.6. A known amount of internal spike (crystalline Si or CeO_2) was added to each sample for quantitative analyses to calculate the mass percentage of each phase. For each Rietveld refinement analysis, the goodness of fit (GOF) was less than 2. The errors in the values of the mass fraction of each phase was calculated by TOPAS 4.1 software, and they were all less than 0.5%. The α-Fe and CaO phases formed simultaneously at all milling speeds within the milling time of 1-2 h (Figure 5.6). Further milling increased the intensity of the CaO diffraction peaks, demonstrating the presence of larger CaO content.

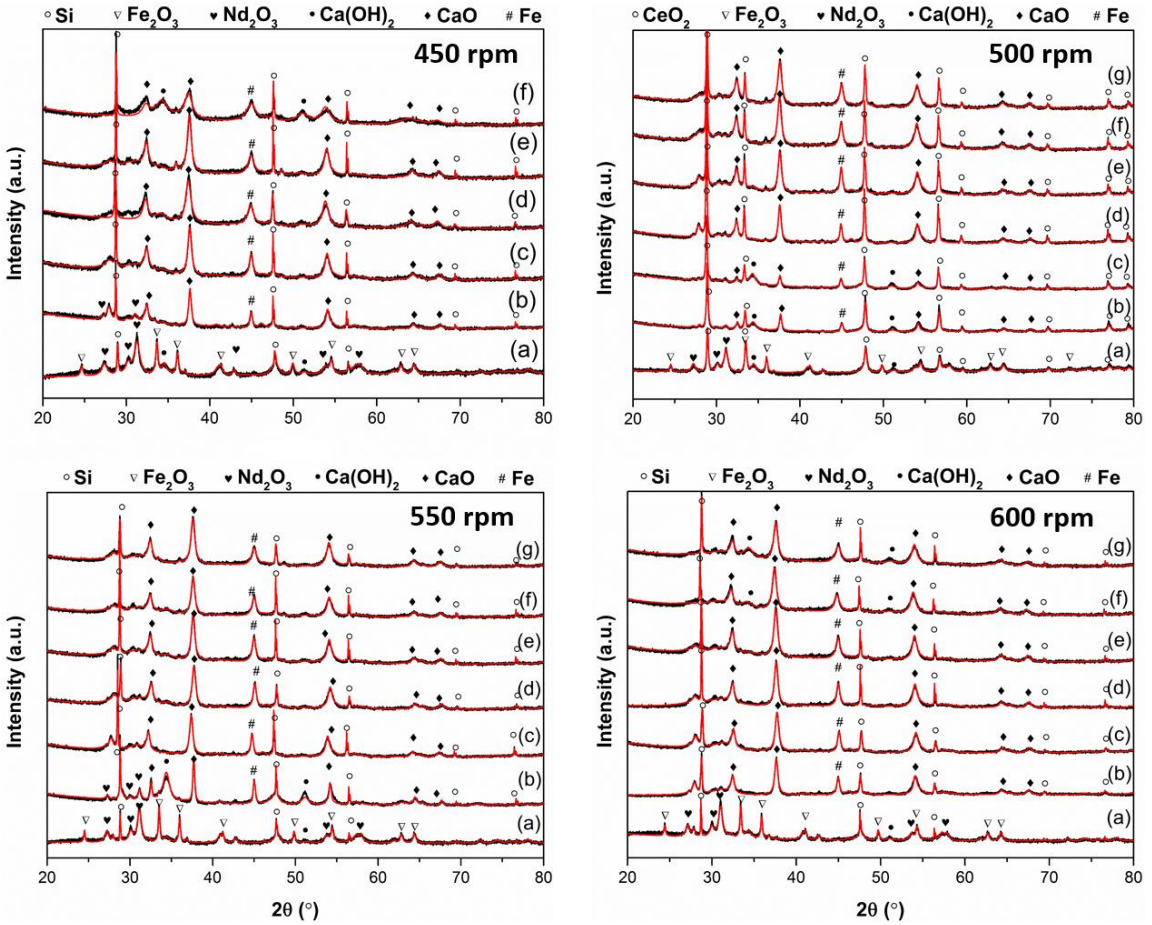

Figure 5.6. XRD and Rietveld refinement for precursors milled at various milling speeds. At 450 rpm for (a) 1h, (b) 2h, (c) 5h, (d) 8h, (e) 10h, and (f) 13 h; at 500 rpm for (a) 10min, (b) 30min, (c) 50min, (d) 1h, (e) 2h, (f) 4 h and (g) 5h; at 550 rpm for (a) 5min, (b) 15min, (c) 1h, (d) 2h, (e) 3h, (f) 4 h and (g) 5h; at 600 rpm for (a) 5min, (b) 30min, (c) 1h, (d) 2h, (e) 3h, (f) 4 h and (g) 5h.

The phase transformation evolution and the mass percentage of each phases with respect to milling time at different milling speeds is present in Figure 5.7. A three-stage milling process can be observed in all cases: (i). amorphization of crystalline Nd_2O_3, Fe_2O_3, CoO and B_2O_3 phases; (ii). formation and steady increase of the CaO and α-Fe content, together with an amorphous phase content decrease. In this stage, the CaO content increased due to the reduction of precursor oxides. The milling induced mechanical energy introduced the reduction of all precursor oxides, which led to decrease in amorphous phase content and formation of α-Fe phase. (iii). Steady state, where there was virtually no change in the content of each phase.

The nanocrystalline α-Fe phase formation was also observed in other non-equilibrium processing of Nd-Fe-B based alloys, such as electron irradiation and mechanical milling. At steady state of these two processes, both the crystalline α-Fe phase and an Nd-rich amorphous phase are observed [23-26]. This phenomenon can be explained thermodynamically. Through calculation based on the Miedema model, the enthalpy of formation for the mixture of a α-Fe phase and an amorphous phase is much less than that of the ternary Nd-Fe-B alloy system [27, 28], therefore the formation of the mixture is thermodynamically more favorable.

The reaction which occurred during mechanochemical milling process is the reduction of precursor oxides by Ca granules. The CaO formed as a reaction product of this reduction reaction. Hence, the change in CaO content can be treated as the progress indicator for this reduction reaction. The steady increase of CaO content suggest that milling energy is continuously required for the progress of the reduction reaction. Thus, the milling induced mechanical energy is comparable to the effect of the thermal energy in a thermally introduced reaction and the change of CaO content can be used to track this progress.

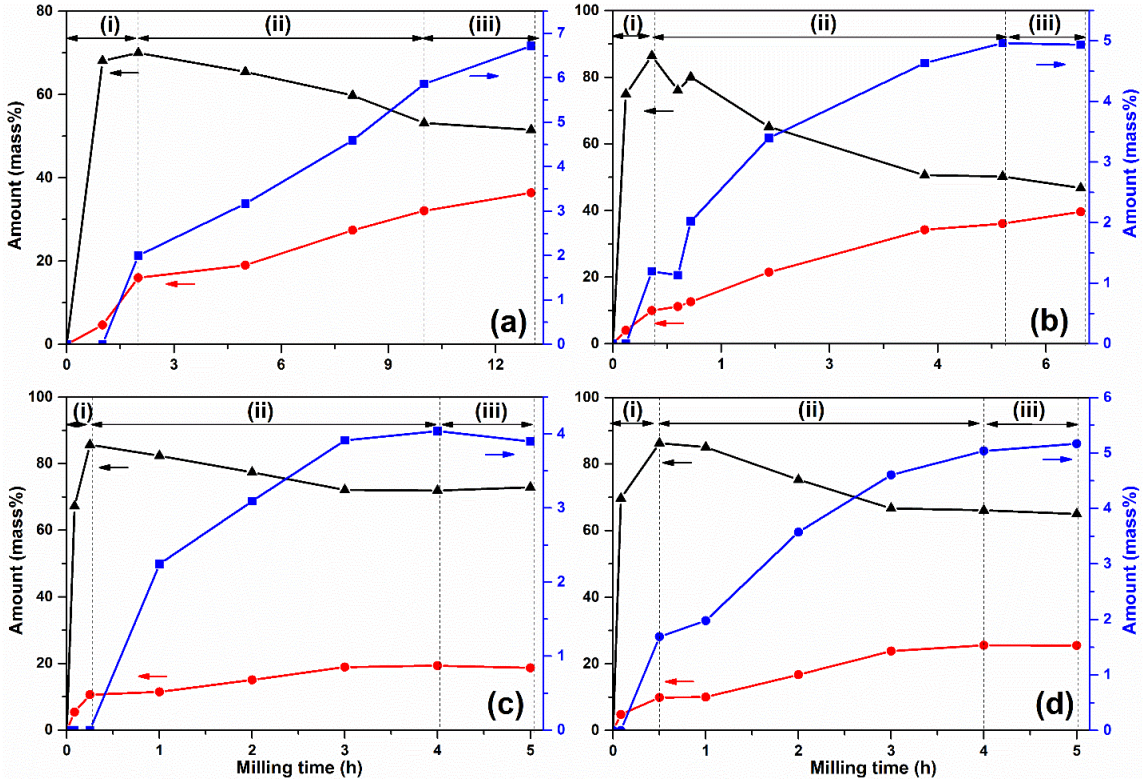

Figure 5.7. Mass% of each phase at different milling durations at various milling speeds: (a) 450, (b) 500, (c) 550 and (d) 600 rpm. The amorphous phase is present by the black plots (left axis), the CaO phase is indicated by red plot (left axis), and the α-Fe phase is present by blue plot (right axis).

5.2.2 Kinetic model

A kinetic model was proposed to monitor the mechanochemical milling process. During the milling process, the milling induced energy (E_0) is assumed to be utilized in three ways: 1. to physically reduce the particle size (E_s); 2. to chemically induce reduction reactions (E_e); 3. to dissipate as heat or sound. E_e indicates the energy that is required to induce the chemical reactions during milling, E_s represents the energy that is required to induce the physical changes during milling, i.e., the energy required to reduce the particle size of the milled species and increase their surface area. The rest of the milling energy is not effectively utilized in the mechanochemical process, instead, it is dissipated as sound and

heat during milling. The fraction of the effectively utilized milling energy is termed as the milling efficiency, and represents by λ. Their relationship is shown in Equation 5.1:

$$\lambda E_0 = E_s + E_e \quad (5.1)$$

By assuming that the collision events during milling transfers the mechanical energy, two parameters were put forward by Magini et al. [17-20] to quantify the milling induced mechanical energy (E_0): the kinetic energy transferred per collision to the powder by a ball (ΔE), and total collision frequency (v_t). E_0 can be calculated by Equation 5.2:

$$E_0 = \varphi_b \Delta E v_t \quad (5.2)$$

where φ_b is a filling ratio related constant. As the filling ratio in our experiments is less than 1/3, it is appraised to be 1[13].

Equation 5.3 estimates the energy transferred to the powder per collision event (ΔE) per milling ball,

$$\Delta E = \frac{1}{2} K_a {K_b}^2 m_b {\omega_p}^2 {R_p}^2 \quad (5.3)$$

where K_a= 1 for perfect inelastic collisions and K_a= 0 for perfect elastic collisions. K_b is a geometrical factor, which depends on the ball mill set-up. For planetary ball mills, it is typically estimated to 0.98 [20]. m_b indicates the mass of the milling ball; R_p represents the milling disk radius; ω_p represents the planetary mill disk rotation speed. In this study, m_b = 7 g and R_p =7 mm.

Equation 5.4 expresses the total energy transferred to the powder per unit time by collision events (v_t):

$$v_t = vN_b = k(\omega_p - \omega_v)N_b/2\pi \quad (5.4)$$

where v refers to the collision frequency during milling for one ball, N_b represents the number of balls used during milling, k refers to a ball diameter related constant. k is estimated to 1.624, as the balls with 10 mm diameter were used in this study [19]. ω_v represents the milling vial rotation speed. For the Fritch Pulverisette-7 planetary ball mill, the transmission ratio ω_p/ω_v is 1:-2. As the vial rotates in opposite direction to the disk, a negative sign is used in the transmission ratio.

It has been widely accepted that a proportionality constant (β) and the increase of surface area (ΔS) can be used to estimate the energy required to form new surfaces (E_s) [29-31]. Equation 5.5 shows this relationship, where γ represents the specific surface energy. β is often estimated to be of the order of 10^2 in literature [31], hence we assume β = 500 in this study. As majority of the precursor oxides is Fe_2O_3, we assume most of the as milled particles are Fe particles, which have a specific energy of ~ 2.5 J/m^2 [29, 30, 32].

$$E_s = \beta\gamma\Delta S \tag{5.5}$$

The surface area increase (ΔS) can be expressed by Equation 5.6 [31],

$$\Delta S = f_s {D_{in}}^2 (D_{in} - D)/D \tag{5.6}$$

where f_s is the shape-related surface area factor and $f_s = \pi$ for spherical particles, D_{in} is the initial average particle size, D is the average particle size at milling time of t.

Equation 5.7 is employed to calculate the average particle size *D* at ball milling time of *t*, and C_1 is a constant:

$$D = C_1 t^{-1} \tag{5.7}$$

From Equations 5.5-5.7, the energy required to create new surface in the ball milling process (E_s) can be expressed in Equation 5.8.

$$E_s = C_1\beta\gamma f_s {D_{in}}^3 t - \beta\gamma f_s {D_{in}}^2 \tag{5.8}$$

Therefore, the time-dependent energy utilized for the chemical reduction occurred in milling (E_e) can be expressed as Equation 5.9. Equation 5.9 establishes based on two assumptions: (i). the mechanical energy input by ball milling has a similar effect as thermal energy; (ii). the energy required to promote chemical reactions during milling only originates from the milling induced mechanical energy.

$$E_e = \lambda E_0 - E_s = \lambda\varphi_b \Delta E v_t - \beta\gamma\Delta S \tag{5.9}$$

At milling time *t*, assuming E_e can be absorbed by the powders sandwiched between two colliding balls, the mass increment of the chemically transformed product (dm) during time increment (dt) can be expressed as:

$$dm = (1 - y)\frac{\lambda\varphi_b \Delta E v_t - \beta\gamma\Delta S}{E_a} dt \tag{5.10}$$

where the reacted fraction of CaO at time *t* is represented by *y*, i.e., the ratio between time-dependent content of CaO/CaO content at steady-state), E_a represents the overall activation energy of the chemical reaction occurred in milling [13].

By denoting m_0 as the content of CaO formed at steady-state, the increment of reaction fraction dy, for an increment of time dt, at milling time *t*, can be shown in Equation 5.11:

$$dy = \frac{dm}{m_0} \tag{5.11}$$

Substituting Equation 5.1-5.9 and 5.11 into Equation 5.10, the time-dependent CaO reaction fraction, *y*, can be obtained:

$$\begin{aligned} y &= 1 - \exp\left(-\frac{(\lambda E_0 - E_s)t}{E_a m_0} + C_2\right) \\ &= 1 - \exp\left(\frac{C_1 \beta \gamma f_s {D_{in}}^3}{2 m_0 E_a} t^2 - \frac{\frac{3}{2}\lambda k {k_b}^2 m_b {R_p}^2 N_b {w_p}^3 + \beta \gamma f_s {D_{in}}^2}{m_0 E_a} t + C_2\right) \end{aligned} \tag{5.12}$$

where C_1 and C_2 are constants.

Both E_a and m_0 are constants for a given reaction, only the milling speed (ω_p) and the milling efficiency (λ) are related to the time taken (t) for the reaction to reach steady state $(y = 1)$. Therefore, for a specific milling speed (w_p), by fitting the experimentally obtained *y* and *t* to Equation 5.12, the milling efficiency (λ) can be calculated.

To simplify the equation for later studies, we assume $A = \frac{C \beta \gamma f_s {D_{in}}^3}{2 m_0 E_a}$; $B = \frac{\frac{3}{2}\lambda k {k_b}^2 m_b {R_p}^2 N_b {w_p}^3 + \beta \gamma f_s {D_{in}}^2}{m_0 E_a}$, Equation 5.12 can be simplified as:

$$y = 1 - \exp(At^2 - Bt + C_2) \tag{5.13}$$

5.2.3 Milling efficiency calculation

During isochronal DSC measurement, when a chemical reaction or phase transition occurs, a peak (T_p) will appear in the measured profile. At different heating rates, the position of reaction temperature peak (T_p) will shift in the isochronal DSC thermograms. According

to the Kissinger model, this peak position shift can be used to calculate the activation energy for this specific reaction (E_a) [33, 34]. The relationship between heating rate b and peak position (T_p) can be expressed as Equation 5.14.

$$ln\frac{b}{{T_p}^2} = -\frac{E_a}{RT_p} + C_2 \quad (5.14)$$

To calculate the overall activation energy E_a needed for the milling-induced reduction reaction, the isochronal DSC thermograms were measured at heating rates of 5, 10, 15, 20 K/min from 25 °C to 900 °C for the mixture of thin Ca flakes and precursor oxides (Figure 5.8a). It was found in a previous study that the majority of the precursor oxides reduction took place in milling process for this reaction [11]. Therefore, E_a required in the mechanochemical milling process can be assumed to be comparable to E_a needed in reduction-diffusion based processes, for example, the microwave-assisted combustion process. During the investigation of the reduction mechanism on the CaH_2 reduced Nd-Fe-B mixed oxide powders [33, 35, 36], it was found that Fe_2O_3 and B_2O_3 reduction took place at temperature between 300 - 350 °C, $Nd_2Fe_{14}B$ phase formed at temperature of~ 692-740 °C and melting of metallic calcium occurred at ~ 840 °C. Hence, the DSC measurements was performed at 25 °C - 900 °C. An exothermic peak was observed at ~ 850 °C, indicating the occurrence of oxides reduction. Figure 5.8b presents the plot for $\ln(\frac{b}{{T_p}^2})$ vs $\frac{1000}{T_p}$ for the reaction took placed at ~ 850 °C. The activation energy E_a for the reaction was then determined.

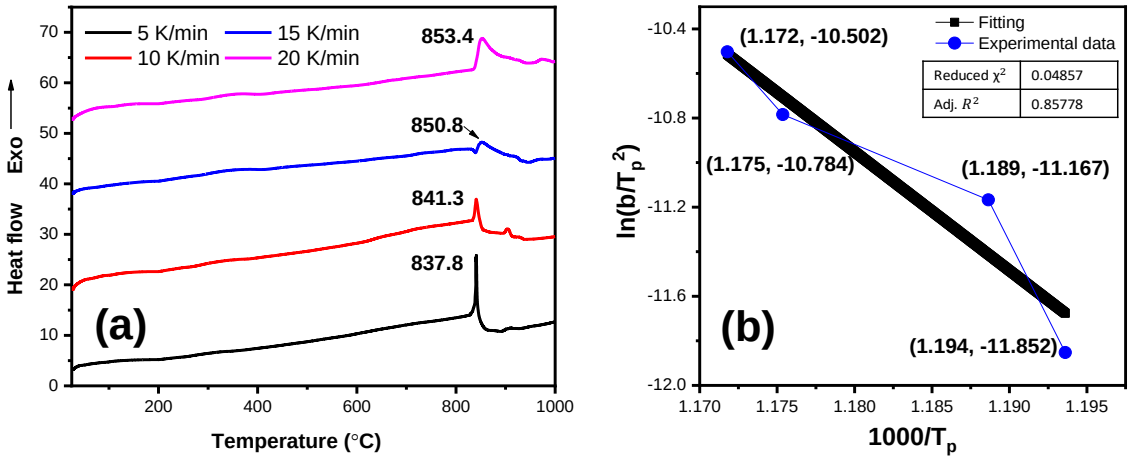

Figure 5.8. (a). Isochronal diffrential scanning calorimetry measurements of the reduction-diffusion process of Ca flakes and precursor oxides at different heating rates: 5 K/min, 10 K/min, 15 K/min and 20 K/min; (b). $\frac{b}{T_p{}^2}$ vs $\frac{1000}{T_p}$ plot for obtaining E_a for reactions at ~850ºC.

For the reduction of precursor oxides, the calculated activation energy (E_a) is 443 kJ/mol. The activation energy E_a, along with k, k_a, k_b, m_b, R_p and N_b are considered as experimental constants in Equation 5.12 during fitting. In the microwave-assisted combustion process to synthesis $Nd_2(Fe,Co)_{14}B$, E_a for Fe and Co reduction and NdH_2 and $Nd_2Fe_{14}B$ formation is 146 kJ/mol and 335 kJ/mol, respectively[35]. Therefore, the E_a for the overall microwave-assisted reduction diffusion process is 481 kJ/mol, which is very similar to what we calculated in the mechanochemical process.

In the theoretical model, the steady-state condition was assumed to be the stage when the content of reduction products (for example, CaO) levels off. y represents the CaO mass percentage at milling time of t, y values obtained experimentally were compared and fit in the theoretical model (Equation 5.12), as shown in Figure 5.9. The values for A and B were calculated during fitting of the experimental data to Equation 5.12. It can be seen from Equation 5.12 that the milling speed ω_p and the milling efficiency λ are only related to the value of B. Hence, we only considered the B values during the calculation. Except milling speed w_p, milling efficiency λ, and the initial particle size D_{in}, all other values in B can be either obtained from literature or are experimental constants. Here D_{in} represents the initial average particle size, which corresponds to the average particle size of the precursor oxides. It is estimated to be ~ 100 μm. At a known milling speed ω_p, by fitting the experimentally

obtained *y* values into Equation 5.12 and substituting all the constants into the obtained B values, the milling efficiency λ at this milling speed can be subsequently calculated (Table 5.1).

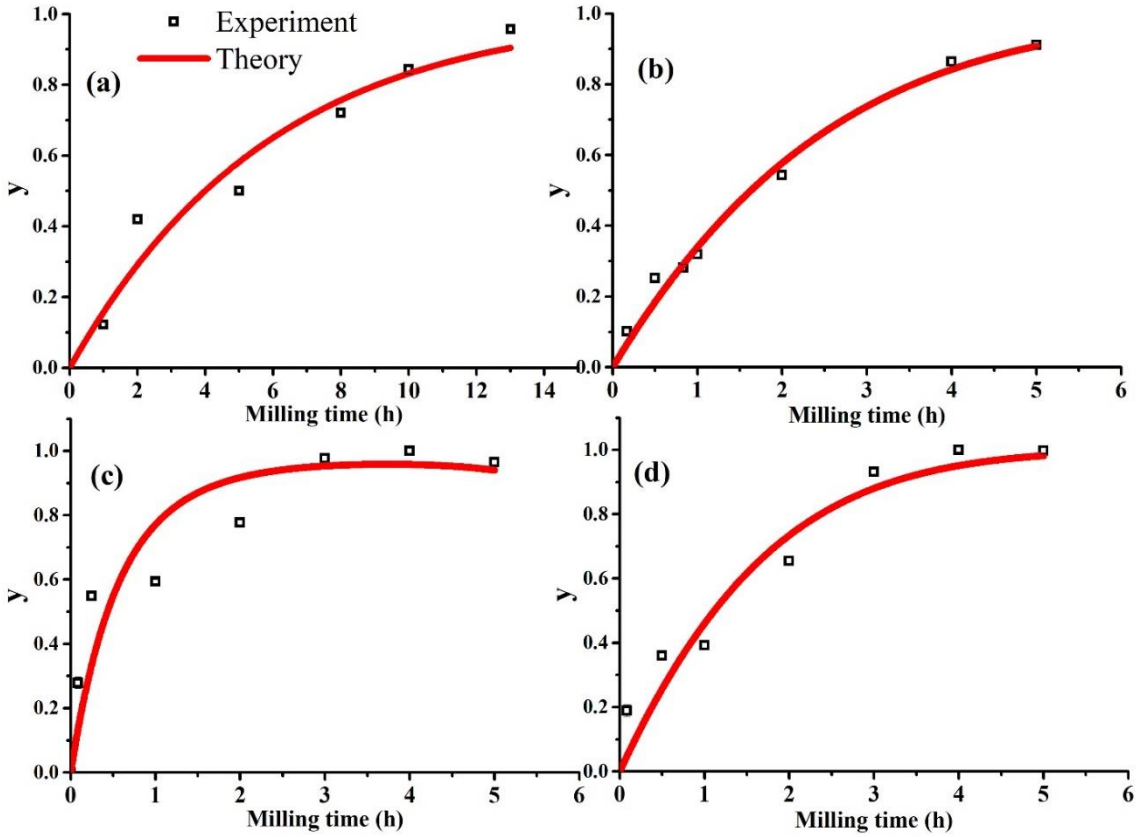

Figure 5.9. Comparison of the experimentally obtained mass fraction of CaO (*y*) with respect to milling time (*t*) and the proposed theoretical model at various milling speeds: (a) 450 rpm, (b) 500 rpm, (c) 550 rpm, (d) 600 rpm.

Table 5.1. The experimental constants and theoretically calculated parameters in the kinetic study of mechanochemical synthesis of $Nd_2(Fe,Co)_{14}B$ particles at different ball milling speeds.

Milling speed (rpm)	w_p * (rad/s)	m_0 (g)	B	λ
450	41.7	1.9	4.74×10^{-5}	6.86×10^{-4}
500	53.3	1.9	1.11×10^{-4}	7.69×10^{-4}
550	57.6	1.0	4.73×10^{-4}	1.37×10^{-3}
600	62.8	1.3	1.59×10^{-4}	4.59×10^{-4}

* w_p is the rotation speed of the planetary disk in rad/s. m_0 is the mass of CaO formed at steady state.

For this mechanochemical process, the calculated value of milling efficiency (λ) is between 4.59×10^{-4} to 1.37×10^{-3}. For a hydrogenation-disproportionation-desorption-recombination (HDDR) assisted by ball milling process, a similar model was employed to calculate the milling efficiency as well. In that model, the change of the H_2 pressure with respect to milling time was selected as a process indicator and milling efficiencies lies in between from 4.46×10^{-4} to 1.33×10^{-3} in their calculation [13]. It can be seen that very similar milling efficiencies was obtained in these two different ball milling processes. In the mechanochemical process, between the milling speeds from 450 rpm to 600 rpm, the respective milling efficiency λ first increased from 6.86×10^{-4} to 1.37×10^{-3} from 450 rpm to 550 rpm, then it decreased to 4.59×10^{-4} with milling speed increasing to 600 rpm. With larger milling speed, less time was needed to achieve steady-state condition. However, the milling efficiency does not keep increasing with increasing milling speed. It could be that larger milling speed does increase the amount of output energy. However, the output mechanical energy cannot be fully utilized to induce reactions. With increasing milling speed, more energy was dissipated as sound or heat in milling, resulted in lower energy utilization efficiency. Therefore, an optimum ball milling speed is needed to utilize energy more effectively. In this mechanochemical process, 550 rpm is the optimum milling speed to reach a highest milling efficiency.

5.2.4 Structure and Magnetic Properties

As mentioned in Chapter 4, the as milled particles does not contain the desired tetragonal $Nd_2(Fe,Co)_{14}B$ particles. Further heat treatment and by-product removal is needed to produce single phase $Nd_2(Fe,Co)_{14}B$ particles. In this study, the steady-state powders at different milling speeds were collected and compacted for subsequent heat treatment and by-product removal process to produce $Nd_2(Fe,Co)_{14}B$ particles. Figure 5.10 shows the XRD and Rietveld refinement of the by-product removed samples processed at various ball milling speeds. Although the tetragonal $Nd_2(Fe,Co)_{14}B$ phase was observed at all milling speeds, the diffraction peaks for the sample milled at 550 rpm are shifted by ~0.3° to lower 2θ positions (Figure 5.10c) when comparing to other samples. This can be due to the introduction of hydrogen induced during the by-product removal process. As explained earlier, the diffusion of hydrogen into the tetragonal $Nd_2Fe_{14}B$ structure can lead to the formation of soft $Nd_2Fe_{14}BH_x$ phase, which shifts the diffraction peaks to lower 2θ positions and severely damages the magnetic properties of the synthesized particles. In this study, the sample milled at 550 rpm possesses the smallest average crystal size compared to other samples. This small crystal size made the particles more prone to hydrogen diffusion, and therefore the diffraction peaks for this sample shifted a bit towards the lower 2θ positions.

There is no CaO phase observed in the XRD of the by-product removed samples (Figure 5.10). In XRD, the detection limit of phase content in multiphase systems is ~ 2% [37, 38]. Hence the CaO phase were effectively removed from the sample after the by-product removal process. The energy dispersive X-ray spectra was employed to cross-check the removal of by-product. An example is shown in Figure 5.11, where the EDS of by-product removed $Nd_2(Fe,Co)_{14}B$ processed at 500 rpm is shown. In the energy spectra, only Nd, Fe and Co signals can be found and no Ca signals was present (the Si, O and C signals arise from the sample holder), which confirmed the CaO is fully removed from the $Nd_2(Fe,Co)_{14}B$ particles.

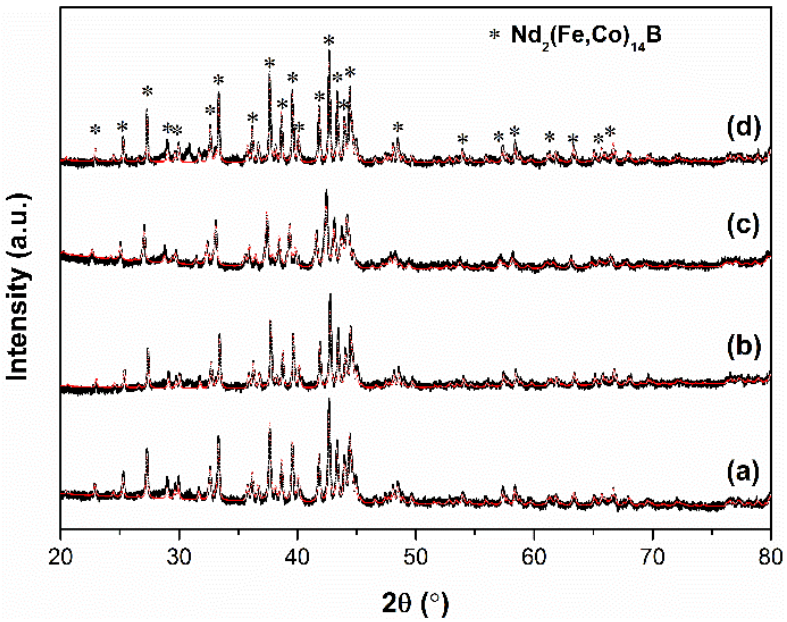

Figure 5.10. X-ray diffraction patterns and Rietveld analysis of samples produced at different ball milling speeds: (a) 450 rpm, (b) 500 rpm, (c) 550 rpm and (d) 600 rpm.

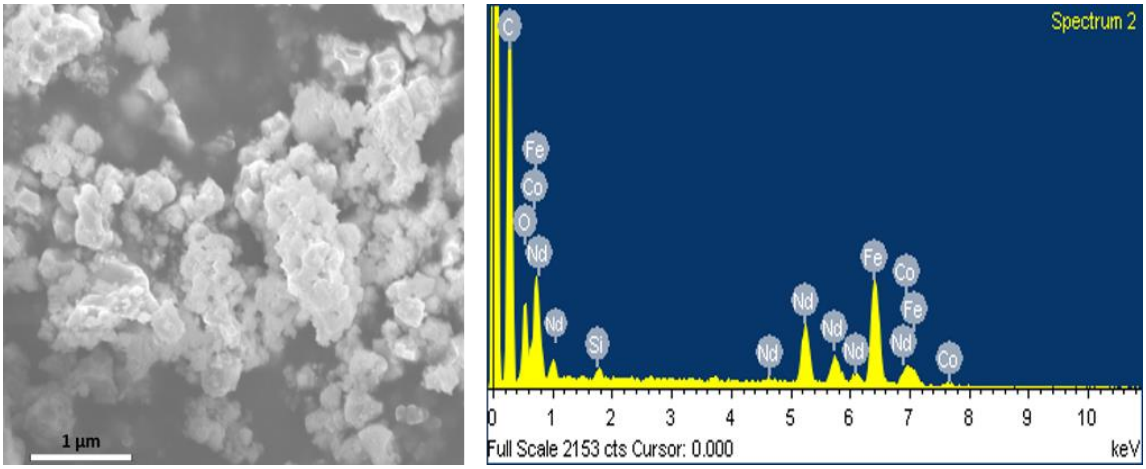

Figure 5.11. Secondary electron image and energy dispersive X-ray spectrum of the by-product removed sample processed at 500 rpm.

The TEM micrographs (Figure 5.12a-d) obtained for samples processed at various milling speeds were used to analyze the particle sizes and particle size distributions. Broad size distributions were obtained for all samples (Figure 5.13), majority of the particles have sizes in the range of 50 – 150 nm with an average particle size of ~ 100 nm. Different milling speeds did not induce significant variations in the average particle sizes and particle

size distributions. This could be because that two steps were there during the mechanochemical processing to determine the $Nd_2(Fe,Co)_{14}B$ particles formation: the milling process and the annealing process. In this case, the influence of annealing overrides the influence of milling on the particle size of $Nd_2(Fe,Co)_{14}B$. Therefore, no obvious effect from the milling speeds can be observed in particle sizes and particle size distributions. Though milling speeds did not directly influence the particle sizes, there is a strong relationship between the magnetic properties and the grain sizes. The grain sizes of the samples processed at different milling speeds were analyzed through the Rietveld refinement method and are listed in Figure 5.14. Larger grain sizes and lattice parameters corresponded to larger coercivity. By referring to the high resolution TEM micrographs (HRTEM) and selected area diffraction pattern (SADP) in Figure 5.12, the obtained $Nd_2(Fe,Co)_{14}B$ particles shows typical polycrystal structure. For example, for the 500 rpm processed sample, there are different structural orientations in the grains. The lattice spacing value of ~1.67 Å, 2.38 Å and 2.78 Å can be assigned to the (117), (303) and (111) $Nd_2(Fe,Co)_{14}B$ planes, respectively. The diffraction rings in the selected area diffraction pattern can be indexed to the respective planes as well. These results indicated that in the mechanochemical process, polycrystalline $Nd_2(Fe,Co)_{14}B$ nanoparticles were produced.

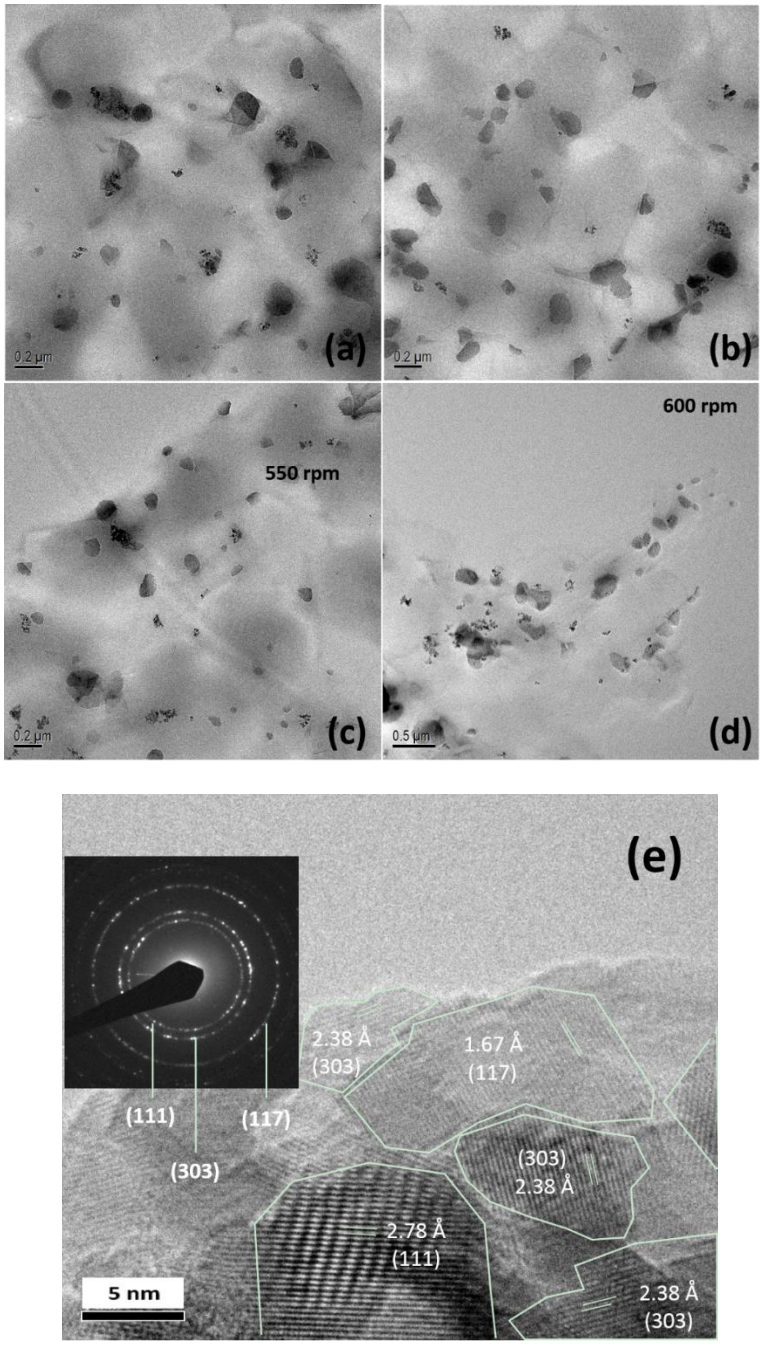

Figure 5.12. TEM bright field images of samples processed at different milling speeds: (a) 450 rpm, (b) 500 rpm, (c) 550 rpm and (d) 600 rpm. (e) High resolution electron micrograph image and the selected area diffraction pattern (SADP) of the sample processed at 500 rpm. The diffraction rings and the lattice spacing can be indexed to different $Nd_2(Fe,Co)_{14}B$ planes.

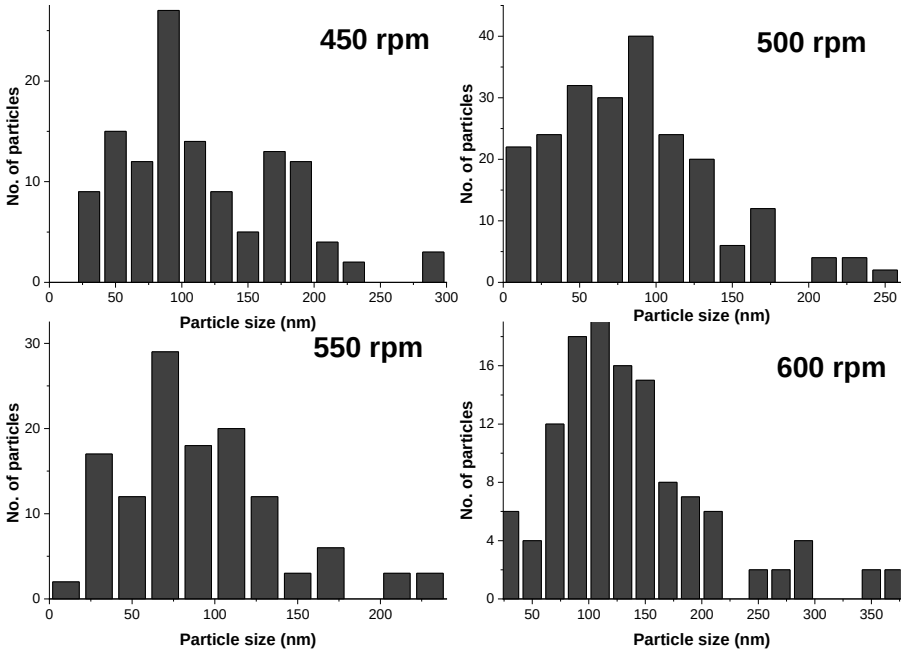

Figure 5.13. Particle size distributions of samples processed at different milling speeds: (a) 450 rpm, (b) 500 rpm, (c) 550 rpm and (d) 600 rpm.

Figure 5.14a shows the magnetic properties of the samples produced at various ball milling speeds after CaO removal. The coercivity (H_{ci}) ranges from 6.6 kOe to 9.4 kOe (Figure 5.14d) and the saturation magnetization at 1.5T (M_s^*) ranges from 60 emu/g to 75 emu/g (Figure 5.14e). It is worth noticing that the coercivity (H_{ci}) of samples milled at 500 rpm is higher than that of the CaO-0 sample milled at 500 rpm in chapter 4. This is because the use of different heat treatment procedures. In chapter 4, to highlight the influence of diluent content on $Nd_2(Fe,Co)_{14}B$ crystallite size, the samples were first sealed in a quartz tube at vacuum level better than 10^{-5} torr, then heat treated for 90 min in a pre-heated box furnace at 850 °C, followed by immediate quenching in ice water. In this chapter, all the samples were heat treated at 850 °C for 90 min in a vacuum tube furnace, followed by furnace cooling. Hence, the crystallite size for samples in this chapter were larger than those of CaO-0 samples in Chapter 4. Higher coercivity values were observed for furnace cooled samples, these samples followed the proposed crystallite size-coercivity relationship in Chapter 4.

The XRD data and Rietveld refinement was employed to calculate the lattice parameters (Figure 5.14b) and the average crystallite sizes (Figure 5.14c) of samples synthesized at different milling speeds. The coercivity H_{ci}, saturation magnetization at 1.5 T M_s^*, lattice parameter *a* and *c*, and crystal sizes are plotted in respect to milling speed in Figure 5.14 b-e. It can be seen that the change of coercivity H_{ci} follows the change in crystal size and lattice parameters. Superior coercivity values were observed for samples with larger crystal size and lattice parameters. Lower coercivity values were observed for samples with smaller crystal size and lattice parameters. Similar crystal size – coercivity relationship was reported in Chapter 4 as well [11, 35]. And researchers have also reported that the values of lattice parameters decreased with increasing Fe replacement of Co in the $Nd_2Fe_{14}B$ structure (up to 30 %), together with an enhancement in magnetization values [39]. The change in lattice parameters results in a variation in the strength of internal exchange interactions, therefore a change in the magnetic properties is expected [40]. However, due to the small magnitude of the lattice parameter changes, the relationship between magnetic properties and lattice parameters still needs to be further confirmed. The relationship between crystallite size and coercivity were also observed in Chapter 4 [11, 35] where larger crystallite size resulted in higher coercivity. Samples with larger crystallite size will have less surface defects, hence less reverse nucleation sites will be generated during the coercivity reversal processes, and higher coercivity values are expected.

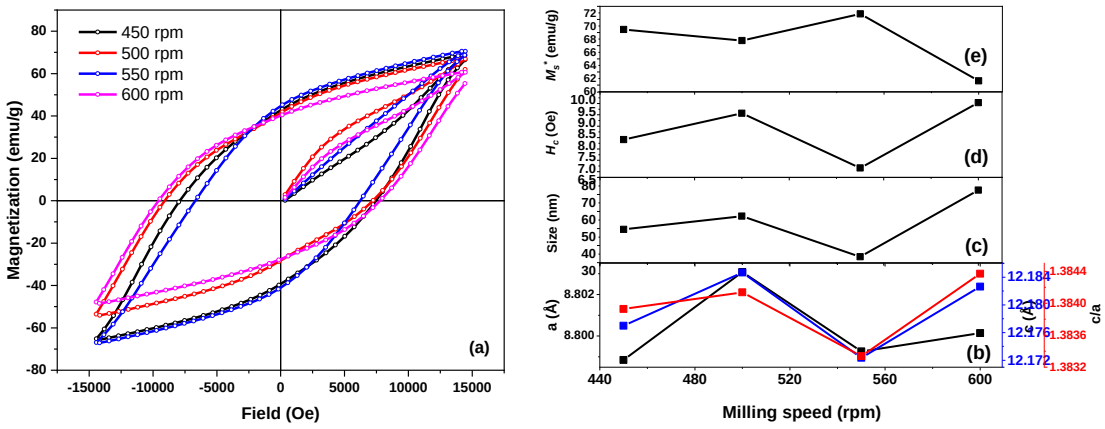

Figure 5.14. (a) Magnetic hysteresis loops, (b) lattice parameters, (c) size, (d) H_c and (e) M_s of by-product removed samples produced at various ball milling speeds (450 rpm, 500 rpm, 550 rpm and 600 rpm).

5.3 Conclusions

Through a study of the phase and structural evolution as a function of milling time, the reaction mechanism during mechanochemical synthesis of $Nd_2(Fe,Co)_{14}B$ was revealed. A three-stage milling process was observed. The propagation of the chemical reduction reactions requires continuous input of mechanical energy. Hence, it is not a self-propagating process, unlike many mechanochemical metathesis reactions. Continuous energy input is required for the system to reach steady-state.

The phase transformation processes and kinetics of chemical reactions during mechanochemical synthesis of $Nd_2(Fe,Co)_{14}B$ at different milling speeds were studied. A three-stage milling process was observed at all milling speeds: (i) high milling energy amorphizes the precursor oxides (Nd_2O_3, Fe_2O_3, CoO and B_2O_3), leading to a large increase in amorphous phase content; (ii) continuous milling provides energy for Ca to slowly reduce the precursor oxides, resulting in the formation of the α-Fe phase and an increase in CaO content; (iii) further milling does not influence reduction, the mass fraction of the reaction products remains constant. During the milling process, the content of the α-Fe and CaO phases slowly increased until a steady state is reached. The reaction kinetics of this process was experimentally investigated by measuring the CaO content. A theoretical model, $y = 1 - \exp(At^2 - Bt + C_2)$ was developed to predict the milling kinetics. The experimental data at ball milling speeds of 450 rpm, 500 rpm, 550 rpm and 600 rpm matched well with the theoretical model. A maximum milling efficiency was observed at a milling speed of 550 rpm. The desired tetragonal crystal structure $Nd_2(Fe,Co)_{14}B$ particles exhibit coercivity values ranging from 6.6 kOe to 9.4 kOe. It was found that the coercivity value increased with increasing crystallite size and larger lattice parameters.

References

[1] S. L. James and T. Friščić. *Chemical Society Reviews*. **2013**, 42, 7494-7496.

[2] T. Friščić, I. Halasz, P. J. Beldon, A. M. Belenguer, F. Adams, S. A. Kimber, V. Honkimäki, and R. E. Dinnebier. *Nature Chemistry*. **2013**, 5, 66-73.

[3] V. V. Boldyrev. *Russian Chemical Reviews*. **2006**, 75, 177.

[4] P. G. McCormick, T. Tsuzuki, J. S. Robinson, and J. Ding. *Advanced Materials*. **2001**, 13, 1008-1010.

[5] W. Liu and P. McCormick. *Journal of Magnetism and Magnetic Materials*. **1999**, 195, L279-L283.

[6] A. Pal, A. Gabay, and G. C. Hadjipanayis. *Journal of Alloys and Compounds*. **2012**, 543, 31-33.

[7] A. Gabay and G. Hadjipanayis. *Journal of Physics D: Applied Physics*. **2014**, 47, 182001.

[8] A. Gabay, X. Hu, and G. Hadjipanayis. *Journal of Magnetism and Magnetic Materials*. **2014**, 368, 75-81.

[9] O. Koylu-Alkan, J. Barandiaran, D. Salazar, and G. Hadjipanayis. *AIP Advances*. **2016**, 6, 056027.

[10] A. M. Gabay, X. C. Hu, and G. C. Hadjipanayis. *Journal of Alloys and Compounds*. **2013**, 574, 472-476.

[11] Y. Zhong, V. Chaudhary, X. Tan, H. Parmar, and R. V. Ramanujan. *Nanoscale*. **2017**, 9, 18651-18660.

[12] J.-L. Do and T. Friščić. *ACS Central Science*. **2016**, 3, 13-19.

[13] X. Liu, L. Hu, and Y. Mei. *International Journal of Hydrogen Energy*. **2013**, 38, 13694-13701.

[14] X. Ma, W. Yuan, S. E. Bell, and S. L. James. *Chemical Communications*. **2014**, 50, 1585-1587.

[15] K. Užarević, I. Halasz, and T. Friščić. *The Journal of Physical Chemistry Letters*. **2015**, 6, 4129-4140.

[16] S. A. Humphry-Baker, S. Garroni, F. Delogu, and C. A. Schuh. *Nature Materials*. **2016**, 15, 1280-1286.

[17] M. Magini, C. Colella, A. Iasonna, and F. Padella. *Acta Materialia*. **1998**, 46, 2841-2850.

[18] M. Magini, A. Iasonna, and F. Padella. *Scripta Materialia*. **1996**, 34, 13-19.

[19] A. Iasonna and M. Magini. *Acta Materialia*. **1996**, 44, 1109-1117.

[20] M. Magini, N. Burgio, A. Iasonna, S. Martelli, F. Padella, and E. Paradiso. *Journal of Materials Synthesis and Processing (USA)*. **1993**, 1, 135-144.

[21] S. Shukla, A. Banas, and R. V. Ramanujan. *Physica Status Solidi -Rapid Research Letters*. **2011**, 5, 169-171.

[22] S. Shukla, A. Banas, and R. V. Ramanujan. *Intermetallics*. **2011**, 19, 1265-1273.

[23] S. Shukla, D. T. Wu, H. Ramanarayan, D. Srolovitz, and R. V. Ramanujan. *Acta Materialia*. **2013**, 61, 3242-3248.

[24] W. Miao, J. Ding, P. McCormick, and R. Street. *Journal of Physics D: Applied Physics*. **1996**, 29, 2370.

[25] W. Miao, J. Ding, P. McCormick, and R. Street. *Journal of Applied Physics*. **1996**, 79, 2079-2083.

[26] T. Nagase, A. Nino, T. Hosokawa, and Y. Umakoshi. *Materials Transactions*. **2007**, 48, 1651-1658.

[27] A. P. Gonçalves and M. Almeida. *Physica B: Condensed Matter*. **1996**, 228, 289-294.

[28] B. Zhang and W. A. Jesser. *Physica B: Condensed Matter*. **2002**, 315, 123-132.

[29] P. Y. Butyagin. *Advances in Mechanochemistry, Physical and Chemical Processes under Deformation. Harward Acad. Publ*. **1998**, 91-165.

[30] P. Y. Butyagin and A. Streletskii. *Physics of the Solid State*. **2005**, 47, 856-862.

[31] A. Gusev and A. Kurlov. *Inorganic Materials*. **2009**, 45, 35-42.

[32] R. Tran, Z. Xu, D. W. Balachandran Radhakrishnan, W. Sun, K. A. Persson, and S. P. Ong. *Scientific Data*. **2016**, 3, 160080.

[33] P. Deheri, S. Shukla, and R. V. Ramanujan. *Journal of Solid State Chemistry*. **2012**, 186, 224-230.

[34] H. E. Kissinger. *Analytical Chemistry*. **1957**, 29, 1702-1706.

[35] X. Tan, H. Parmar, Y. Zhong, V. Chaudhary, and R. V. Ramanujan. *IEEE Magnetics Letters*. **2017**, PP, 1-5.

[36] H. Parmar, T. Xiao, V. Chaudhary, Y. Zhong, and R. V. Ramanujan. *Nanoscale*. **2017**, 9, 13956-13966.

[37] B. Ehlmann, D. Bish, S. Ruff, and J. Mustard. *Journal of Geophysical Research: Planets*. **2012**, 117, E00J16.

[38] D. L. Bish and S. J. Chipera. *Clays and Clay Minerals*. **1991**, 39, 437-445.

[39] Y. c. Yang, W. W. Ho, H. y. Chen, J. Wang, and J. Lan. *Journal of Applied Physics*. **1985**, 57, 4118-4120.

[40] X. Fang, Y. Shi, and D. Jiles. *IEEE Transactions on Magnetics*. **1998**, 34, 1291-1293.

Chapter 6 *

Effect of Dy-alloying on mechanochemically synthesised $(Nd_{1-x}Dy_x)_2(Fe,Co)_{14}B$ Nanoparticles

$(Nd_{1-x}Dy_x)_2(Fe,Co)_{14}B$ magnetic nanoparticles, in a range of Dy content （x） from 0 to 0.6, were synthesized by a mechanochemical process. The effect of Dy substitution on the magnetic properties and crystal structure of the nanoparticles were studied. With increasing Dy content, the coercivity of $(Nd_{1-x}Dy_x)_2(Fe,Co)_{14}B$ particles first doubled from 8.8 kOe (x=0) to a high value of 17.8 kOe (x=0.5), further increase of Dy content led to a slightly lower coercivity of 17.5 kOe (x=0.6). $(Nd_{0.8}Dy_{0.2})_2(Fe,Co)_{14}B$ particles exhibited good thermal stability, with a thermal coefficient of remanence (α) of -0.053% and thermal coefficient of coercivity (β) of -0.348%. Reduced spin-reorientation temperatures (T_{SR}) of 105 K – 115 K were observed for $(Nd_{1-x}Dy_x)_2(Fe,Co)_{14}B$, for x in the range of 0 to 0.2, making these compositions more attractive for cryogenic applications. Detailed analysis of the temperature dependent magnetic properties revealed that coercivity was controlled by the nucleation of reversed magnetic domains.

---

*The content of this section is submitted substantially as reference:

1. Y. Zhong, V. Chaudhary, X. Tan, H. Parmar & R. V. Ramanujan. High coercivity Nd-Fe-Co-B magnetic nanoparticles produced by mechanochemical processing. *Journal of Magnetism and Magnetic Materials* (submitted).

6.1 Introduction

Nd-Fe-B based permanent magnets are of high current scientific and industrial interest due to their excellent magnetic properties [1-5]. They possess the highest energy product and are especially useful in energy generation and conversion systems, such as motors, electric and hybrid vehicles, wind turbines, etc [4, 6]. Coey's prediction of a giant energy product in anisotropic nanocomposite magnets [7] and Cui et al.'s report of high $(BH)_{max}$ in nanocomposite thin films [8] have spurred great interest in the development of nanostructured Nd-Fe-B based magnets to further enhance the magnetic performance. Various processing techniques have been employed to produce such magnets. Physical methods, such as ball milling, hydrogenation-disproportionation-desorption-recombination (HDDR) and melt spinning are well-developed and widely used to synthesize hard magnets [9]. Surfactant assisted ball milling has also been utilized to process magnetic nanoparticles with sizes ranging from 10 nm to 100 nm [10-13]. One major shortcoming of such physical methods is that they are associated with high cost due to the use of elemental powders as precursors. To overcome this disadvantage, researchers have studied various chemical methods to synthesis Nd-Fe-B nanoparticles. These chemical methods include sol-gel processing, microwave induced combustion, mechanochemical processing, etc. [10, 14-19]. All these chemical methods to produce hard magnetic nanoparticles exhibit advantages such as enhanced shape control, and lower processing cost. However, the use of chemical methods to produce Nd-Fe-B nanoparticles typically results in limited magnetic properties. On the other hand, the mechanochemical process, which utilizes low cost metal oxides as precursors, can produce Nd-Fe-B based nanoparticles with higher coercivity (H_C) while minimizing precursor cost [14-16, 20].

The magnetic properties of $Nd_2Fe_{14}B$ based alloys can be improved by alloying. The substitution of Nd by heavy rare earth elements (e.g., Dy) can increase H_C [21-23] since the $Dy_2Fe_{14}B$ phase has higher magnetocrystalline anisotropy compared to the $Nd_2Fe_{14}B$ phase. Co substitution of Fe in $Nd_2Fe_{14}B$ increases the Curie temperature (T_C) and has minimum deleterious effects on the coercivity and magnetization [6, 24]. However, the thermal stability of $Nd_2Fe_{14}B$ cannot be improved only by Co substitution. Dy substitution

can enhance the thermal stability of Nd-Fe-B magnets and also expanding their operating temperature range. Thus, combining the effect of Dy substitution of Nd and Co substitution of Fe can improve T_C, thermal stability as well as other magnetic properties of Nd-Fe-B magnets. While most investigations have focused on the magnetic properties, less attention has been paid to the coercivity mechanism and the associated magnetization reversal process. Two mechanisms, i.e., nucleation of reverse domains and pinning of domain walls have been identified [25, 26]. Nucleation of reversed domains starts at surface irregularities and impurities with low anisotropy, this mechanism has been widely employed to understand the magnetic behavior of sintered Nd-Fe-B magnets [27, 28]. The domain wall pinning model suggests that impurities within the magnetic phase can prevent/slow down domain wall motion, thus increasing H_C. It has been used to explain the behavior of melt spun Nd-Fe-B ribbons and Sm_2Co_{17}-based magnets. However, the reversal mechanism for Nd-Fe-B nanoparticles is still not well understood, numerical models have been proposed to understand the coercivity mechanism [29]. The temperature dependent magnetic properties can be used to experimentally determine the coercivity mechanism.

In our previous study, we developed $Nd_2(Fe,Co)_{14}B$ nanoparticles with coercivity (H_C) of 8.8 kOe [20]. Here, we use the mechanochemical method to synthesize Dy substituted $(Nd_{1-x}Dy_x)_2(Fe,Co)_{14}B$, with x in the range of 0 to 0.6. The magnetic behaviour of these particles was examined and the optimum Dy content was determined. The temperature dependent magnetic behaviour was also measured to determine the effect of Dy substitution on thermal stability. The coercivity mechanism of these samples was analysed by comparing the temperature dependent magnetic properties with the predictions of numerical modelling.

6.2 Results and Discussions

6.2.1 Structural analysis of $(Nd_{1-x}Dy_x)_2(Fe,Co)_{14}B$ nanoparticles

In the previous thesis chapter, we reported the influence of CaO, acting as a dispersant, on the magnetic properties of $Nd_2(Fe,Co)_{14}B$ magnetic particles produced by the mechanochemical process. Adding 50 wt% CaO in the starting material resulted in optimum magnetic properties [20]. Hence 50 wt% CaO was added in all samples. Dy substitution of Nd can enhance the anisotropy field of the tetragonal 2-14-1 phase by the formation of the high-anisotropy $(Nd,Dy)_2Fe_{14}B$ phase [30-32]. To improve the magnetic properties and study the influence of substituting Nd by Dy, six sample sets with a nominal composition of $(Nd_{1-x}Dy_x)_2(Fe,Co)_{14}B$ (x = 0.1, 0.2, 0.3, 0.4, 0.5 and 0.6) were synthesized by the mechanochemical process. X-ray diffraction patterns and Rietveld refinement of all samples were performed and compared with Dy-free sample (Figure 6.1). The desired tetragonal 2-14-1 structure was formed in all cases (Figure 6.1A). The desired $(Nd_{1-x}Dy_x)_2(Fe,Co)_{14}B$ phase co-exists with the by-product, i.e., CaO. XRD patterns and refinement for the samples after by-product removal are shown in Figure 6.1B. It can be seen that with increasing Dy content, the $(Nd_{1-x}Dy_x)_2(Fe,Co)_{14}B$ diffraction peaks shifted to higher angles.

According to Bragg's equation, $n\lambda = 2dsin\theta$, the higher angle of diffraction (2θ) indicates that the interplanar spacing (*d*) decreases with increasing Dy content. The lattice parameters were calculated from Rietveld refinement (Table 6.1). The lattice parameters *a*, *c* and the cell volume *v* decreased with increasing *x* value, indicating that a smaller cell structure was obtained by Dy substitution. This can be explained by the fact that the lattice parameters (*a* and *c*) of $Dy_2Fe_{14}B$ are smaller than $Nd_2Fe_{14}B$ due to lanthanide contraction [22, 31]. With increasing value of *x*, greater replacement of Nd by Dy occurs, resulting in a contracted tetragonal cell structure, leading to the shift of diffraction peaks to higher 2θ. The bright field TEM image of $(Nd_{0.8}Dy_{0.2})_2(Fe,Co)_{14}B$ after by-product removal is shown in Figure 6.2a. As in the case of our previous study on $Nd_2(Fe,Co)_{14}B$, a range of particle sizes between 10 nm and 150 nm were observed. A grain size of ~ 30 nm was observed (see the inset high resolution image), which is close to the value we obtained from Rietveld refinement (Table 6.1).

TEM EDS mapping of Nd, Dy and Fe in the $(Nd_{0.6}Dy_{0.4})_2(Fe,Co)_{14}B$ particles after by-product removal was performed to study the distribution of Dy in the powder particles (Figure 6.2b). No preferential distribution or segregation of Dy was observed, indicating that Dy was homogeneously distributed. The EDS maps and the decrease of lattice parameter indicate that there is negligible segregation of Dy. With increasing value of *x*, the majority phase changes from the Nd dominated $(Nd_{1-x}Dy_x)_2(Fe,Co)_{14}B$ phase to the Dy dominated $(Nd_{1-x}Dy_x)_2(Fe,Co)_{14}B$ phase.

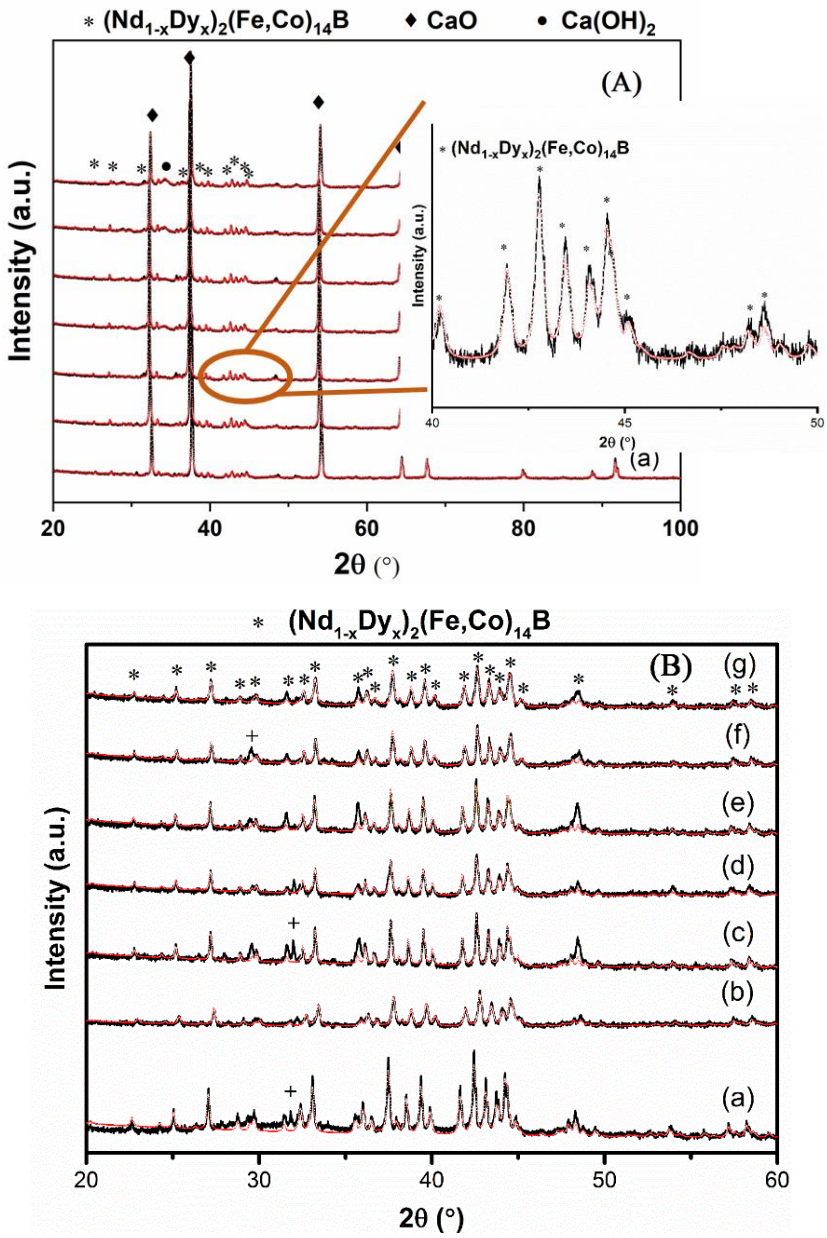

Figure 6.1. (A) X-ray diffraction patterns and Rietveld refinement of the mechanochemically synthesized $(Nd_{1-x}Dy_x)_2(Fe,Co)_{14}B$ particles prepared in a range of Dy content (a) x=0, (b) x=0.1, (c) x=0.2, (d) x=0.3, (e) x=0.4, (f) x=0.5, (g) x= 0.6. (B) X-ray diffraction patterns and Rietveld refinement of the $(Nd_{1-x}Dy_x)_2(Fe,Co)_{14}B$ particles after removal of by-product (a) x=0, (b) x=0.1, (c) x=0.2, (d) x=0.3, (e) x=0.4, (f) x=0.5, (g) x= 0.6. Black curves are experimental data, red dots are calculated data from Rietveld refinement. The diffraction peaks indicated by "+" were not identified.

Table 6.1.Structural parameters obtained from refinement of X-ray diffraction patterns of $(Nd_{1-x}Dy_x)_2(Fe,Co)_{14}B$ (x = 0, 0.1, 0.2, 0.3, 0.4, 0.5, 0.6) particles after removal of by-product.

x	a (Å)	c (Å)	v (Å^3)	Crystal size $L_{vol\text{-}IB}$ (nm)	R_{bragg}
0	8.769	12.143	933.76	46.6	2.4
0.1	8.767	12.142	933.41	52.7	2.4
0.2	8.764	12.117	930.65	59.2	1.7
0.3	8.765	12.118	931.10	58.5	1.7
0.4	8.755	12.086	926.36	50.9	1.7
0.5	8.748	12.054	922.39	57.6	1.8
0.6	8.747	12.042	921.39	42.8	2.3

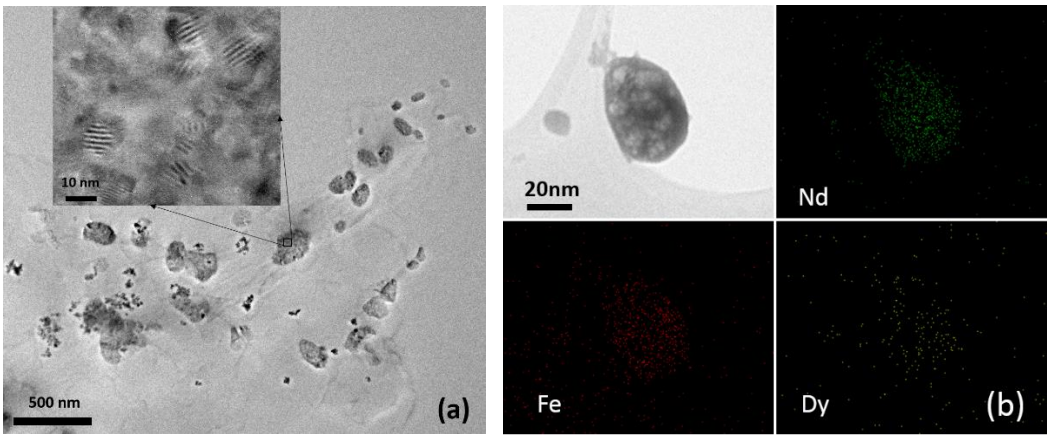

Figure 6.2. (a). Bright field transmission electron micrographs of $(Nd_{0.8}Dy_{0.2})_2(Fe,Co)_{14}B$ particles after removal of by-product; (b) Energy dispersive spectroscopy maps of $(Nd_{0.6}Dy_{0.4})_2(Fe,Co)_{14}B$ particles after removal of by-product.

6.2.2 Room temperature magnetic properties of $(Nd_{1-x}Dy_x)_2(Fe,Co)_{14}B$

The M-H hysteresis loop in Figure 6.3 shows the room temperature magnetic properties for $(Nd_{1-x}Dy_x)_2(Fe,Co)_{14}B$ particles over a range of Dy content (x = 0, 0.1, 0.2, 0.3, 0.4, 0.5, 0.6) before (Figure 6.3a) and after by-product removal (Figure 6.3b). It can be seen from Figure 6.3c that with increasing Dy content before by-product removal, H_C increased

continuously from 12.5 kOe to a high value of 24.2 kOe. The origin of the coercivity increase in Nd-Fe-B magnets is the large magnetocrystalline anisotropy of $Nd_2Fe_{14}B$. The continuous increase of H_C (Figure 6.3c) demonstrates the positive effect of Dy alloying on the local magnetocrystalline anisotropy [22]. The intrinsic anisotropy field (H_A) of $Dy_2Fe_{14}B$ (15.8 T) is much higher than that of $Nd_2Fe_{14}B$ (7.5T). This high intrinsic anisotropy field (H_A) can suppress the nucleation of reverse domains at low magnetic fields and increase the coercivity. Therefore, with increasing Dy content, the $(Nd_{1-x}Dy_x)_2(Fe,Co)_{14}B$ phase will have much higher local magnetocrystalline anisotropy/intrinsic anisotropy field, leading to enhanced H_C values. After by-product removal, H_C increases from 8.8 kOe to 17.8 kOe with increasing amount of Dy substitution until x=0.5 (Figure 6.3b and 6.3d). Substitution of Nd by Dy in $Nd_2Fe_{14}B$ is expected to continuously increases coercivity until 100% replacement. However, in our work, after by-product removal, the H_C decreased to 17.5 kOe with substitution of Nd by Dy at x = 0.6. This could be due to the process of removal of by-product, which can affect the particle surfaces, providing more sites for the activation of reversal mechanisms. The graphs of saturation magnetization v/s Dy content are shown in Figure 6.3e and 6.3f. With increasing Dy content, the saturation magnetization at 5 T decreased continuously.

It is challenging to directly observe the coercivity mechanism of magnetic materials due to the small size of the critical nucleus involved and the suddenness and short time required for the phenomenon. However, magnetization measurements can provide important information on the reversal mechanism [29]. The virgin magnetization curve for samples before by-product removal (Figure 6.3a) initially exhibits high susceptibility, followed by lower susceptibility all the way to saturation, which is the typical behavior of a nucleation-type magnet. On the other hand, the virgin magnetization curve for samples after by-product removal (Figure 6.3b) does not follow the steep virgin magnetization curve for a nucleation-type magnet nor the low initial susceptibility of a pinning-type magnet. This indicates a complex combined coercivity mechanism in the by-product removed samples [33].

To further analyze the magnetic reversal, the demagnetization curves at first quadrant of the MH loops for selected samples were taken out and analyzed. The normalized slopes (*dM/dH*) of these demagnetization curves were plotted for $(Nd_{1-x}Dy_x)_2(Fe,Co)_{14}B$ particles (x = 0, 0.1, 0.5). The value of this slop is an indicator of the amount of grains that reverse their magnetization when the field is changed from H_i to $H_{(i+1)}$. The normalized slopes indicate the relative amount of grains that have reversed for that field interval, *dH*. This method is generally used to describe the fraction of reversed grains during the demagnetization process [34] [35]. The magnetization of grains will reverse when the external applied field is larger than the coercivity of this grain. Thus the measurement of the relationship between the magnitude of applied field and the amount of reversed magnetization is a method to estimate the distribution of coercivity. In order to compare the distribution of coercivity correctly in different samples, they need to have the same degree of orientation because the coercivity has an angular dependence. Figure 6.4 shows the relationship between *dM/dH* and applied field of the aligned $(Nd_{1-x}Dy_x)_2(Fe,Co)_{14}B$ particles (x = 0, 0.1, 0.5). It was found that in all cases. Nominal *dM/dH* increased gradually from lower H to higher values. Comparing to literature, most of the sintered and the melt-spun Nd-Fe-B magnets have a nearly zero nominal *dM/dH* at small external magnetic field (*H*<6kOe). The plots for our particles indicates that there is an inhomogeneity in their coercivity. It could be that there is a distribution of particle sizes in each set of samples. For the smaller particles with higher surface/volume ratio, there is a higher chance to induce high surface defects/volume ratio during by-product removal process. These high surface defects/volume ratio led to smaller larger amount of reversal magnetization nucleation sites and ease the magnetization reversal process. On the other hand, larger particles have relatively smaller surface defects/volume ratio, thus smaller amount of reversal magnetization nucleation sites is induced during by-product removal. Therefore, there is a range of coercivity exist in our sample. Hence, nucleation-controlled mechanism can be adopted to explain the behaviour of demagnetization curves for the by-product removed samples.

To further analyze the magnetic reversal, the demagnetization curves at first quadrant of the MH loops for selected samples were taken out and analyzed. The normalized slopes

(*dM/dH*) of these demagnetization curves were plotted for $(Nd_{1-x}Dy_x)_2(Fe,Co)_{14}B$ particles (x = 0, 0.1, 0.5). The value of this slop is an indicator of the amount of grains that reverse their magnetization when the field is changed from H_i to $H_{(i+1)}$. The normalized slopes indicate the relative amount of grains that have reversed for that field interval, *dH*. This method is generally used to describe the fraction of reversed grains during the demagnetization process [34] [35]. The magnetization of grains will reverse when the external applied field is larger than the coercivity of this grain. Thus the measurement of the relationship between the magnitude of applied field and the amount of reversed magnetization is a method to estimate the distribution of coercivity. In order to compare the distribution of coercivity correctly in different samples, they need to have the same degree of orientation because the coercivity has an angular dependence. Figure 6.4 shows the relationship between *dM/dH* and applied field of the aligned $(Nd_{1-x}Dy_x)_2(Fe,Co)_{14}B$ particles (x = 0, 0.1, 0.5). It was found that in all cases. Nominal *dM/dH* increased gradually from lower H to higher values. Comparing to literature, most of the sintered and the melt-spun Nd-Fe-B magnets have a nearly zero nominal *dM/dH* at small external magnetic field (H<6kOe). The plots for our particles indicates that there is an inhomogeneity in their coercivity. It could be that there is a distribution of particle sizes in each set of samples. For the smaller particles with higher surface/volume ratio, there is a higher chance to induce high surface defects/volume ratio during by-product removal process. These high surface defects/volume ratio led to smaller larger amount of reversal magnetization nucleation sites and ease the magnetization reversal process. On the other hand, larger particles have relatively smaller surface defects/volume ratio, thus smaller amount of reversal magnetization nucleation sites is induced during by-product removal. Therefore, there is a range of coercivity exist in our sample. Hence, nucleation-controlled mechanism can be adopted to explain the behaviour of demagnetization curves for the by-product removed samples.

Removal of CaO should not induce any change in the virgin magnetization curve as CaO is a non-magnetic phase. It was found that for Nd-Fe-B phase, the texture/crystallographic does not change after by-product removal process. The insert in Figure 6.1A shows a zoom-in for the XRD pattern of the samples before by-product removal. There is almost no

texture changes between the sample before and after by-product removal. The study done by Campo et. al. suggests that the volume fraction of single domain particles in the samples will influence the behavior of the initial curve [36]. With greater volume fraction of single domain particles, lower initial susceptibility will be observed. This could be relevant to our observations. Before by-product removal, the Nd-Fe-B particles are embedded in the CaO matrix and they behave as a bulk multi-domain particle. However, after by-product removal, some of the particles became single domain particles. This can be validated by the change of crystallographic texture in XRD under the application of external magnetic field (Figure 4.4a). Therefore, greater volume fraction of single domain particles presents after by-product removal and results in a smaller susceptibility. Hence, texture doesn't seem to induce a change of behavior for the initial magnetization curve. Instead, increased volume fraction of single domain magnetic nanoparticles and the removal of some phase during by-product removal process might lead to a change in initial curve.

The observed change of the shape of the initial curve indicates that some magnetic phase was altered by by-product removal. It could be that before by-product removal, some defects were induced at the surface of the individual $(Nd_{1-x}Dy_x)_2(Fe,Co)_{14}B$ crystals. These defects acted as pinning sites, which altered the shape of the initial magnetization curve. An analysis of the coercivity mechanism for by-product removed samples will be presented later.

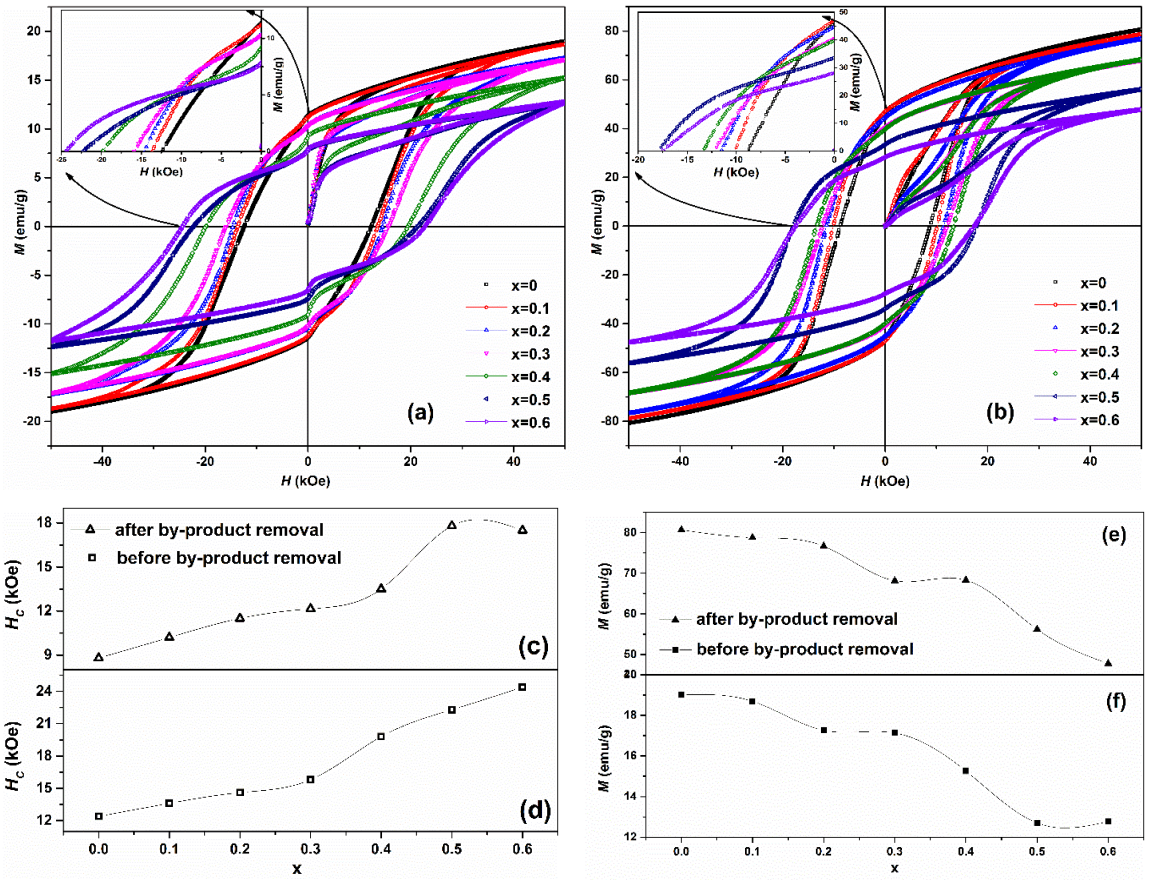

Figure 6.3. Room temperature magnetic hysteresis (M-H) loops of $(Nd_{1-x}Dy_x)_2(Fe,Co)_{14}B$ particles (x = 0, 0.1, 0.2, 0.3, 0.4, 0.5, 0.6) (a) before by-product removal, (b) after by-product removal, the insets show the corresponding magnified second quadrant of these M-H curves. Room temperature coercivity of $(Nd_{1-x}Dy_x)_2(Fe,Co)_{14}B$ particles (x = 0, 0.1, 0.2, 0.3, 0.4, 0.5, 0.6) (c) after by-product removal, (d). before by-product removal. Room temperature saturation magnetization (at 5T) of $(Nd_{1-x}Dy_x)_2(Fe,Co)_{14}B$ particles (x = 0, 0.1, 0.2, 0.3, 0.4, 0.5, 0.6) (e) after by-product removal, (f). before by-product removal.

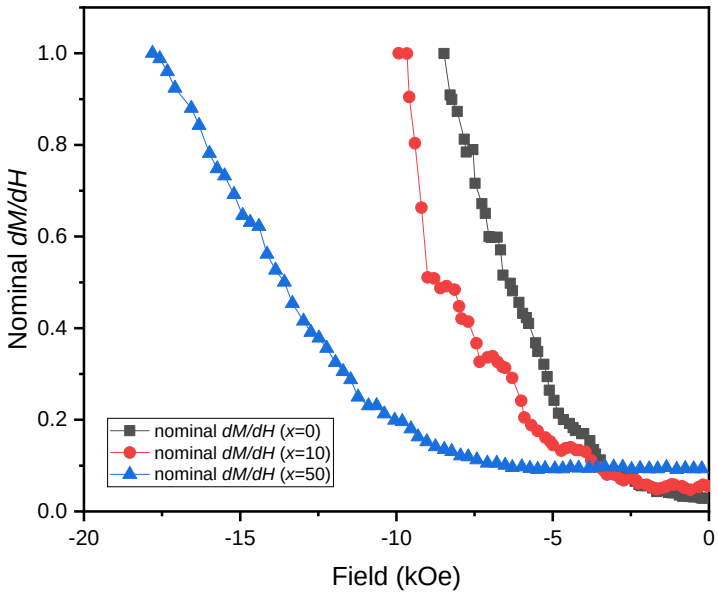

Figure 6.4. Nominal dM/dH vs. demagnetization field (H) for the aligned $(Nd_{1-x}Dy_x)_2(Fe,Co)_{14}B$ particles (x = 0, 0.1, 0.5).

In our previous study, we found that the properties of $Nd_2(Fe,Co)_{14}B$ particles are highly sensitive to the degree of magnetic alignment. In this study, we examined the response of the $(Nd_{0.8}Dy_{0.2})_2(Fe,Co)_{14}B$ particles to magnetic alignment. $(Nd_{0.8}Dy_{0.2})_2(Fe,Co)_{14}B$ particles were embedded in a liquid adhesive and aligned under a 1.8 T magnetic field generated by an electromagnet. The magnetic field was removed after drying of the liquid adhesive. Figure 6.4a shows the room temperature M-H loop measured for powder samples which were randomly oriented, and for aligned samples measured in the direction ⊥ and // to the alignment direction, respectively. The shape of the M-H loop was found to be highly sensitive to magnetic alignment by the external magnetic field. The value of remanent magnetization (M_r) almost tripled after magnetic alignment. To quantify the degree of magnetic alignment, we calculated the average misorientation angle $\varphi = arctan(\frac{2M_r^{\perp}}{M_r^{//}})$ [37]. The value φ represents the angle between the macroscopic magnetization easy axis and the individual magnetization easy axis in each grain. The smaller the value of φ, the better the alignment. Commercial isostatic pressing provides an optimally aligned magnet with $\varphi = 11 - 14^0$ [35]. For our $(Nd_{0.8}Dy_{0.2})_2(Fe,Co)_{14}B$ particles, a value of $\varphi = 39^0$

was obtained. Typically, smaller particle size and grain size tend to randomize grain orientations and reduce the degree of alignment and increase the value of φ. Thus, the φ values of nanocrystalline magnetic nanoparticles lie in the range of 34-48°[38].

We also calculated the energy product $(BH)_{max}$ of the $(Nd_{0.8}Dy_{0.2})_2(Fe,Co)_{14}B$ particles, assuming a particle packing density of 7.4 g/cm^3 (Figure 6.5b). Magnetic alignment enhanced the $(BH)_{max}$ from 2.8 MGOe to 6.6 MGOe. This increase of $(BH)_{max}$ was due to the increase of B in the samples due to magnetic alignment. The alignment of particles along their easy axis increases the values of M_r and B_r. The $(BH)_{max}$ for all Dy substituted samples were also calculated and shown in Figure 6.6.

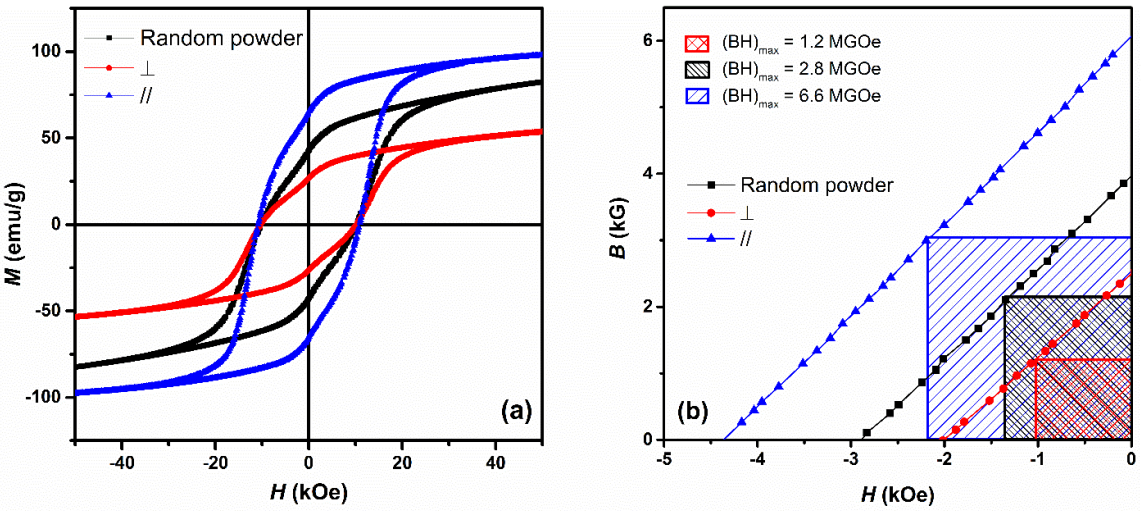

Figure 6.5. (a) Room temperature M-H magnetic hysteresis loop of $(Nd_{0.8}Dy_{0.2})_2(Fe,Co)_{14}B$ measured in randomly oriented samples and aligned samples, ⊥ and // to the magnetic alignment c-axis direction; (b) Room temperature demagnetization second quadrant B-H curve of $(Nd_{0.8}Dy_{0.2})_2(Fe,Co)_{14}B$ particles, the shaded area represents $(BH)_{max}$.

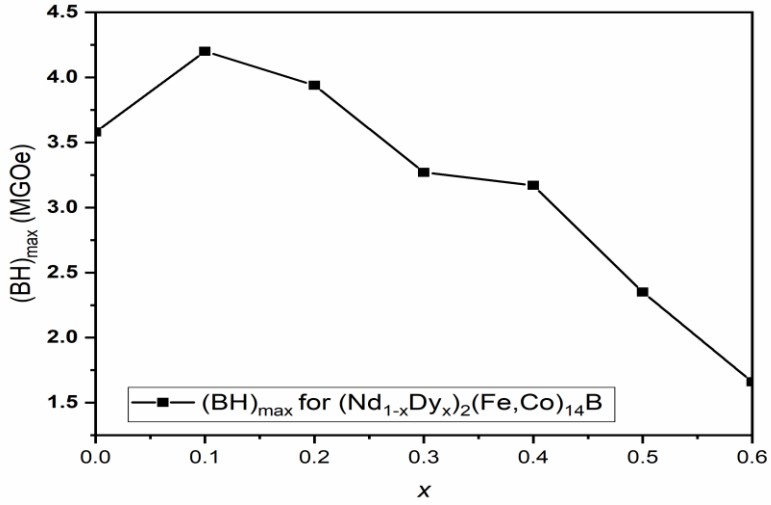

Figure 6.6. $(BH)_{max}$ for $(Nd_{1-x}Dy_x)_2(Fe,Co)_{14}B$ (x = 0, 0.1, 0.2, 0.3, 0.4, 0.5, 0.6) without magnetic alignment.

6.2.3 Temperature dependent magnetic properties

To study the influence of Dy on the temperature dependent magnetic properties, the M-H hysteresis loops of $(Nd_{0.8}Dy_{0.2})_2(Fe,Co)_{14}B$ were measured at different temperatures. Figure 6.7a shows the demagnetization curves of M-H hysteresis loops at temperatures ranging from 100 K to 400 K of $(Nd_{0.8}Dy_{0.2})_2(Fe,Co)_{14}B$. It can be seen that, due to thermal effects, both H_c and M_r increased with decreasing temperature from 400 K to 150 K. Further decrease of temperature from 150 K to 100 K led to a deep kink in the demagnetization curve, a decrease in H_c, and an increase in M_s. A maximum in H_c can be observed at a temperature of 150K. A similar behavior was observed in $(Nd_{0.9}Dy_{0.1})_2(Fe,Co)_{14}B$ and $Nd_2(Fe,Co)_{14}B$ samples. For these samples, a deep kink was observed at ~ 100 K and maximum H_c was observed at 150 K. Eckert et al. and Hilscher et al. also reported a maximum H_c at ~160 K for melt spun Nd-Fe-B magnets [39, 40]. The kink at low temperatures in the demagnetization curve can be attributed to spin reorientation [41, 42]. Spin reorientation is characterized by a temperature (T_{SR}) below which the easy axis of magnetization deviates from the c-axis, the anisotropy constant K_1 is zero in this condition [43]. Usually, $Nd_2Fe_{14}B$ has a T_{SR} of ~ 135 K [44-47], this value is strongly size-dependent for magnetic nanoparticles [43]. Usually nanocrystalline magnets

exhibit a lower T_{SR} compared to micro- or sintered magnets and magnetic nanoparticles possess a lower T_{SR} than nanocrystalline materials. Figure 6.7a suggests that for our samples, the spins reoriented at ~ 100 K. To further study T_{SR}, the magnetization vs. temperature curve was measured at a low applied field of 100 Oe (Figure 6.7b). The T_{SR} was determined by the derivative of the magnetization vs. temperature (dM/dT) curve. The T_{SR} for $(Nd_{1-x}Dy_x)_2(Fe,Co)_{14}B$ with x = 0, 0.1, 0.2 was found to be 115K, 110 K and 105 K, respectively. These values are close to the value of melt spun $Nd_2Fe_{14}B$ ribbons, and are ~ 20 K less than the corresponding values of bulk $Nd_2Fe_{14}B$ magnets, hence, they are more attractive for cryogenic applications. The change of T_{SR} with Dy content could be because Dy preferentially replaces Nd in the 4f site, altering the crystal anisotropy value. The reduction of T_{SR} with increasing Dy content in the nanoparticles was also reported by Rahimi et.al. In their work, spin-reorientation occurred at temperatures below 100 K [22]. The thermal stability of our samples was evaluated by calculating the thermal coefficient of remanence (α) and thermal coefficient of coercivity (β) in the temperature range between two temperatures, say T_1 and T_2, by the following equations:

$$\alpha(M_r) = \frac{M_r(T_2) - M_r(T_1)}{M_r(T_1)(T_2 - T_1)} \times 100\% \quad (6.1)$$

$$\beta(H_C) = \frac{H_C(T_2) - H_C(T_1)}{H_C(T_1)(T_2 - T_1)} \times 100\% \quad (6.2)$$

The M-H curves from 150 K to 400 K were used to calculate the temperature coefficients. It can be seen from Figure 6.7a that coercivity decreased with increasing temperature; the extent of decrease became larger when the temperature was increased beyond 350 K. The thermal coefficient of remanence (α) for $(Nd_{0.8}Dy_{0.2})_2(Fe,Co)_{14}B$ and $(Nd_{0.9}Dy_{0.1})_2(Fe,Co)_{14}B$ was found to be -0.053% and -0.142%, respectively. The thermal coefficient of coercivity (β) for $(Nd_{0.8}Dy_{0.2})_2(Fe,Co)_{14}B$ and $(Nd_{0.9}Dy_{0.1})_2(Fe,Co)_{14}B$ was found to be -0.348% and -0.370%, respectively. With increasing Dy content, the thermal stability of the magnetic nanoparticles improved, similar to previous reports using other processing techniques [21, 48, 49].

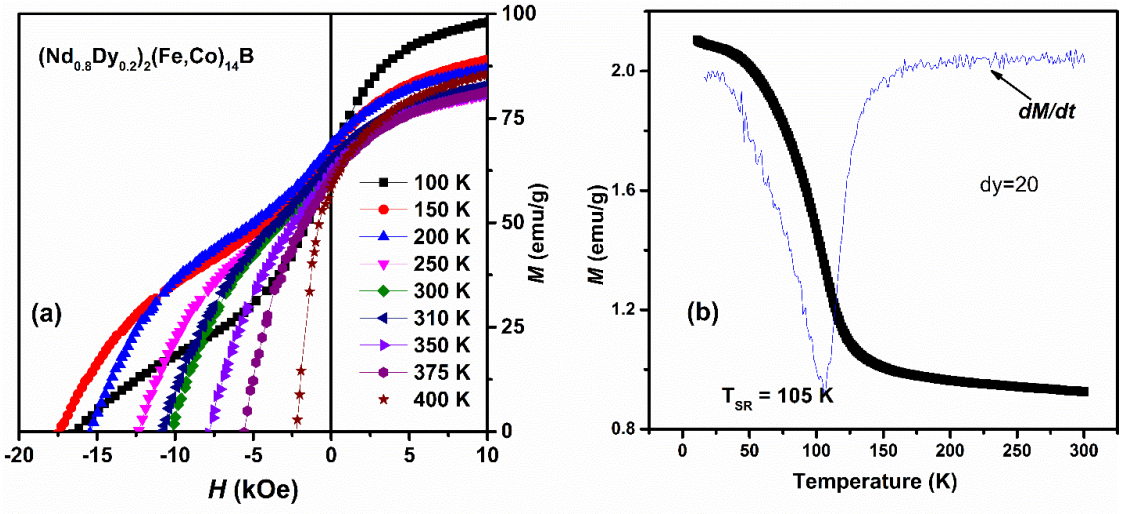

Figure 6.7. (a). M-H demagnetization curves of $(Nd_{0.8}Dy_{0.2})_2(Fe,Co)_{14}B$ at temperatures ranging from 100 K to 400 K. (b). M-T curve of $(Nd_{0.8}Dy_{0.2})_2(Fe,Co)_{14}B$ particles at an applied field of 100 Oe. dM/dT plots are constructed from the M-T plots to the T_{SR}.

The coercivity value H_c is highly sensitive to microstructure. For sintered Nd-Fe-B magnets, the coercivity can be described by Brown's equation, based on a nucleation type coercivity mechanism. If the demagnetization process is governed by the nucleation field, a modified form of Brown's equation can be used to describe the temperature dependence of coercivity, as shown below [33, 50, 51]:

$$\mu_0 H_c(T) = \alpha_K \mu_0 H_N^{min}(T) - N_{eff} M_s(T) \tag{6.3}$$

$H_c(T)$ is the coercivity measured at different temperatures, $H_N^{min}(T)$ is the minimum nucleation field, α_K and N_{eff} are microstructure related parameters, $M_s(T)$ is the spontaneous magnetization at different temperatures [52]. Due to the difficulty in finding the H_N^{min} value, a simpler version of this equation is employed to analyze the temperature dependence of H_c.

$$\mu_0 H_c(T) = \alpha H_A(T) - N M_s(T) \tag{6.4}$$

Where α and N are two microstructure related constants and $H_A(T)$ represents the temperature dependent anisotropy field. The value $H_A(T)$ of the Dy substituted $R_2Fe_{14}B$ phase can be calculated according to the rule of mixtures, as shown below [21, 53]:

$$H_A^{eff} = H_A^{Nd} \times \frac{C_{Nd}}{C_{Nd} + C_{Dy}} + H_A^{Dy} \times \frac{C_{Dy}}{C_{Nd} + C_{Dy}} \tag{6.5}$$

Where H_A^{Nd} and H_A^{Dy} represent the anisotropy field of $Nd_2Fe_{14}B$ and $Dy_2Fe_{14}B$, respectively, C_{Nd} and C_{Dy} indicate the atomic percentage of Nd and Dy in the system, respectively.

In Equation 6.4, the first term on the right is interpreted as the nucleation field of a reverse domain, the second term describes the average local demagnetizing effects. It was reported that the α value varies with grain size and that the *N* value varies with the smoothness of the grain boundaries [27, 28]. This equation is relevant to a nucleation-controlled mechanism [26]. From this equation, the plot of $\frac{\mu_0 H_c(T)}{M_s(T)}$ vs. $\frac{\mu_0 H_A(T)}{M_s(T)}$ should yield a straight line, with a slope of α and an intercept of $-N$.

Figure 6.8(a) shows the $\frac{\mu_0 H_c(T)}{M_s(T)}$ vs. $\frac{\mu_0 H_A(T)}{M_s(T)}$ plot for $(Nd_{1-x}Dy_x)_2(Fe,Co)_{14}B$ (x = 0, 0.1, 0.2) in the temperature range of 250 K to 400 K. Good linear fits can be seen for all samples, indicating that nucleation of reversed domains contributes to the magnetization reversal of $(Nd_{1-x}Dy_x)_2(Fe,Co)_{14}B$ particles. The statistical measurement of fit (adj. R^2) is 0.98, 0.97, 0.99 for these three fittings, respectively. Values of the microstructural constants are listed in the inset of Figure 6.7a: α is 0.36, 0.44, 0.37; and N is 1.5, 2.9, 2.2, respectively. The value of α does not vary much for the three samples, indicating that grain size did not change much with Dy content (Table 6.1). The difference in the demagnetization parameter *N* suggests that the grain boundaries are smooth and that the local stray field changed with Dy content. More studies are needed to confirm the effect of Dy substitution on the grain boundary.

Although the nucleation-controlled coercivity mechanism is supported by the $\frac{\mu_0 H_c(T)}{M_s(T)}$ vs. $\frac{\mu_0 H_A(T)}{M_s(T)}$ plot, the shape of the initial susceptibility curves suggest a more complex coercivity mechanism. Hence, we further tested the fit by a pinning dominated model [54], as shown below.

$$(\frac{H_C}{H_0})^{1/2} = 1 - (\frac{75k_BT}{4bf})^{2/3} \quad (6.6)$$

H_c is the coercivity, H_0 is the critical field in the absence of thermal activation, k_B is the Boltzmann constant, $4b$ is the interaction range of a pin equating with the domain wall width and f is the maximum restoring force per pin. All parameters (except H_c and T) are constants for a given sample. Thus a linear relationship should be obtained in $(H_c)^{1/2}$ versus $(T)^{2/3}$ plot. In Figure 6.8b, the relationship between $(H_c)^{1/2}$ vs. $(T)^{2/3}$ was plotted for these three samples and it was found that the experimental data points deviated from a linear relationship. The statistical measurement of fitting (adj. R^2) of these three fittings are 0.80, 0.89, 0.81, respectively. These findings suggest that strong pinning of domain walls may also take part in coercivity reversal. However, the process is still dominated by nucleation of reversed domains.

The coercivity mechanism for sintered Nd-Fe-B magnets is believed to be nucleation-controlled [27], while domain wall pinning is usually the dominant process for melt-spun Nd-Fe-B magnets [26]. However, the coercivity mechanism of Nd-Fe-B nanoparticles is still unclear. In this study, from the initial magnetization curve (Figure 6.3b), we found that the nucleation of reverse domains and the pinning of domain walls may co-exist in our $(Nd_{1-x}Dy_x)_2(Fe,Co)_{14}B$ magnetic particles. However, our study of the temperature dependent magnetic behavior suggested that the coercivity mechanism should be the nucleation of reverse domains.

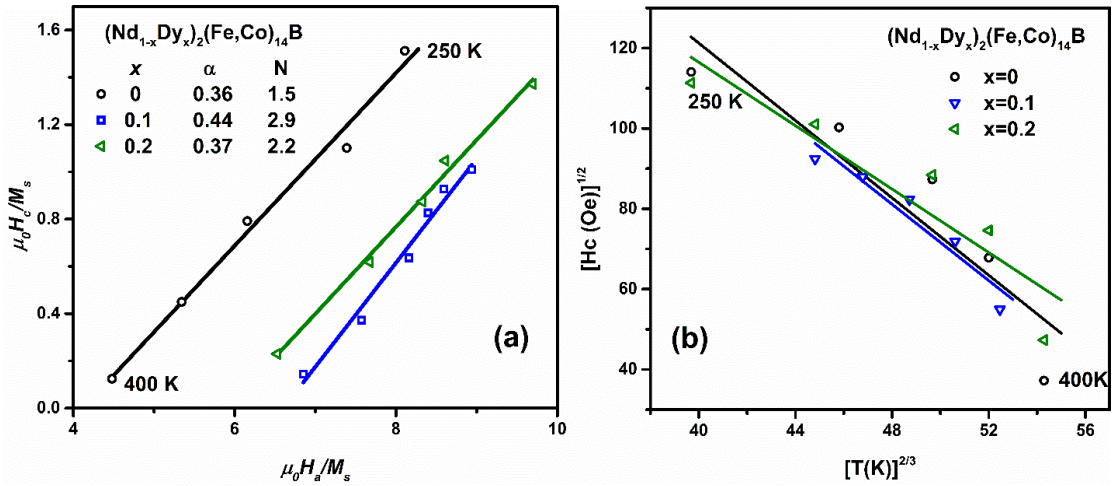

Figure 6.8.(a). Plots of $\frac{\mu_0 H_C(T)}{M_S(T)}$ vs. $\frac{\mu_0 H_A(T)}{M_S(T)}$, (b) plots of $(H_c)^{1/2}$ vs. $(T)^{2/3}$ for $(Nd_{1-x}Dy_x)_2(Fe,Co)_{14}B$ alloys (x = 0, 0.1, 0.2).

6.3 Conclusions

The effect of Dy content on the magnetic properties of $(Nd_{1-x}Dy_x)_2(Fe,Co)_{14}B$ nanoparticles produced by the mechanochemical process was studied. With increasing Dy content, the unit cell of $(Nd_{1-x}Dy_x)_2(Fe,Co)_{14}B$ contracts, indicating that Dy substituted for Nd. With increasing Dy content, the coercivity of $(Nd_{1-x}Dy_x)_2(Fe,Co)_{14}B$ increased dramatically from 8.8 kOe to 17.8 kOe until x=0.5. The temperature dependent magnetic measurements indicated good thermal stability for $(Nd_{0.8}Dy_{0.2})_2(Fe,Co)_{14}B$, with α = -0.053%, β = 0.348%. The reduced spin reorientation temperature of these particles suggests these Dy containing magnet are more attractive for cryogenic applications. The coercivity mechanism was analyzed through a study of the temperature dependent magnetic properties, and it was determined that nucleation of reversed domains was the controlling coercivity mechanism.

References

[1] C.-B. Rong, H.-W. Zhang, R.-J. Chen, B.-G. Shen, and S.-L. He. *Journal of Applied Physics*. **2006**, 100, 3913.

[2] J. Zhang *et al. IEEE Transactions on Magnetics*. **2011**, 47, 2792-2795.

[3] D. Brown, B.-M. Ma, and Z. Chen. *Journal of Magnetism and Magnetic Materials*. **2002**, 248, 432-440.

[4] N. Poudyal and J. P. Liu. *Journal of Physics D: Applied Physics*. **2012**, 46, 043001.

[5] O. Gutfleisch, M. A. Willard, E. Brück, C. H. Chen, S. Sankar, and J. P. Liu. *Advanced Materials*. **2011**, 23, 821-842.

[6] C. B. Rong *et al. Journal of Physics D: Applied Physics*. **2013**, 46, 045001.

[7] R. Skomski and J. Coey. *Physical Review B*. **1993**, 48, 15812.

[8] W. B. Cui, Y. K. Takahashi, and K. Hono. *Advanced Materials*. **2012**, 24, 6530-6535.

[9] O. Gutfleisch. *European School on Magnetism: New Experimental Approaches in Magnetism, Constanta*. **2005**, 1-7.

[10] P. K. Deheri, V. Swaminathan, S. D. Bhame, Z. Liu, and R. V. Ramanujan. *Chemistry of Materials*. **2010**, 22, 6509-6517.

[11] M. Jurczyk, J. Cook, and S. Collocott. *Journal of Alloys and Compounds*. **1995**, 217, 65-68.

[12] B. Cui, L. Zheng, W. Li, J. Liu, and G. Hadjipanayis. *Acta Materialia*. **2012**, 60, 1721-1730.

[13] B. Z. Cui, L. Y. Zheng, M. Marinescu, J. F. Liu, and G. C. Hadjipanayis. *Journal of Applied Physics*. **2012**, 111, 07A735.

[14] A. Pal, A. Gabay, and G. C. Hadjipanayis. *Journal of Alloys and Compounds*. **2012**, 543, 31-33.

[15] A. M. Gabay, X. C. Hu, and G. C. Hadjipanayis. *Journal of Alloys and Compounds*. **2013**, 574, 472-476.

[16] O. Koylu-Alkan, J. Barandiaran, D. Salazar, and G. Hadjipanayis. *AIP Advances*. **2016**, 6, 056027.

[17] V. Swaminathan, P. K. Deheri, S. D. Bhame, and R. V. Ramanujan. *Nanoscale*. **2013**, 5, 2718-2725.

[18] X. Tan, H. Parmar, Y. Zhong, V. Chaudhary, and R. V. Ramanujan. *IEEE Magnetics Letters*. **2017**, 5508805.

[19] H. Parmar, T. Xiao, V. Chaudhary, Y. Zhong, and R. V. Ramanujan. *Nanoscale*. **2017**, 9, 13956-13966.

[20] Y. Zhong, V. Chaudhary, X. Tan, H. Parmar, and R. V. Ramanujan. *Nanoscale*. **2017**, 9, 18651-18660.

[21] H. Rahimi, A. Ghasemi, R. Mozaffarinia, and M. Tavoosi. *Journal of Magnetism and Magnetic Materials*. **2017**, 424, 199-206.

[22] H. Rahimi, A. Ghasemi, R. Mozaffarinia, and M. Tavoosi. *Journal of Magnetism and Magnetic Materials*. **2017**, 429, 182-191.

[23] X. Liu and Z. Altounian. *Journal of Applied Physics*. **2012**, 111, 07A701.

[24] E. Burzo. *Reports on Progress in Physics*. **1998**, 61, 1099.

[25] X. H. Tan, S. F. Chan, K. Han, and H. Xu. *Scientific Reports*. **2014**, 4, 6805.

[26] J. Herbst. *Reviews of Modern Physics*. **1991**, 63, 819-898.

[27] A. Fukuno, K. Hirose, and T. Yoneyama. *Journal of Applied Physics*. **1990**, 67, 4750-4752.

[28] S. Hirosawa. *IEEE Transactions on Magnetics*. **1989**, 25, 3437-3439.

[29] E. d. T. De Lacheisserie, D. Gignoux, and M. Schlenker, *Magnetism: II-Materials and Applications*. Springer Science & Business Media, **2012**.

[30] W. Li, H. Sepehri-Amin, T. Ohkubo, N. Hase, and K. Hono. *Acta Materialia*. **2011**, 59, 3061-3069.

[31] M. Sagawa, S. Fujimura, H. Yamamoto, Y. Matsuura, and K. Hiraga. *IEEE Transactions on Magnetics*. **1984**, 20, 1584-1589.

[32] M. Ghandehari. *Applied Physics Letters*. **1986**, 48, 548-550.

[33] H. Li, Y. Liang, X. Tan, H. Xu, P. Hu, and K. Ren. *Materials*. **2017**, 10, 1062.

[34] T. Maki and S. Hirosawa. *Journal of Applied Physics*. **2008**, 103, 043904.

[35] R. Ramesh and K. Srikrishna. *Journal of applied physics*. **1988**, 64, 6406-6415.

[36] M. F. de Campos, F. A. da Silva, and J. A. de Castro. *Materials Science Forum*. **2014**, 802, 558-562.

[37] W. Fernengel, A. Lehnert, M. Katter, W. Rodewald, and B. Wall. *Journal of Magnetism and Magnetic Materials*. **1996**, 157, 19-20.

[38] C.-b. Rong, V. V. Nguyen, and J. P. Liu. *Journal of Applied Physics*. **2010**, 107, 09A717.

[39] D. Eckert, K. H. Muller, A. Handstein, J. Schneider, R. Grossinger, and R. Krewenka. *IEEE Transactions on Magnetics*. **1990**, 26, 1834-1836.

[40] G. Hilscher, R. Grössinger, S. Heisz, H. Sassik, and G. Wiesinger. *Journal of Magnetism and Magnetic Materials*. **1986**, 54, 577-578.

[41] D. Givord, H. Li, and R. P. De La Bâthie. *Solid State Communications*. **1984**, 51, 857-860.

[42] K. Tokuhara, Y. Ohtsu, F. Ono, O. Yamada, M. Sagawa, and Y. Matsuura. *Solid State Communications*. **1985**, 56, 333-336.

[43] C.-b. Rong, N. Poudyal, and J. P. Liu. *Physics Letters A*. **2010**, 374, 3967-3970.

[44] D. Givord, H. Li, and J. Moreau. *Solid State Communications*. **1984**, 50, 497-499.

[45] R. Grossinger, X. Kou, R. Krewenka, H. Kirchmayr, and M. Tokunaga. *IEEE Transactions on Magnetics*. **1990**, 26, 1954-1956.

[46] J. Herbst. *Reviews of Modern Physics*. **1991**, 63, 819.

[47] R. Skomski and J. Coey, *Permanent magnetism*. Institute of Physics Pub., **1999**.

[48] L. Yu, J. Zhang, S. Hu, Z. Han, and M. Yan. *Journal of Magnetism and Magnetic Materials*. **2008**, 320, 1427-1430.

[49] L. Yu, Y. Wen, and M. Yan. *Journal of Magnetism and Magnetic Materials*. **2004**, 283, 353-356.

[50] G. Martinek and H. Kronmüller. *Journal of Magnetism and Magnetic Materials*. **1990**, 86, 177-183.

[51] W. F. Brown Jr. *Reviews of Modern Physics*. **1945**, 17, 15.

[52] P. Kharel *et al. Journal of Physics D: Applied Physics*. **2013**, 46, 095003.

[53] S. Hirosawa, Y. Matsuura, H. Yamamoto, S. Fujimura, M. Sagawa, and H. Yamauchi. *Journal of Applied Physics*. **1986**, 59, 873-879.

[54] P. Gaunt. *Philosophical Magazine B*. **1983**, 48, 261-276.

Chapter 7

Discussion and Future Work

Nd-Fe-B type magnets are essential in almost every aspect of modern life, especially in electric machine systems. The development of a more cost-effective method, i.e., the mechanochemical processing technique, to synthesize Nd-Fe-B is vital due to its increasing demand. This chapter provides a general discussion to conclude the whole thesis and summarize the novelty and significance of the research work. First, the influence of the diluent (CaO) in the structure, properties and formation mechanism of $Nd_2(Fe,Co)_{14}B$ nanoparticles is systematically analyzed and optimized for better properties. Second, the formation mechanism of the $Nd_2(Fe,Co)_{14}B$ nanoparticles and the milling kinetics during mechanochemical processing were investigated to facilitate better control of the process. The effect of Dy-alloying in $Nd_2(Fe,Co)_{14}B$ nanoparticles produced by the mechanochemical process were studied and the structural and magnetic properties of the synthesized $(Nd_{1-x}Dy_x)_2(Fe,Co)_{14}B$ nanoparticles were examined. The coercivity reversal mechanism was also investigated. Based on the current research status, future work is also discussed.

7.1. General Discussion

This thesis focused on the synthesis and process optimization of Nd-Fe-Co-B based hard magnetic nanoparticles produced through a "green" and cost-effective mechanochemical method. The influence of diluent (CaO), milling speed and alloying (i.e., Dy addition) on the synthesized hard magnetic nanoparticles were investigated. Moreover, the formation mechanism of $Nd_2(Fe,Co)_{14}B$ powder particles and the milling kinetics of mechanochemical synthesis were also studied. The mechanism of coercivity reversal was also analyzed. These results deepened the understanding and allowed greater control of the synthesis of Nd-Fe-B based material through the mechanochemical process, making the process more readily available for industrial applications.

7.1.1 Discussion on the influence of dispersant (CaO) on the synthesized $Nd_2(Fe,Co)_{14}B$ nanoparticles

In this part, $Nd_2(Fe,Co)_{14}B$ hard magnetic nanoparticles were synthesized by a mechanochemical process. The synthesized nanoparticles have a size in the range of 40 – 250 nm and exhibit good ability to be crystallographically aligned. The influence of dispersant (CaO) on the process was studied. It was found that addition of 50 wt% CaO gives good magnetic properties of the nanoparticles. The crystal size of $Nd_2(Fe,Co)_{14}B$ nanoparticles increase with increasing CaO content until 50 wt%, with an enhancement in magnetic properties. Coercivity of the as-synthesized nanoparticles dropped by ~29% after the removal of by-product. This effect may due to the increasing density of anisotropic defects at the particle surface, induced by the by-product removal process. This study optimized dispersant content during mechanochemical synthesis of $Nd_2(Fe,Co)_{14}B$ and provided a relationship between the crystal size and the magnetic properties of $Nd_2(Fe,Co)_{14}B$ in the nano range.

The novelty and significance of this work are listed below:

(1). Nd-Fe-B based magnets are ubiquitous. Due to the increasing demand for high performance magnets, the development of a cost-effective method is essential to produce better and cheaper Nd-Fe-B based magnets. The mechanochemical method stands out due to its ability to produce superior Nd-Fe-B magnets. However, previous work produced Nd-Fe-B magnetic nanoparticles with poor magnetic properties. This could be due to hydrogen diffusion or oxidation induced by by-product removal process. In this work, after by-product removal, the coercivity drop is only ~ 29% for the $Nd_2(Fe,Co)_{14}B$ nanoparticles. These nanoparticles showed the best magnetic properties among all the mechanochemically processed Nd-Fe-B particles.

(2). The few previous reports on the mechanochemical synthesis of Nd-Fe-B magnets mainly focus on the synthesis of the magnetic nanoparticles rather than studying the influence of processing parameters. In this work, the effect of dispersant (CaO) content was systematically studied and optimized. It was found that with increasing CaO content until 50 wt%, the crystal size of the $Nd_2(Fe,Co)_{14}B$ particles increased from 12 nm to 38 nm, with enhanced coercivity from 5.1 kOe to 12.4 kOe. In addition, increasing dispersant (CaO) content delayed the reduction of precursor oxides and the formation of $Nd_2(Fe,Co)_{14}B$ particles. These findings optimized and deepened the understanding of the process. They indicated the relationship between the structure and the magnetic properties of the synthesized $Nd_2(Fe,Co)_{14}B$ particles.

7.1.2 Formation mechanism of $Nd_2(Fe,Co)_{14}B$ particles and milling kinetics during mechanochemical synthesis

The formation mechanism and processing kinetics are critical to understand and monitor the synthesis process. In this section, the $Nd_2(Fe,Co)_{14}B$ formation mechanism was analyzed by monitoring the phase transitions during the milling process. It was found that the majority of the reduction occurred during the mechanical milling process, while a small fraction of the reduction process, especially the reduction of Nd_2O_3, occurred during the heat treatment process. The reduction kinetics during milling were monitored by measuring the by-product (CaO) content at different milling times. It was found that the milling

process consists of 3 stages: (i) fast amorphization of precursor oxides, (ii) reduction of precursor oxides, (iii) steady state. A numerical model, which considered both physical impact and chemical reactions which occurred during the milling process was proposed to simulate the milling kinetics and estimate the milling efficiency. It was found that a milling speed of 550 rpm gives the highest milling efficiency.

The novelty and significance of this work are listed below:

(1). The reactions occurring during the mechanochemical milling for synthesis of $Nd_2(Fe,Co)_{14}B$ were revealed and monitored for the first time. The process was found to involve amorphization of precursor oxides in the initial stage, followed by reduction and steady-state behavior. Unlike some self-propagating metathesis process, milling energy is continuously needed in this mechanochemical process until steady state.

(2). A theoretical model was put forward for the first time to predict the milling kinetics during mechanochemical milling. Good agreement was obtained between the model and experimental data. Milling efficiency at different milling speeds can be estimated by this model, which helps to improve energy utilization efficiency in the future scaled up processes.

7.1.3 Influence of Dy-alloying on mechanochemically synthesized $(Nd_{1-x}Dy_x)_2(Fe,Co)_{14}B$ nanoparticles

In this work, the influence of Dy-alloying, in a range of Dy content (x = 0 – 0.6), on the structure and properties of $(Nd_{1-x}Dy_x)_2(Fe,Co)_{14}B$ nanoparticles synthesized by the mechanochemical method was investigated. It was found that the mechanochemical method can easily alloy Dy homogeneously into $(Nd_{1-x}Dy_x)_2(Fe,Co)_{14}B$ nanoparticles. The influence of Dy-substitution on the structure and magnetic properties were investigated. With increasing Dy content, the lattice parameters decrease due to lanthanide contraction, the coercivity increases from 8.8 kOe to 17.8 kOe until x = 0.5. Better thermal stability and smaller thermal coefficients was observed in the Dy-alloyed samples. The coercivity

reversal mechanism was examined for selected samples and it was found that the nucleation of reversed magnetic domains dominated the reversal process.

The novelty and significance of this work are listed below:

(1). Although previous work has synthesized $(Dy_{0.25}Nd_{0.75})_2Fe_{14}B$ and $Dy_2Fe_{14}B$ by the mechanochemical approach [1, 2], systematic investigation of Dy alloying has not yet been conducted. In this study, Dy in the range of $x = 0 – 0.6$ was incorporated in the magnetic $(Nd_{1-x}Dy_x)_2(Fe,Co)_{14}B$ nanoparticles. Structure and magnetic property investigations were conducted. It was shown that Dy was homogeneously distributed in these $(Nd_{1-x}Dy_x)_2(Fe,Co)_{14}B$ nanoparticles. With increasing Dy content, the coercivity increased until it reaches 17.8 kOe. The thermal stability was also enhanced.

(2). Various studies have been performed of the coercivity reversal mechanism of bulk and micron-sized Nd-Fe-B magnets. It is widely accepted that the coercivity reversal mechanism for sintered Nd-Fe-B is the nucleation of reserved domains and for melt-spun Nd-Fe-B is the domain wall pinning [3, 4]. However, the coercivity mechanism for nanoparticles may behave differently compared to these counterparts. In this work, the coercivity mechanism of the nanoparticles was studied. It was determined that nucleation of reversed domain is the controlling reversal mechanism.

7.2. Suggestions for future work

The main focus of the current work is the synthesis of Nd-Fe-B based hard magnetic nanoparticles by the mechanochemical technique. The synthesized nanoparticles possesses superior magnetic properties compared to other Nd-Fe-B based nanoparticles. However, further improvements can still be made.

7.2.1 Composition tuning

One advantage of the mechanochemical method is the ease of tuning the alloy composition.

The resultant alloy composition can be readily tuned by simply changing the composition of the precursor oxides. For Nd-Fe-B magnets, alloying or elemental substitution can improve the properties. In this thesis, partial Co substitution of Fe was used to improve the Curie temperature and Dy-alloying was employed to improve the coercivity and thermal stability. Other elemental substitution, investigated in Nd-Fe-B magnets processed by other methods, can produced similar benefits in mechanochemically processed Nd-Fe-B based alloys. Hence, elemental substitution can be studied in the future to enhance the magnetic properties. For example, Al or Ga were used to partially substitute for Fe to improve the coercivity in sintered NdFeB, since they can refine the microstructure of NdFeB magnets [5-7]. Partial substitution by Nb is was known to significantly increase coercivity, as Nb inhibited grain growth and promoted smaller and more homogeneous grain formation [8, 9].

The mechanochemical method can also be used to produce exchange coupled Nd-Fe-B magnets. Nd-lean compositions can be produced by reducing the Nd_2O_3 content in the precursor oxides. The ability of the mechanochemical method to produce nanoparticles implies that exchange coupled nanocomposite magnets can be produced. As the exchange coupled magnets possesses both high coercivity from the hard magnetic phase and the high saturation magnetization from the soft magnetic phase, magnetic nanoparticles with a higher energy product can be expected.

7.2.2 Coating of nanoparticles

One drawback of the nanoparticles produced by the chemical method is that they are not stable enough to be further heat treated. Coating of these nanoparticles with an inert shell may stabilize these nanoparticles, making them useful for a wider range of applications. It is not easy to compact the mechanochemically processed nanoparticles into dense magnets. An inert coating may also help in the densification of the magnets. Metallic coatings, including Al, Al-Mn, Fe, can effectively improve the corrosion resistance of the Nd-Fe-B magnets [10]. Similar coatings can be applied on the mechanochemically processed Nd-Fe-B nanoparticles for particle stabilization.

7.2.3 Improve the by-product removal method

Majority of the CaO was removed through water wash or acetic acid wash [11, 12]. These methods are exothermic and easily induce an oxide layer on the particle surface, in some cases, H can also be induced into the particle structure. Hence the magnetic property of the by-product removed samples drops a lot. The current by-product removal method uses NH_4Cl/methanol solution, which eliminate the potential exothermic reaction between CaO and water, and minimize the nanoparticle surface oxidation problem. However, severe coercivity drop is still associated with this process. Some new/better by-product removal methods are essentially needed to fully optimize the magnetic properties of the synthesized Nd-Fe-B magnetic nanoparticles and fully utilize the chemical synthesis method. From oxidation point of view, the process should be handled in oxygen-free environment if possible. From H diffusion point of view, less temperature should be aimed to decrease H diffusion coefficient, and H free condition should be used. Grain boundary condition can also be tuned to after by-product removal to compensate the coercivity loss, e.g., induce Nd-Al eutectic alloy into grain boundary.

7.2.4 Compaction of the synthesized nanoparticles

The synthesized Nd-Fe-B based magnetic nanoparticles are of no commercial use without proper compaction. Hence, compaction of the synthesized nanoparticles is essential in future work. However, conventional sintering and annealing methods can easily damage the property and structure of the synthesized nanoparticles. New and novel compaction techniques should be explored to compact the synthesized nanoparticles properly to usable bulk material. Recently, novel techniques such as spark plasma sintering was employed to compact the melt-spun powders without damaging the nanostructure in these powders. Similar approach can be used to compact the synthesized Nd-Fe-B based magnetic nanoparticles. Besides. Grain boundary engineering is now emerging as an interesting topic in hard magnetic materials. It would be easier to do grain boundary engineering with nanoparticles. Instead of current grain boundary techniques (e.g. annealing), simple mix of diffusion particles with the synthesized Nd-Fe-B magnetic nanoparticles can easily induce

a homogeneously grain boundary engineered structure after compaction. If grain boundary engineering and compaction can be properly done, further improvement of the magnetic properties of the bulk samples is possible.

References

[1] O. Koylu-Alkan, J. Barandiaran, D. Salazar, and G. Hadjipanayis. *AIP Advances*. **2016**, 6, 056027.

[2] A. M. Gabay, X. C. Hu, and G. C. Hadjipanayis. *Journal of Alloys and Compounds*. **2013**, 574, 472-476.

[3] A. Fukuno, K. Hirose, and T. Yoneyama. *Journal of Applied Physics*. **1990**, 67, 4750-4752.

[4] S. Hirosawa. *IEEE Transactions on Magnetics*. **1989**, 25, 3437-3439.

[5] K. Knoch, E.-T. Henig, and J. Fidler. *Journal of Magnetism and Magnetic Materials*. **1990**, 83, 209-210.

[6] X. Kou, X. Sun, Y. Chuang, T. Zhao, R. Grössinger, and H. Kirchmayr. *Journal of Magnetism and Magnetic Materials*. **1989**, 82, 327-334.

[7] K. Knoch, B. Grieb, E.-T. Henig, H. Kronmuller, and G. Petzow. *IEEE Transactions on Magnetics*. **1990**, 26, 1951-1953.

[8] D. Salazar, A. Martín-Cid, R. Madugundo, J. Garitaonandia, J. Barandiaran, and G. Hadjipanayis. *Journal of Physics D: Applied Physics*. **2016**, 50, 015305.

[9] R. Zhang, Y. Liu, J. Ye, W. Yang, Y. Ma, and S. Gao. *Journal of Alloys and Compounds*. **2007**, 427, 78-81.

[10] C. D. Qin, A. Li, and D. Ng. *Journal of Applied Physics*. **1996**, 79, 4854-4856.

[11] J. Lee, T.-Y. Hwang, H.-B. Cho, J. Kim, and Y.-H. Choa. *Scientific Reports*. **2018**, 8, 15656.

[12] B. Shen *et al*. *Angewandte Chemie*. **2018**, 10, 1002.